



**HAL**  
open science

## Geological context and significance of the clay-sulfate transition region in Mount Sharp, Gale crater, Mars: An integrated assessment based on orbiter and rover data

Melissa J Meyer, Ralph E Milliken, Kathryn M. Stack, Lauren Edgar, Elizabeth B Rampe, Madison L Turner, Kevin W Lewis, Edwin S Kite, Gwénaél Caravaca, Ashwin R Vasavada, et al.

### ► To cite this version:

Melissa J Meyer, Ralph E Milliken, Kathryn M. Stack, Lauren Edgar, Elizabeth B Rampe, et al.. Geological context and significance of the clay-sulfate transition region in Mount Sharp, Gale crater, Mars: An integrated assessment based on orbiter and rover data. Geological Society of America Bulletin, 2024, 10.1130/B37355.1. . hal-04649829

**HAL Id: hal-04649829**

**<https://hal.science/hal-04649829>**

Submitted on 16 Jul 2024

**HAL** is a multi-disciplinary open access archive for the deposit and dissemination of scientific research documents, whether they are published or not. The documents may come from teaching and research institutions in France or abroad, or from public or private research centers.

L'archive ouverte pluridisciplinaire **HAL**, est destinée au dépôt et à la diffusion de documents scientifiques de niveau recherche, publiés ou non, émanant des établissements d'enseignement et de recherche français ou étrangers, des laboratoires publics ou privés.



Distributed under a Creative Commons Attribution 4.0 International License

# Geological context and significance of the clay-sulfate transition region in Mount Sharp, Gale crater, Mars: An integrated assessment based on orbiter and rover data

Melissa J. Meyer<sup>1,†</sup>, Ralph E. Milliken<sup>1</sup>, Kathryn M. Stack<sup>2</sup>, Lauren A. Edgar<sup>3</sup>, Elizabeth B. Rampe<sup>4</sup>, Madison L. Turner<sup>5</sup>, Kevin W. Lewis<sup>5</sup>, Edwin S. Kite<sup>6</sup>, Gwénaél Caravaca<sup>7</sup>, Ashwin R. Vasavada<sup>2</sup>, William E. Dietrich<sup>8</sup>, Alexander B. Bryk<sup>8</sup>, Olivier Gasnault<sup>7</sup>, Stéphane Le Mouélic<sup>9</sup>, Christina H. Seeger<sup>10</sup>, and Rachel Y. Sheppard<sup>11,12</sup>

<sup>1</sup>Department of Earth, Environmental, and Planetary Sciences, Brown University, 324 Brook Street, Box 1846, Providence, Rhode Island 02912, USA

<sup>2</sup>Jet Propulsion Laboratory, California Institute of Technology, 4800 Oak Grove Drive, Pasadena, California 91109, USA

<sup>3</sup>Astrogeology Science Center, U.S. Geological Survey, 2255 N. Gemini Drive, Flagstaff, Arizona 86001, USA

<sup>4</sup>Astromaterials Research and Exploration Science Division, National Aeronautics and Space Administration (NASA) Johnson Space Center, 2101 NASA Parkway, Houston, Texas 77059, USA

<sup>5</sup>Department of Earth and Planetary Sciences, The Johns Hopkins University, 3400 N. Charles Street, Baltimore, Maryland 21218, USA

<sup>6</sup>Department of Geophysical Sciences, University of Chicago, 5734 S. Ellis Avenue, Chicago, Illinois 60637, USA

<sup>7</sup>Institut de Recherche en Astrophysique et Planétologie (IRAP), Unité Mixte de Recherche (UMR) 5277, Centre National de la Recherche Scientifique (CNRS), Centre National d'Etudes Spatiales (CNES), Université Paul Sabatier Toulouse III, 9 Avenue du Colonel Roche, 31400 Toulouse, France

<sup>8</sup>Department of Earth and Planetary Science, University of California, Berkeley, Berkeley, California 94709, USA

<sup>9</sup>Laboratoire de Planétologie et Géosciences, CNRS UMR 6112, Nantes Université, Université Angers, Le Mans Université, 44000 Nantes, France

<sup>10</sup>Division of Geological and Planetary Sciences, California Institute of Technology, 1200 E. California Boulevard, Pasadena, California 91125, USA

<sup>11</sup>Planetary Science Institute, 1700 East Fort Lowell, Tucson, Arizona 85719, USA

<sup>12</sup>Institut d'Astrophysique Spatiale, Université Paris-Saclay, Bâtiment 121, 91405 Orsay, France

## ABSTRACT

On Mars, phyllosilicate (“clay”) minerals are often associated with older terrains, and sulfate minerals are associated with younger terrains, and this dichotomy is taken as evidence that Mars’ surface dried up over time. Therefore, *in situ* investigation of the Mount Sharp strata in Gale crater, which record a shift from dominantly clay-bearing to sulfate-bearing minerals, as seen in visible–near-infrared orbital reflectance spectra, is a key science objective for the Mars Science Laboratory (MSL) *Curiosity* rover mission. Here, we present regional (orbiter-based) and *in situ* (rover-based) evidence for a low-angle erosional unconformity that separates the lacustrine and marginal lacustrine depos-

its of the Carolyn Shoemaker formation from the dominantly eolian deposits of the lower Mirador formation within the orbitally defined clay-sulfate transition region. The up-section record of wetter (Carolyn Shoemaker formation) to drier (lower Mirador formation) depositional conditions is accompanied by distinct changes in diagenesis. Clay minerals occur preferentially within the Carolyn Shoemaker formation and are absent within the lower members of the Mirador formation. At and above the proposed unconformity, strata are characterized by an increase in diagenetic nodules enriched in X-ray amorphous Mg-sulfate. Early clay formation in the Carolyn Shoemaker formation may have created a hydraulic barrier such that later migrating magnesium- and sulfur-rich fluids accumulated preferentially within the lower members of the Mirador formation. The proposed unconformity may have also acted as a fluid conduit to further promote

Mg-sulfate nodule formation at the Carolyn Shoemaker–Mirador formation boundary. These results confirm an association of the clay-sulfate transition with the drying of depositional environments, but they also suggest that at least some orbital sulfate signatures within the region are not time-congruent with the environmental signals extracted from primary sedimentology. Our findings highlight that complex interactions among primary depositional environment, erosion, and diagenesis contribute to the transition in clay-sulfate orbital signatures observed in the stratigraphy of Mount Sharp.

## INTRODUCTION

On Mars, orbital spectroscopic detections of phyllosilicate minerals (i.e., “clays”) broadly coincide with the ancient heavily cratered and valley network–carved Noachian (older than ca. 3.6 Ga) terrains (e.g., Bibring et al., 2006; Carr

Melissa J. Meyer  <https://orcid.org/0000-0003-2207-1435>  
†mjmeyer87@gmail.com

and Head, 2010; Ehlmann et al., 2011, 2013). These clay-bearing terrains predate the volcanically resurfaced Hesperian (ca. 3.6–3.0 Ga) terrains, which are host to widespread orbital spectroscopic signatures of hydrated sulfate minerals (Bibring et al., 2006; Carr and Head, 2010). This spatiotemporal transition from clay- to sulfate-forming environments observed from orbit has been hypothesized to record the global desiccation of the Martian surface environment (Bibring et al., 2006). However, satellite-based

observations alone often cannot unambiguously reveal specific paleoenvironments or processes corresponding to the observed clay-sulfate mineral transitions. In contrast, detailed, ground-based exploration of the Martian sedimentary rock record can reveal the ways in which it may preserve the climatic evolution, aqueous history, and potential habitability of the planet's surface conditions through time. This notion was part of the motivation that led to the selection of Gale crater (late Noachian to early Hesperian in age,

ca. 3.8–3.55 Ga; Thomson et al., 2011; Le Deit et al., 2013) as a landing site for the National Aeronautics and Space Administration (NASA) Mars Science Laboratory (MSL) *Curiosity* rover.

The ~150-km-diameter Gale crater (Figs. 1A and 1B) contains an ~5.2-km-high asymmetric mound of stratified rocks inferred to be the remnant of more extensive, crater-filling materials (e.g., Milliken et al., 2010; Anderson and Bell, 2010; Thomson et al., 2011; Grotzinger et al., 2015; Day and Kocurek, 2016; Kite et al., 2016).

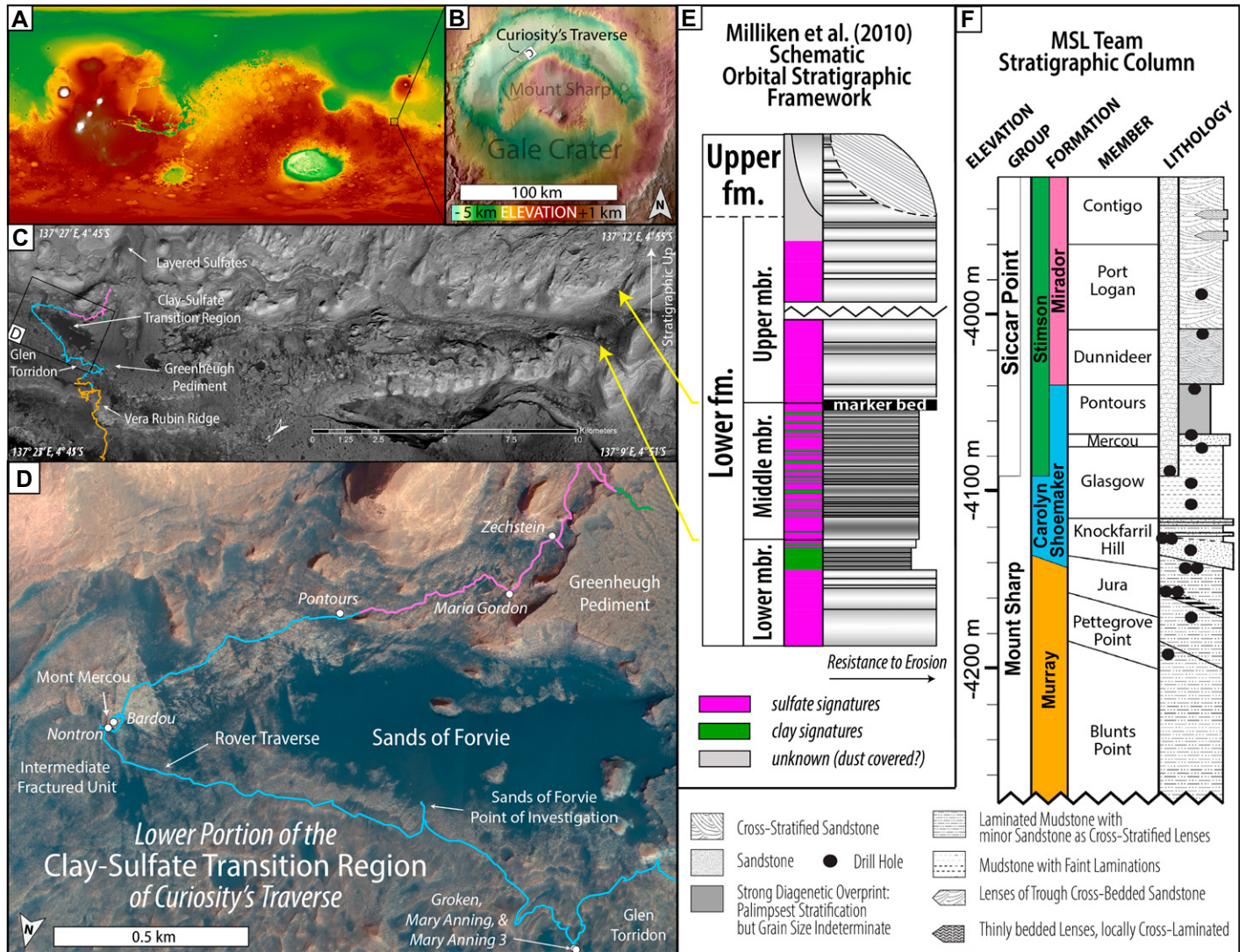


**Figure 1. Study location at Gale crater.** (A) Mars Orbiter Laser Altimeter (MOLA) color-shaded elevation map of Mars. Black box shows location of Gale crater. (B) MOLA color-shaded elevation map draped on Context Camera (CTX) image mosaic tiles (~5 m per pixel resolution; Dickson et al., 2018) showing Gale crater and in-lying Mount Sharp. *Curiosity*'s traverse from sol 0 to 3544 is marked by a white line. Black box shows rotated inset location of panel C. (C) Region of interest for the orbital mapping conducted in this study. Sols 1632–3544 of *Curiosity*'s traverse are shown and colored by formation as denoted on the Mars Science Laboratory (MSL) Team stratigraphic column shown in panel F. Black box shows inset location of panel D. Image is a subset of the MSL Gale orthophoto mosaic base map (Calef and Parker, 2016). (D) Colorized base map of the clay-sulfate transition region of *Curiosity*'s traverse. Traverse from sols 2786–3462 is marked and colored consistent with panel C. (E) Original preland orbital stratigraphic framework, modified with permission, from Milliken et al. (2010). Yellow arrows denote the location of lower-middle and middle-upper member boundaries. (F) Segment of the rover-based stratigraphic column. Names of specific drill holes for the region of interest can be found in Figure 4.

In situ investigation by *Curiosity* has determined the strata of the lowermost portion of the mound—formally Aeolis Mons, but informally known as Mount Sharp—to be sedimentary in origin. Satellite-based visible–near-infrared (VIS-NIR) spectral reflectance data that cover portions of Mount Sharp demonstrate an up-section transition from generally clay-bearing strata to those apparently more enriched in hydrated sulfates, with a transitional zone in between wherein the spectra indicate the presence of both types of hydrated minerals (Figs. 1C–1E; Milliken et al., 2010; Sheppard et al., 2021).

*Curiosity* traversed through the orbitally defined clay-sulfate transition within Mount Sharp approximately between mission sols 2800 and 3600 (or –4130 m and –3880 m elevation; Fig. 1D). Thus, it is now possible to investigate the sedimentology, mineralogy, and stratigraphy of this transition in situ, and to assess whether it reflects a drying trend as previously hypothesized (e.g., Milliken et al., 2010; Rapin et al., 2021). Here, we present orbiter- and rover-based evidence showing that an erosional unconformity exists within this intriguing clay-sulfate transition and separates clay-rich marginal lacustrine and fluvial deposits of the Carolyn Shoemaker formation from clay-poor eolian deposits of the Mirador formation. We demonstrate that the latter deposits contain an abundance of late diagenetic sulfate-bearing nodules, and that the orbitally observed clay-sulfate transition coincides with a significant change in depositional environment and a decrease in the availability of surface water in ancient Gale crater.

## BACKGROUND

### Existing Orbital Perspectives on the Clay-Sulfate Transition Region

The orbital observation of a vertical succession from clay to sulfate spectroscopic signatures in Mount Sharp was first discussed in detail by Milliken et al. (2010) (Fig. 1E). This interpretation, based on limited spectral (Compact Reconnaissance Imaging Spectrometer for Mars [CRISM]) and morphologic data (e.g., High Resolution Imaging Science Experiment [HiRISE] images) collected over parts of Gale crater, divided Mount Sharp strata into Lower and Upper formations separated by an erosional unconformity (e.g., Thomson et al., 2011; Milliken et al., 2010; Anderson and Bell, 2010). The Lower formation (estimated to be late Noachian to early Hesperian in age; Thomson et al., 2011) was further subdivided into lower, middle, and upper members that correspond to a light-dark-light tonality sequence that can be traced around the mound (Milliken et al., 2010; Sheppard

et al., 2021). The lower member of the Lower formation consists of light-toned and more massive strata with sulfate signatures that transition upward to clay (specifically, Fe-smectite) signatures (Milliken et al., 2010). The overlying, darker-toned, and more recessive strata of the middle member are characterized by mixed clay and sulfate signatures with increasingly more prominent layering (Milliken et al., 2010; Fraeman et al., 2016). A zone of darker-toned strata in the middle member is also noted to be enriched in the Mg-sulfate kieserite (Sheppard et al., 2021). A distinct smooth, erosion-resistant, dark-toned marker band (termed “marker bed” by Milliken et al., 2010; Weitz et al., 2022; hereafter referred to as the “marker band”) is traceable over long distances and defines the boundary between the middle and upper members of the Lower formation (Milliken et al., 2010; Weitz et al., 2022). The upper member represents a return to lighter-toned, massive, prominently layered, and sulfate-bearing strata generally lacking clay signatures (Milliken et al., 2010; Fraeman et al., 2016).

More recently, Sheppard et al. (2021) used additional CRISM data and improved processing techniques to show that clay signatures are more heterogeneously intercalated with sulfate signatures across Mount Sharp than proposed by Milliken et al. (2010). Sheppard et al. (2021) showed that clay mineral signatures are discontinuously present in multiple stratigraphic positions—including stratigraphically above the marker band—often occurring as thin units encapsulated by Mg-sulfate-bearing strata. These results parallel discoveries elsewhere on Mars (Wiseman et al., 2010; Flahaut et al., 2014; Cino et al., 2017; Carter et al., 2023) and challenge the hypothesis of a single, terminal clay-to-sulfate transition in Martian history. Instead, they suggest more protracted, patchy, and perhaps intermittent conditions conducive to clay and sulfate formation, respectively.

In both the Milliken et al. (2010) and Sheppard et al. (2021) studies, the clearest examples of changes in mineralogy with stratigraphic height were observed at locations to the west of—not coincidental with—*Curiosity*'s traverse path. That is, although a clay-to-sulfate transition region is observed as a key part of the overall mineralogical stratigraphy of Mount Sharp, correlations between mineralogy and specific strata are poorly expressed in orbital data where *Curiosity* actually explored that part of the section. This is largely due to the practical constraints of roving on Mars, where low-sloped and more eroded surfaces are easier to traverse. As an example, the darker-toned, kieserite-bearing strata of the middle member are prominent in many places throughout Mount

Sharp but are poorly expressed along *Curiosity*'s path (Sheppard et al., 2021). However, the strata that bracket the transition from the lower to middle member in the Milliken et al. (2010) and Sheppard et al. (2021) orbital stratigraphic frameworks are equivalent to those in the clay-sulfate transition region discussed in this paper. The origin of this change in mineralogy is not discernible from orbital data alone, and addressing this question through in situ observations has been a key goal of *Curiosity*'s mission.

### Rover-Based Stratigraphic Column and Perspectives on the Clay-Sulfate Transition Region

Along *Curiosity*'s traverse across the crater floor and continued ascent of Mount Sharp, the MSL Team routinely inspects encountered lithologies, noting changes with elevation in characteristics such as lamination style and thickness, sediment grain size, outcrop color, and degree of diagenesis (e.g., Fedo et al., 2022). This work is summarized in a lithostratigraphic column (Fig. 1F). The column is a log of generalized lithologies plotted against elevation as encountered along the rover traverse, and it is subdivided via conventional methods (North American Commission on Stratigraphic Nomenclature, 2005) into groups, formations, and members. In many places, it represents condensed stratigraphy across large lateral distances. Here, we briefly review relevant portions of the current stratigraphic column, emphasizing members within the Carolyn Shoemaker and Mirador formations of the Mount Sharp group that are present in the clay-sulfate transition region. This study also presents new details and support for interpretations of some of these units.

*Curiosity* began to ascend the lowest exposed strata along the northwest geographic boundary of Mount Sharp on sol 750, marking the start of exploration of the Mount Sharp group (MSg in Fig. 1F). The Mount Sharp group is currently divided into the Murray, Carolyn Shoemaker, and Mirador formations. The Murray formation (yellow traverse line in Fig. 1C) is dominated by well-laminated mudstones formed via suspension settling within a low-energy lacustrine depositional environment (Grotzinger et al., 2015; Rivera-Hernández et al., 2020; Stack et al., 2019; Edgar et al., 2020). Lower members of the Murray formation also contain cross-stratified and planar-laminated sandstones indicative of isolated eolian dune and interdune subenvironments, perhaps along a lacustrine margin (Gwizd et al., 2022). Upper members of Murray formation strata also exhibit a subtle coarsening-upward trend from mudstone to very fine sandstones that may reflect shallowing upward to a

nearshore lacustrine depositional setting (Edgar et al., 2020).

The overlying Carolyn Shoemaker formation (blue traverse line in Figs. 1C, 1D, and 1F) is divided into four members: the Knockfarril Hill, Glasgow, Mercou, and Pontours members. The Knockfarril Hill member at the base of the Carolyn Shoemaker formation is characterized by mixed lacustrine mudstones and fluvial cross-bedded sandstones (Fedo et al., 2022; Caravaca et al., 2022a). This member was well studied in the clay-rich Glen Torridon region (Fig. 1D; Fedo et al., 2022; Caravaca et al., 2022a). *Curiosity's* last place of exploration in Glen Torridon—and what we use as the first place of exploration for understanding the clay-sulfate transition region—is at the Mary Anning drill location (Fig. 1D). This location exhibits strong spectroscopic signatures of clay minerals from orbit. Here, three drill samples—Mary Anning, Mary Anning 3, and Groken—were obtained within Knockfarril Hill sandstones (Figs. 1D and 1F; Fedo et al., 2022; Thorpe et al., 2022; Treiman et al., 2023). The Knockfarril Hill member is overlain by a succession of finely laminated lacustrine mudstones that comprise the Glasgow member (Fedo et al., 2022). Together, the Knockfarril Hill and Glasgow members are interpreted to reflect a marginal lacustrine depositional environment with fluvial components (Fedo et al., 2022; Caravaca et al., 2022a).

Ancient river bars are recognized in the overlying Mercou member, which is prominently exposed in the cliff face of “Mont Mercou” (Fig. 1D), and interpreted to record an alluvial/shoreline environment (Cardenas et al., 2022). Two drill samples—Nontron and Bardou—were obtained at the base and top of this member, respectively. As will be demonstrated in this study, the final Carolyn Shoemaker formation member, Pontours, is heavily overprinted by diagenesis but shows faint evidence for the continuation of Glasgow-like planar-laminated mudstones, suggesting continuation of a marginal lake environment.

The onset of the overlying Mirador formation (Fig. 1F; pink traverse line in Figs. 1C and 1D) is characterized by large (meter-scale) cross-bedded sandstones, consistent with earlier predictions made from long-distance imaging efforts (Rapin et al., 2021); these are interpreted to be eolian in origin (Gupta et al., 2022; Rapin et al., 2021). *Curiosity* drilled several rocks in the Mirador formation (Fig. 1D), which has three distinct members: Dunnideer, Port Logan, and Contigo. Together, both the Dunnideer and Port Logan members reflect deposition in a dry eolian environment (Rapin et al., 2021; demonstrated in this study). We refer to the Dunnideer and Port Logan members together as the “lower” Mira-

dor formation in this study, and details of both are provided below. Incorporation of data and observations for this article concluded at the base of the Contigo member. While still dominantly eolian in origin, this member shows considerable evidence for local lacustrine and fluvial deposition in shallow interdune environments (Gupta et al., 2022; Caravaca et al., 2022b), suggesting the intermittent and local availability of water during the continued deposition of the Mirador formation.

The Stimson formation of the younger Siccar Point group unconformably overlies the Mount Sharp group succession (Fig. 1F) and is visible in some of the images presented here, notably as a capping unit of the Greenheugh Pediment (Fig. 1D). The Stimson formation preserves an arid eolian dune-field environment (Banham et al., 2021) and is interpreted to be significantly younger than Mount Sharp strata encountered thus far along *Curiosity's* traverse (Watkins et al., 2022).

In summary, the current stratigraphic understanding depicts a transition from wetter lacustrine-fluvial-alluvial conditions (as recorded by the Carolyn Shoemaker formation) to a drier eolian system (as recorded by the lower Mirador formation) within the orbitally identified clay-sulfate transition region. A focus of this study was to understand the nature and detailed geologic context of this important environmental transition through an integrated study of orbital- and rover-based observations.

## DATA SETS AND METHODS

### Orbital-Scale Mapping of Layer Boundaries

Prior to *Curiosity's* arrival in the clay-sulfate transition region, apparent layer boundaries visible in orbital data were mapped with ESRI ArcGIS Pro 3D using the Mars MSL Gale orthophoto mosaic base map (~25 cm per pixel spatial resolution) draped on the associated digital elevation model (DEM; vertical accuracy of ~1 m per pixel; Calef and Parker, 2016). Orbital-scale analyses focused on the area shown in Figure 1C. This 9 by 25 km (225 km<sup>2</sup>) area connects the clay-sulfate rover traverse region (i.e., Fig. 1D) to the original orbital-scale stratigraphic framework proposed by Milliken et al. (2010), which is best observed in the region southwest of the existing rover traverse (i.e., the right side of Figs. 1C and 1E).

The presence of an “orbital-scale layer boundary” was based on changes in layer texture, albedo, and/or topographic slope at the finest level of detail permitted by the base map, typically at a viewing scale of ~1:400. When

viewed under these conditions, layer boundaries were often traceable for several kilometers laterally. Figures 2A–2D show example layer boundary identifications; see Figure S1-A1 for an unmarked version of this figure, Figure S1-A2 for additional examples, and Data File S1-C1 for shapefiles of all completed orbital mapping results<sup>1</sup>.

Orbital-scale mapping was completed independent from ground-based mapping efforts for two reasons: (1) to separate the two scales of observations in order to test the extent to which layer boundaries at these two scales coincide, and (2) to retain relevance to orbital-scale studies elsewhere on Mars (e.g., Okubo, 2014; Kite et al., 2016; Okubo and Gaither, 2017) where in situ rover data are not available. For this reason, orbitally identified layer boundaries were not assumed a priori to represent primary bedding surfaces, geologic contacts, and/or diagenetic contacts.

For selected orbital layer boundaries, dip and dip azimuth were quantified by extracting the corresponding HiRISE elevation from the boundary line (see Fig. S1-A3). Planar fits were calculated from the resulting topographic profiles using ordinary least squares regression, with an angular error threshold of 2° (Turner and Lewis, 2023).

### Mastcam Mosaic Data Set Selection and Analyses

The Mast Camera (Mastcam) is a two-camera instrument mounted on *Curiosity's* mast 2 m above ground level that can capture images for broader geologic context. Mastcam image mosaics constructed by Malin Space Science Systems (Malin et al., 2017) served two purposes: (1) to investigate orbitally mapped layer boundaries regionally within far-field panoramic mosaics, and (2) to examine geologic features directly along *Curiosity's* traverse within near-field workspace mosaics. Image information for all analyzed mosaics and companion observations are listed in Data File S1-C2.

To translate layer boundaries from orbital data sets to rover images, the observation viewing geometry (latitude, longitude, elevation, field of view, pitch, and heading) was set in ArcGIS Pro to mimic the conditions of each Mastcam

<sup>1</sup>Supplemental Material. This study includes additional clarifying supplementary information, including examples of target classifications, raw data descriptions, additional supplementary figures, mapping shapefile results, and unmarked and unannotated versions of main text figures. Please visit <https://doi.org/10.1130/GSAB.S.25938268> to access the supplemental material; contact [editing@geosociety.org](mailto:editing@geosociety.org) with any questions.

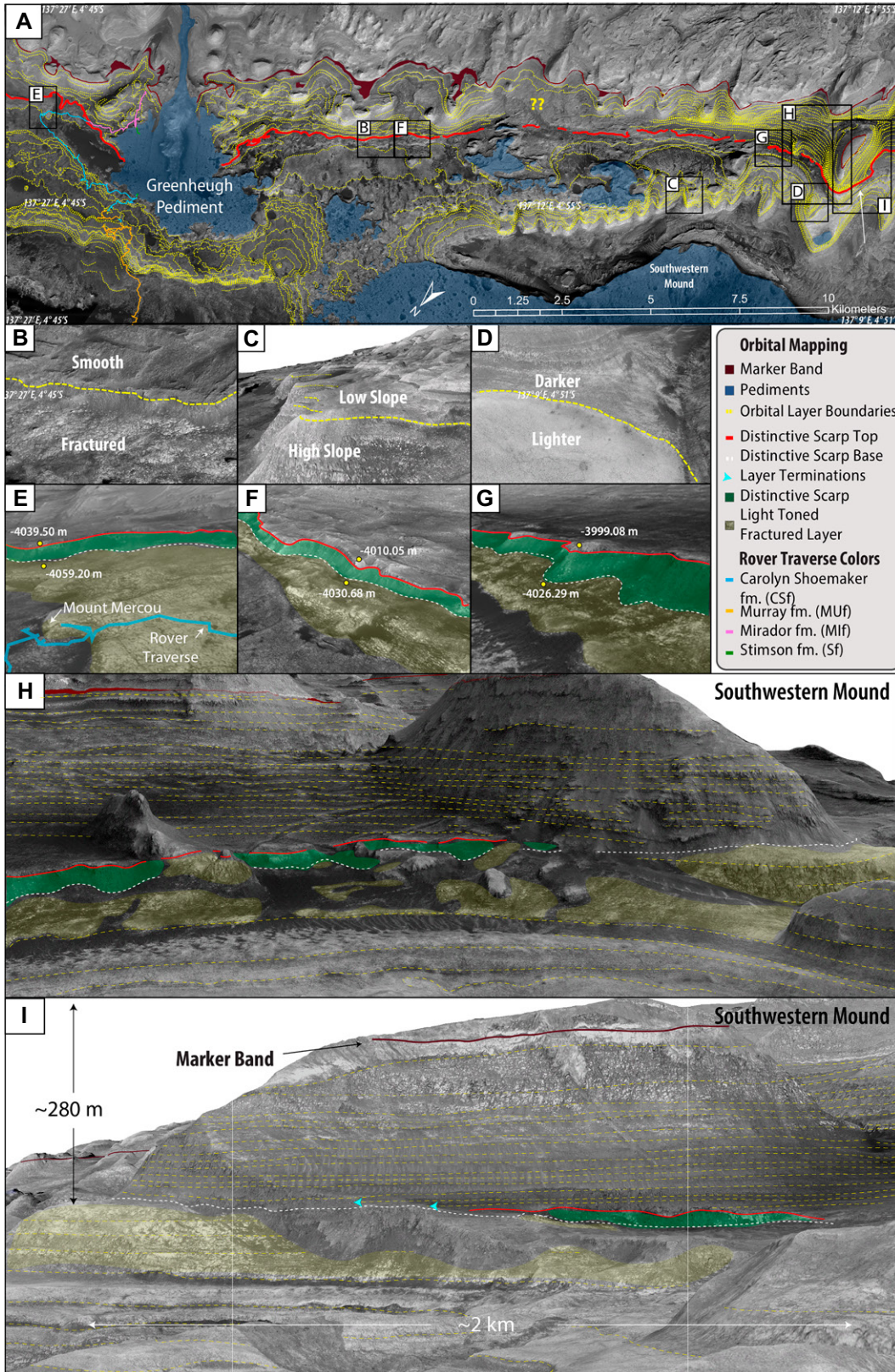


Figure 2. Orbital-scale layer boundary mapping results. See Figure S1-A1 for an unmarked and unannotated version of this figure (see text footnote 1). (A) Regional study area showing mapped orbital layer boundaries as yellow dashed lines. The previously identified Milliken et al. (2010) marker band is shown by the maroon lines and shading. Pediments, including the Greenheugh Pediment and the associated Gediz Vallis ridge, are mapped as dark-blue shading. Distinctive scarp top and bottom (appear as overlapping at this scale) are shown by the red solid line. Question marks note an area where layer boundary correlation is hindered by dust cover. Inset figure locations are shown by black boxes. (B–D) Examples of orbital layer boundaries identified by layered changes in texture (B), topographic slope break (C), and albedo (D). (E–G) Images of distinctive scarp across various portions of the study region. Distinctive scarp is identifiable by an underlying lighter-toned and fractured region (yellow shading) below, followed by a distinct increase in topographic slope at the scarp base (white dashed line), the scarp itself (green shading), the scarp top (solid red line), and a transition to smooth and darker-toned layers above. (H, I) Orbital views of the Southwestern Mound showing overlying orbital layer boundaries (yellow dashed lines) terminating against the distinctive scarp base (white dashed line) at the blue arrows. Scenes are 2× vertically exaggerated. As discussed in the main text, the visibility of the scarp top (red solid line) appears to be associated with variable concentrations of diagenetic features, so it can be laterally discontinuous and appear to merge with

the scarp base in some locations, particularly in large cliff faces as shown in panels H and I.

panoramic mosaic. The perspective view for each orbital scene was then overlain on the associated Mastcam panorama to allow orbital layer boundaries and rover traverse locations to be traced directly onto the latter. This method overcomes foreshortening effects that often impede correlation between these two types of image data. Thus, the orbital layer boundaries shown on rover-based images were derived from orbital analyses and may or may not correlate a priori to clear geologic, stratigraphic, and/or geomorphic attributes observed in ground-based images. Rover traverse route tracings translated to all panoramic images by these methods should be considered approximate. Height measurements shown in Mastcam far-field/panoramic mosaics are based on elevation values from the orbital HiRISE DEM, not from the Mastcam images, and as such they are only intended to be approximate.

Mastcam mosaics of near-field workspace outcrops (i.e., mosaics with images captured at focal distances of  $\sim 5$  m or less) along *Curiosity's* traverse were utilized to recognize the occurrence of sedimentary structures and diagenetic features. Emphasis on near-field observations permits the position on the stratigraphic column to be approximated by rover elevation. We utilized all near-field mosaics within the traverse range of interest, except for those that significantly overlapped, repeated, or imaged mainly sand or rover hardware. For each near-field mosaic, scale bars were generated by first selecting the individual frame with the median focus distance of all frames within the mosaic. This focus distance and the instantaneous field of view of the camera were then used to calculate pixel scale and generate a scale bar for the mosaic. By these methods, scale bars should be considered approximate, and true scale will vary as a function of distance within mosaics (Goetz et al., 2023).

### Small-Scale Textural and Compositional Analyses

#### Data Set Selections

In situ changes in chemistry and associated sedimentary and/or diagenetic textures were evaluated using data from the Chemistry Camera (ChemCam) instrument. ChemCam uses stand-off (from  $\sim 2$  m to 6 m) laser-induced breakdown spectroscopy (LIBS) to measure elemental compositions of small (on the order of  $500 \mu\text{m}$  in diameter) point measurement locations of selected targets in line or grid geometric configurations (Wiens et al., 2012; Maurice et al., 2012). We assessed LIBS data from the Mary Anning location in the Knockfarril Hill member of the Carolyn Shoemaker formation to the top

of the Port Logan member of the Mirador formation. Excluding calibration target measurements, this included elemental measurements acquired across 266 targets spanning the elevation range  $-4128$  m to  $-3955$  m. Additional information regarding ChemCam instrumentation is described in Text S1-B1.

Each LIBS target was imaged by ChemCam's Remote Micro Imager (RMI; Maurice et al., 2012) both before and after LIBS sampling with a field of view of 20 milliradians and an angular pixel size of  $19.6 \mu\text{rad}/\text{pixel}$  (Le Mouélic et al., 2015). At this optical resolution, the capacity to distinguish details is  $\sim 43 \mu\text{rad}$  in optimal conditions (Le Mouélic et al., 2015; Langevin et al., 2013). We examined the postmeasurement target RMI images (i.e., one image per LIBS target). The studied LIBS targets have an average stand-off distance of 2.68 m with a standard deviation of 0.34 m. Thus, the average pixel scale of target RMI images investigated in this study is  $\sim 52 \pm 6 \mu\text{m}$  per pixel, which, with the margins mentioned above, allows distinction of features at the scale of  $\sim 115 \pm 15 \mu\text{m}$ . Where available, Mastcam images were included for broader context in the analysis of each ChemCam target. Mastcam images collected on ChemCam target locations were acquired primarily by the right-eye camera (Mastcam-100 or M100), which has a focal length of 100 mm. At the average target stand-off distance of 2.68 m, Mastcam has a resolution of  $\sim 0.2$  cm per pixel.

Target and image names and associated descriptions for this combined data set can be accessed in Data File S1-C3. We focused primarily on ChemCam data for small-scale chemical and textural analyses because of the (1) large sample size, (2) well-constrained positional information, and (3) small spot size of LIBS and high resolution of RMI images, which allow chemical variability to be correlated with visible small-scale textural features. At some sites, images acquired by the Mars Hand Lens Imager (MAHLI) were also used to assist in textural analyses. Mounted on *Curiosity's* robotic arm, the MAHLI camera can acquire high-resolution (up to  $14 \mu\text{m}$  per pixel) color images of rocks and soils (Edgett et al., 2015).

#### ChemCam LIBS Measurement Classification Schemes

To better isolate compositional variability associated with individual geologic features, ChemCam LIBS point measurements were classified according to several schemes (Fig. 3). First, associated Mastcam images were inspected to categorize each whole ChemCam LIBS target as (1) in place (or likely in place) bedrock, (2) float, or (3) unconsolidated sand or pebbles (see Fig. S1-A4 for example classifications). Float

and unconsolidated sand or pebble targets were excluded from all results presented in this article.

Individual LIBS point measurements within each in-place bedrock ChemCam target were further classified according to the apparent geologic feature sampled by the measurement as evident from RMI images. The four individual feature classes were (1) bedrock, (2) nodules, (3) veins/fractures, and (4) sand-covered bedrock (Fig. 3; see Fig. S1-A5 for examples). Additional descriptions of these classifications can be found in Text S1-B2.

The in-place bedrock measurements were further subclassified according to the geologic feature sampled at each individual LIBS point (Fig. 3). Measurements sampling sand- or pebble-covered in-place bedrock were discarded. Of the remaining LIBS point measurements, 1075 points sampled bedrock, 282 points sampled apparent nodules, and 246 points sampled apparent veins or fractures (Fig. 3).

Bedrock, nodule, and vein/fracture classes were then further divided into 10 subcategories (Fig. 3). Bedrock points enriched in calcium (beyond 8.19 wt%, or one standard deviation of the total bedrock measurement data) were separated into a CaO-enriched bedrock class, and the remaining bedrock points were categorized as "typical" bedrock. LIBS points that sampled nodules and fracture/vein features were further categorized by morphology via Mastcam and RMI image inspection (Fig. 3).

#### Descriptive Schemes for Small-Scale Lithologic Textures

For all in-place bedrock LIBS targets, several lithologic attributes were also defined by inspection of RMI and non-color-corrected, non-color-stretched Mastcam M100 images. Lithologic attributes included lamination visibility, lamination expression, bedrock sheen, grain visibility, fracture/vein pervasiveness, nodule pervasiveness, nodule size, and nodule erosion resistance (see Figs. S1-A4 through S1-A13 for detailed descriptions and examples and Data File S1-C3 for the classification output). Quantitative abundance estimates of characteristics (e.g., apparent nodule pervasiveness across a target) were completed for each target based on the ChemCam RMI image field of view. Where sizes of features were classified (e.g., apparent nodule size), the scale bars provided by the ChemCam team in each RMI image were utilized. See Le Mouélic et al. (2015) for methods of RMI image scale bar generation.

#### CheMin Mineralogic Data Set Selection

In the studied portion of the clay-sulfate transition region, *Curiosity* acquired powder

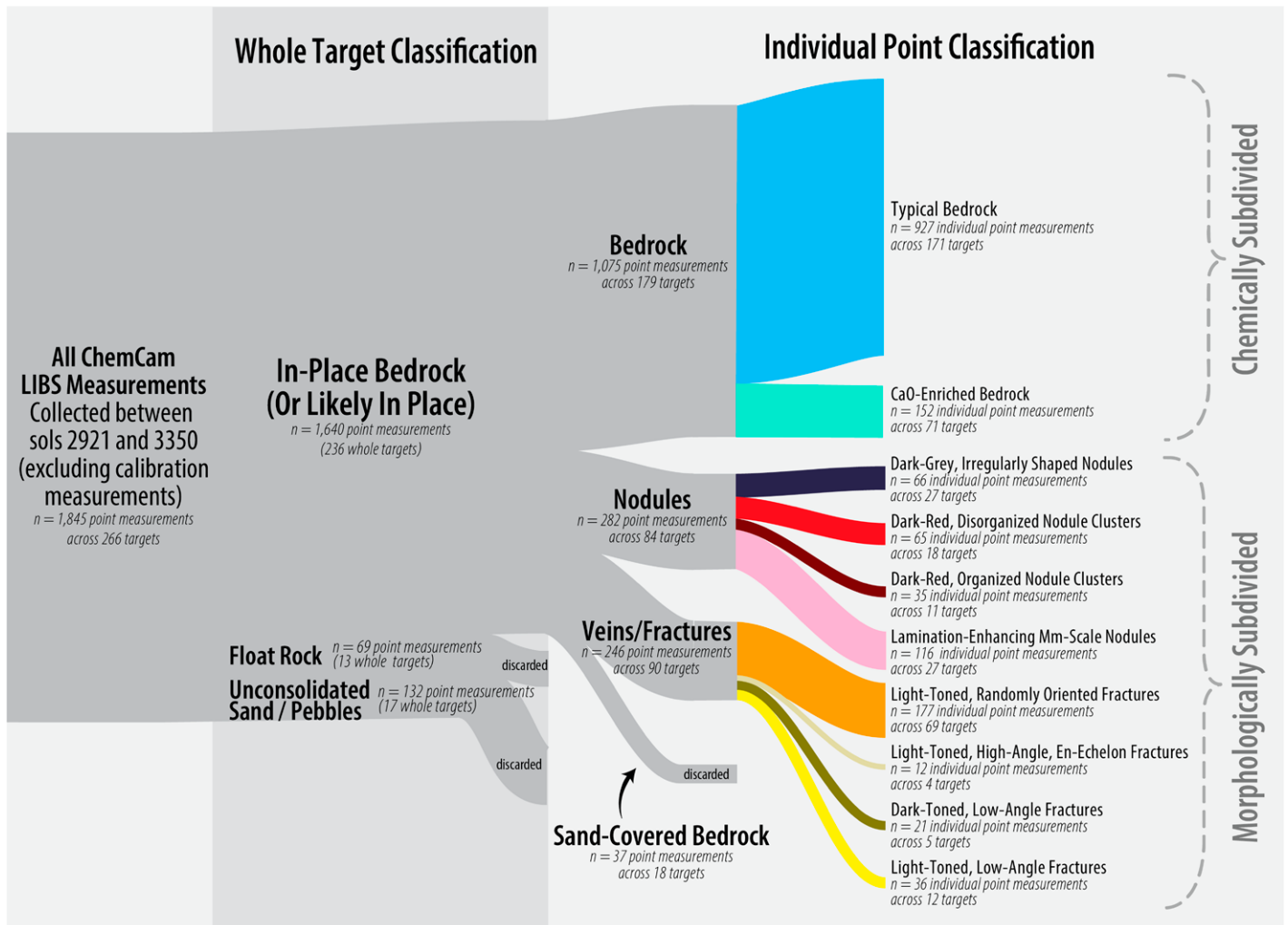


**Figure 3. Classification scheme of ChemCam laser-induced breakdown spectroscopy (LIBS) data.** See Figures S1-A1 through S1-A10 for examples of all classification schemes (see text footnote 1). All ChemCam LIBS data collected on geologic targets between sols 2921 and 3350 were included in initial analyses. Float rock and unconsolidated sand and pebble targets were differentiated from in-place bedrock measurements and discarded. Individual LIBS point measurements within each in-place bedrock ChemCam target were then further classified according to geologic feature sampled (bedrock, nodules, veins/fractures, and sand-covered bedrock), as apparent from ChemCam Remote Micro Imager (RMI) images. Sand-covered bedrock measurements were discarded. Bedrock measurements were then chemically subdivided into two subclasses, nodules were morphologically subdivided into four subclasses, and veins/fractures were morphologically subdivided into four subclasses, as recognized via Mastcam image analysis of near-field rover workspaces.

samples drilled from eight bedrock locations for analysis by the Chemistry and Mineralogy (CheMin) X-ray diffractometer (Blake et al., 2012). Drill samples included Mary Anning, Mary Anning 3, Groken, Nontron, Bardou, Pontours, Maria Gordon, and Zechstein (for drill locations, see Fig. 4). The quantitative mineral abundances discussed here were determined by the CheMin Team (see Thorpe et al., 2022; Rampe et al., 2022, 2023) using the Materials Data, Inc., JADE™ and FULLPAT programs (e.g., Chipera and Bish, 2013).

## ORBITAL AND ROVER OBSERVATIONS OF A DISTINCTIVE SCARP

### Recognition of a Distinctive Scarp via Orbital-Scale Layer Boundary Mapping

A map of layer boundaries identified from orbit in the study area is shown in Figure 2A (see Fig. S1-A1 for an unannotated version of this figure). Pediments, such as the Greenheugh Pediment (Bryk et al., 2019), are distinguished by their dark tone, bounding scarps, and abundant craters and are mapped as blue-shaded poly-

gons in Figure 2A. The “marker band” (maroon lines and shading in Fig. 2A) is distinguished by its darker tone, smooth texture, and relatively enhanced erosional resistance (mapped consistent with previous work by Milliken et al., 2010; Sheppard et al., 2021; Rapin et al., 2021; Weitz et al., 2022).

Many layer boundaries are laterally continuous on the order of several kilometers (sometimes >10 km) within the Mount Sharp group stratigraphy. Layer boundaries are easier to trace in the southwest portion of the study region (i.e., right side of Fig. 2A) than near the rover traverse,

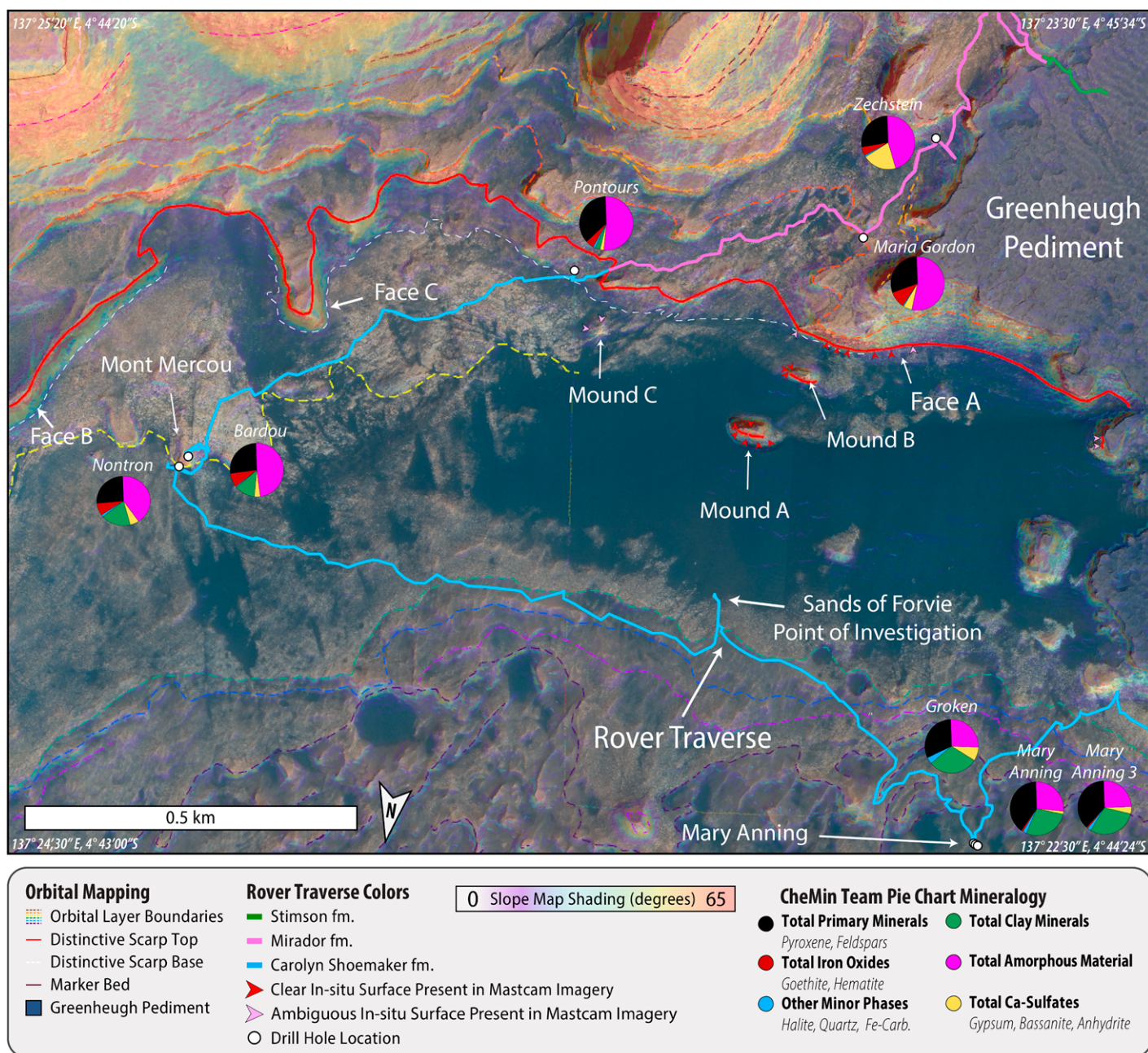


**Figure 4.** Mapping results in the clay-sulfate transition region of *Curiosity*'s traverse. Note the intersection of the distinctive scarp top (red solid line) with *Curiosity*'s transition into the Mirador formation (pink traverse line). Other orbital layer boundaries are shown by the colored dashed lines. Mars Science Laboratory (MSL) Gale orthophoto mosaic base map is overlain by a transparent rainbow-shaded slope map calculated from the corresponding digital elevation model. Note the increase in slope at the distinctive scarp (rainbow shading and white dashed line). Eight drill-hole locations and their corresponding X-ray diffraction (XRD) mineralogy are shown by white circles and pie charts, respectively. Points of in situ surface identification (transferred from Figs. 5 and 6) are marked by the dark (definitive) and light (ambiguous) red arrows.

likely owing to steeper slopes and reduced dust, sand, and talus cover. Here, a vertical succession of 32 laterally continuous layer boundaries was identified. Subtle changes in albedo and topographic slope were the basis for many of the layer boundaries in the southwest portion

of the study area, whereas many layer boundaries closer to the rover traverse were defined exclusively by changes in topographic slope and exhibit no significant change in albedo or texture at the scale of HiRISE images (see Fig. S1-A2 for additional mapping results).

Through this orbital mapping approach, we also identified a distinct and traceable scarp that occurs in association with the light-to-dark transition associated with the boundary between Milliken et al. (2010)'s lower and middle members. This distinctive scarp is identifiable based on an

underlying lighter-toned and fractured zone (yellow shading in Figs. 2E–2I), a distinct increase in topographic slope (white dashed line and green shading in Figs. 2E–2I; see also the slope maps in Fig. S1-A12), a scarp top (red solid line in Figs. 2E–2I), and a transition to an overlying smoother and darker-toned region (at and above red solid line in Figs. 2E–2I). The distinctive scarp is regionally correlative and projects across the rover traverse path in the clay-sulfate transition region (red solid line in Figs. 2A and 2E–2I). Where present, this scarp has a topographic relief across the study region of up to 27 m (20, 20, and 27 m at locations shown in Figs. 2E, 2F, and 2G, respectively). The scarp face (i.e., green shading in Figs. 2E–2I) is typically darker in tone than the underlying lighter-toned and fractured zone, and the scarp base (white dashed line in Figs. 2E–2I) is often covered by sand and talus.

Where exposures are very steep, such as the location we refer to as the Southwestern Mound (Figs. 2A, 2H, and 2I), relief along the distinctive scarp diminishes, and the laterally equivalent horizon is defined purely on the basis of a change in tone (i.e., light versus dark) and texture (i.e., fractured versus smooth). The face of the Southwestern Mound shown in Figure 2I contains the steepest and least sand- and talus-covered exposures in the study area. Here, the local scarp transitions to a larger cliff face, and the boundary that defines the scarp top ultimately merges with the boundary that defines the scarp base (Fig. 2I). As demonstrated and discussed below, this is due to the appearance/relief of the scarp being linked to diagenetic features that vary in abundance/concentration laterally and vertically. That is, the boundary that marks the scarp top appears to be a diagenetic one, thus explaining why it sometimes appears to “merge” with the well-defined boundary that coincides with the scarp base.

The boundary that marks the base of the scarp is laterally continuous over long distances and can be traced into larger cliffs, suggesting this boundary is not diagenetic. Within the study region, layers beneath this boundary appear to be thicker, lighter in tone, and heavily fractured. Layers above the boundary appear to be comparatively thinner, darker toned, and smoother in texture. In addition, a key observation in the Southwestern Mound is that the overlying layers appear to be dipping slightly steeper and, in rare places, gently terminate against the boundary that correlates to the scarp base (light-blue arrows in Fig. 2I). Structural measurements of layers below and above this boundary average a dip of 2.7°N45W and 3.0°N44W, respectively (see Fig. S1-A3). The distinctive scarp itself has an average dip of 4.7°N44W (see Fig. S1-A3). Deviations along the boundary from this best-fit orientation indicate variable relief, typically

ranging within  $\pm 11$  m from the best-fit surface (see Fig. S1-A3).

Correlation of this distinctive scarp and its associated boundaries from the southwestern exposure in the orbital study region (Fig. 2I) back to the clay-sulfate transition region of the rover traverse (Fig. 4) enables a direct comparison of orbiter- and rover-based observations (Figs. 5 and 6). In the following sections, we present rover-based observations across this boundary—which occurs within the clay-sulfate transition region—for three separate localities. First, we show that a clear surface can be observed in correlation with this boundary in distant mounds and outcrop faces adjacent to the Greenheugh Pediment (Fig. 6, red arrows). Second, we examined this distinctive scarp near Mont Mercou to demonstrate that a prominent change in outcrop expression occurs across this boundary that is broadly consistent with orbital observations. Next, we present a description of primary and diagenetic attributes of near-field outcrops encountered along the broader transect of *Curiosity*'s traverse where it intersects this orbitally defined boundary.

#### Far-Field Mastcam Observations of Cliff Faces and Mounds Adjacent to the Greenheugh Pediment

While traversing southeastward from the Mary Anning and Groken drill sites, *Curiosity* imaged several mounds and cliff-face exposures that provided some of the first in situ views of the distinctive scarp. We discuss six different locations, which we refer to as mound A, B, and C and face A, B, and C (Figs. 4–6). Mounds A and B and face A are near the Greenheugh Pediment (imaged from across the Sands of Forvie region; e.g., Fig. 5B). Mound A exhibits a prominent and traceable planar surface (red arrows in Fig. 6A) that corresponds with the location of the distinctive scarp as identified from HiRISE images. The surface is observed  $\sim 12$  m up the  $\sim 30$ -m-tall mound and is visible from multiple vantage points (e.g., red arrows in Figs. 6A and 6E), indicating continuity through the mound. An  $\sim 2$ -m-thick darker-toned horizon overlies this surface (e.g., yellow arrows in Figs. 6A and 6E). The top of mound A is dissected by relatively high-angle fracturing (e.g., green lines in Figs. 6A and 6E).

The surface present in mound A also extends through mound B (red arrows in Figs. 6A and 6D) and into face A (Figs. 6B and 6C), albeit with variable expression. In contrast to mounds A and B, the surface appears curvilinear in face A. The darker-toned horizon overlying the surface in mound A is also not apparent in face A. Like at mound A, high-angle fracturing dissects the top of mound B (e.g., green lines in Fig. 6D).

Outcrop slope noticeably affects visibility of the surface: steeper slopes provide better exposure (e.g., left side of Fig. 6B), whereas lower-slope terrain results in poorer exposure (e.g., right side of Fig. 6B). This phenomenon impedes unambiguous correlation of the surface from face A eastward toward the low-slope terrain traversed by *Curiosity* (e.g., from right to left in Fig. 6C). A trough of sand also conforms loosely to the projected location of the surface in this low-slope terrain (pink arrows in Fig. 6C), further hindering direct and confident correlation laterally toward the rover traverse route.

#### Far-Field Mastcam Observations of Scarp Faces near Mont Mercou

Images acquired farther to the southeast, closer to Mont Mercou (e.g., face B in Fig. 5A), provide additional in situ views of the distinctive scarp. A clear change in outcrop color is apparent when comparing the lighter-toned bedrock below the scarp's base (e.g., yellow arrows in Figs. 5A, 6G, and 6I) to the darker-toned bedrock within and above the scarp face (e.g., cyan arrows in Figs. 5A, 6G, and 6I). Textural differences between outcrops at the scarp base and top are also apparent. Beneath the scarp's base, lighter-toned bedrock is heavily crosscut by meter-scale sand-filled fractures (e.g., yellow arrows in Fig. 6I), consistent with orbital observations.

Rover images reveal that bedrock within and above the scarp is not as “smooth” as it appears at the resolution of HiRISE images. Instead, it is heavily dissected at a submeter scale by both high-angle fracturing (e.g., green lines in Figs. 6G, 6H, and 6I) and low-angle fracturing (e.g., magenta lines in Fig. 6I). Bedrock is dislocated along high-angle fractures, giving rise to the rubbly appearance along the scarp tops (e.g., green arrows in Figs. 6G, 6H, and 6I). This heavy fracturing, coupled with excessive sand cover at the base of the scarp, prevents unambiguous interpretation of primary stratification in these images. Although it is difficult to disentangle the influence of fracturing, hints of both horizontal and inclined stratification are suggested at variable heights within the scarp face (e.g., blue lines in Figs. 6G, 6H, and 6I). Whether absent or present but obscured by sand, fractures, and/or diagenetic overprint, the scarp in these locations lacks clear evidence of the prominent surface present in mounds and cliff faces closer to the Greenheugh Pediment. Instead, these localities exhibit only a change in outcrop color and texture. Although scarp relief significantly diminishes laterally (westward) toward the rover traverse, these changes in outcrop expression persist.

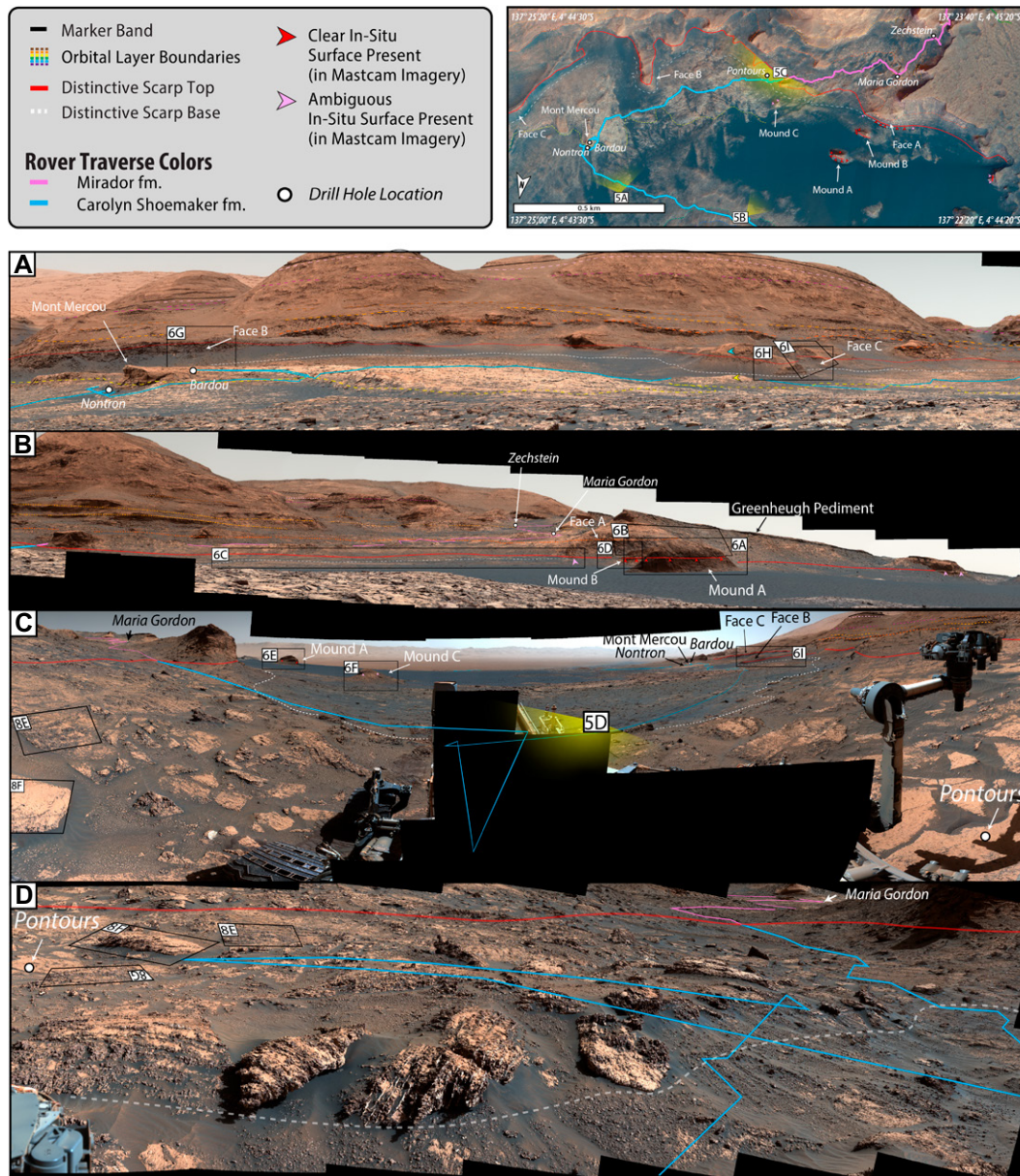


**Figure 5.** In situ inspection of the distinctive scarp via Mastcam panorama. Rover location and approximate field of view (yellow-shaded polygons) for each panoramic image are shown on the map in the upper right. See Figure S1-A14 for an unmarked and unannotated version of this figure and Figure S1-A15 for the ArcGIS Pro High Resolution Imaging Science Experiment (HiRISE) scenes used to translate orbital layer boundaries and rover traverse locations to each Mastcam panoramic image (see text footnote 1). See Data File S1-C2 for all Mastcam image sequence information (see text footnote 1). (A) Overview panoramic image near Mont Mercou. At  $\sim 500$  m stand-off distance from the distinctive scarp, a change in the in situ outcrop expression coincides with the distinctive scarp: Bedrock tonality changes from lighter below to slightly darker redder above, and topographic slope steepens notably. Color contrast across the boundary is most pronounced (e.g., compare bedrock and yellow and blue arrows), and the associated scarp is prominent despite significant sand cover. In this location, a discrete surface within the scarp is not identifiable. (B) Closer to the Greenheugh Pediment, where outcrop slopes steepen in face A

and mounds B and C, a clear throughgoing surface correlates with the distinctive scarp. Toward the rover traverse, visibility of this surface diminishes. However, the lighter-to-darker transition in bedrock tonality is throughgoing. (C) At the Pontours workspace, bedrock is strongly overprinted by diagenesis and covered by sand. Visibility of any primary stratification is rare, and the surface present closer to the Greenheugh Pediment in panel B cannot be identified here unambiguously. (D) The dark-red, linearly organized nodules appear pervasive where *Curiosity*'s traverse intersects the base of the distinctive scarp (white dashed line) and around the Pontours workspace.

## LITHOLOGIC DESCRIPTIONS OF STRATIGRAPHIC MEMBERS

Ultimately, *Curiosity*—guided by mobility constraints—traversed across the low-slope terrain between the localities described above where scarp relief is significantly diminished (Fig. 4). In this region, the mapped location of the scarp broadly aligns with the transition from the Carolyn Shoemaker formation into the Mirador formation, a boundary marked in the MSL Team

composite stratigraphic column at  $\sim 4040$  m elevation (Fig. 7). We now present more detailed lithologic descriptions of outcrops from near-field images along the traverse region below, at, and above this boundary—from the upper portion of the Glasgow member of the Carolyn Shoemaker formation to the top of the Port Logan member of the Mirador formation (Figs. 7–9; see Data File S1-C2 for raw descriptions). In addition to changes in sedimentary structures, diagenetic characteristics also systematically change

within this stratigraphic transition. The lithologic descriptions are followed by details on the stratigraphic changes in mineralogy as well as details for eight distinct populations of diagenetic features recognized in this region (Fig. 9).

### Glasgow Member, Carolyn Shoemaker Formation

At the base of Mont Mercou (Figs. 4 and 7), Glasgow member mudstones exhibit millime-

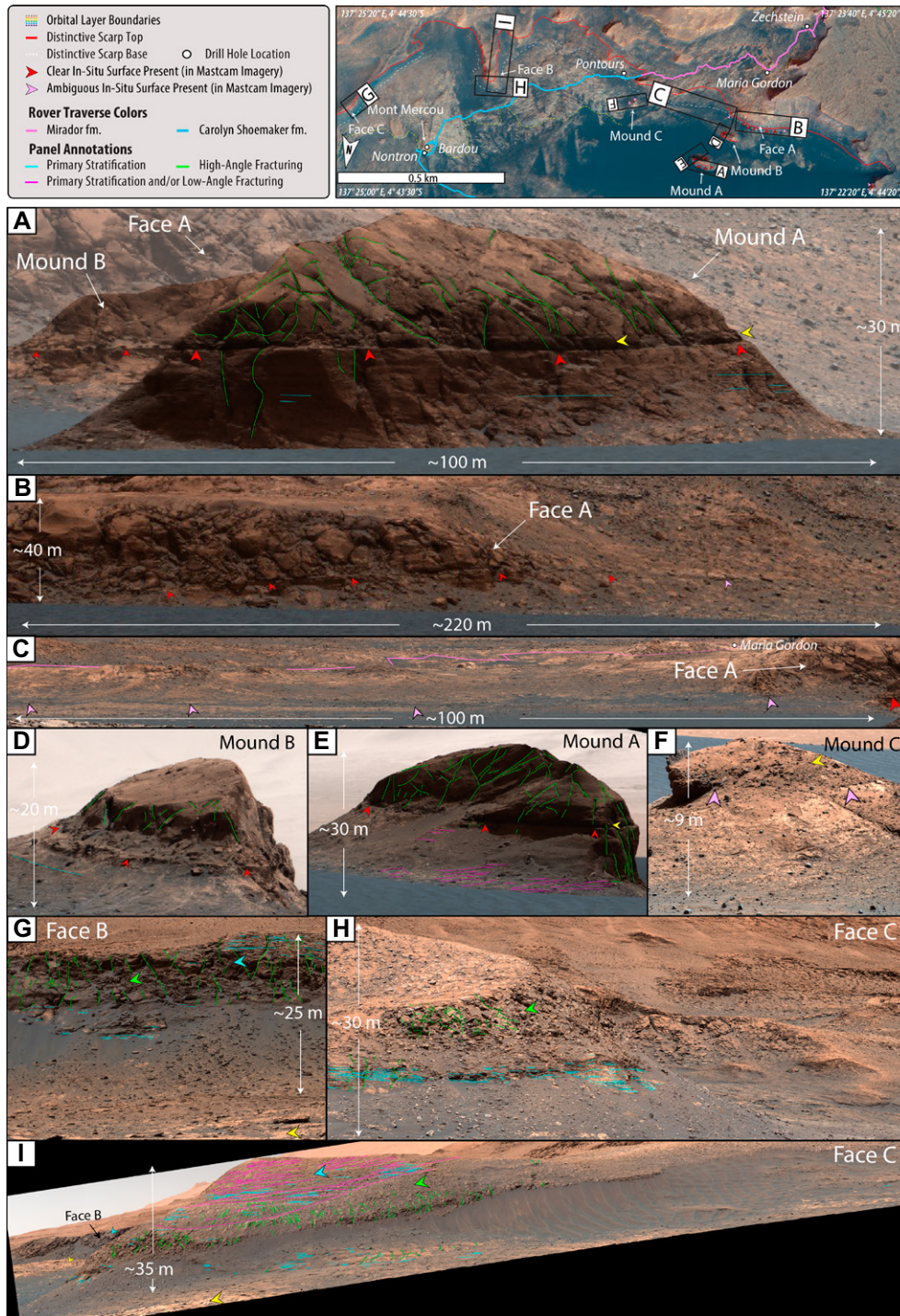


**Figure 6.** Inset images from Mastcam panorama shown in Figure 5 for closer in situ inspection of the distinctive scarp location. Inset image locations are shown on the map in the upper right. See Figure S1-A17 for an unmarked and unannotated version of this figure and Data File S1-C2 for all Mastcam image sequence information (see text footnote 1). Distances and heights annotated by the white lines were determined by using the measuring tool in ArcGIS Pro on the orthophoto mosaic map and associated digital elevation map and therefore should be considered approximate. (A) View of mound A showing a prominent surface (red arrows) at the location predicted by the distinctive scarp. An ~2-m-thick dark-toned band (yellow arrows), rubbly texture, and high-angle fracturing (green lines) are present above this surface. Hints of planar stratification (blue lines) are ambiguously present below this surface. The prominent surface also extends through mound B (red arrows). Note that background terrain has been whitened in this image to enhance mound visibility. (B) The prominent surface present in mounds A and B is also thoroughgoing into face A. Surface traceability declines significantly toward the right side of the image, demonstrating the often intermittent nature of stratigraphic surface visibility in rover images. (C) When attempting to trace the prominent surface eastward from face A toward its intersection with the rover traverse route, surface visibility again diminishes due to low slope of terrain and sand cover. (D) An oblique view demonstrating that the surface is continuous through mound B. (E) Oblique view demonstrating that the surface is continuous through mound A. High-angle fracturing (green lines) is also present on this side of mound A. Possible low-angle fracturing or hints of gently inclined stratification (pink lines) are present at the base of the mound. (F) View of mound C, with a contact (pink arrows) marked between a lighter-toned mound base and a darker-toned, rubbly mound top, which may correlate to the dark-toned band above the prominent surface observed in mound A. (G) View of face B showing the distinctive scarp that is darker in tone (compare bedrock at yellow and blue arrows), approximately ~25 m in relief, and crosscut by high-angle fracturing (green lines). Hints of possible stratification (blue lines) appear both horizontal and gently inclined. (H) View of face C showing the distinctive scarp and high-angle fracturing (green lines) and associated rubbly texture (green arrow) at the upper part of the scarp. Hints of possible stratification (blue lines) appear both horizontal and gently inclined. (I) Oblique view of face C showing high-angle fracturing (green lines) and associated rubbly texture (green arrow) are present across the upper part of the scarp, here showing conjugate fracture orientations. Hints of possible stratification (blue lines) within the scarp appear both horizontal and gently inclined. An additional set of low-angle linear features (pink lines) present across the scarp could be primary stratification or low-angle fracturing. The distinct lighter-to-darker change in tonality is also observed across this scarp face (e.g., compare bedrock at yellow and blue arrows).

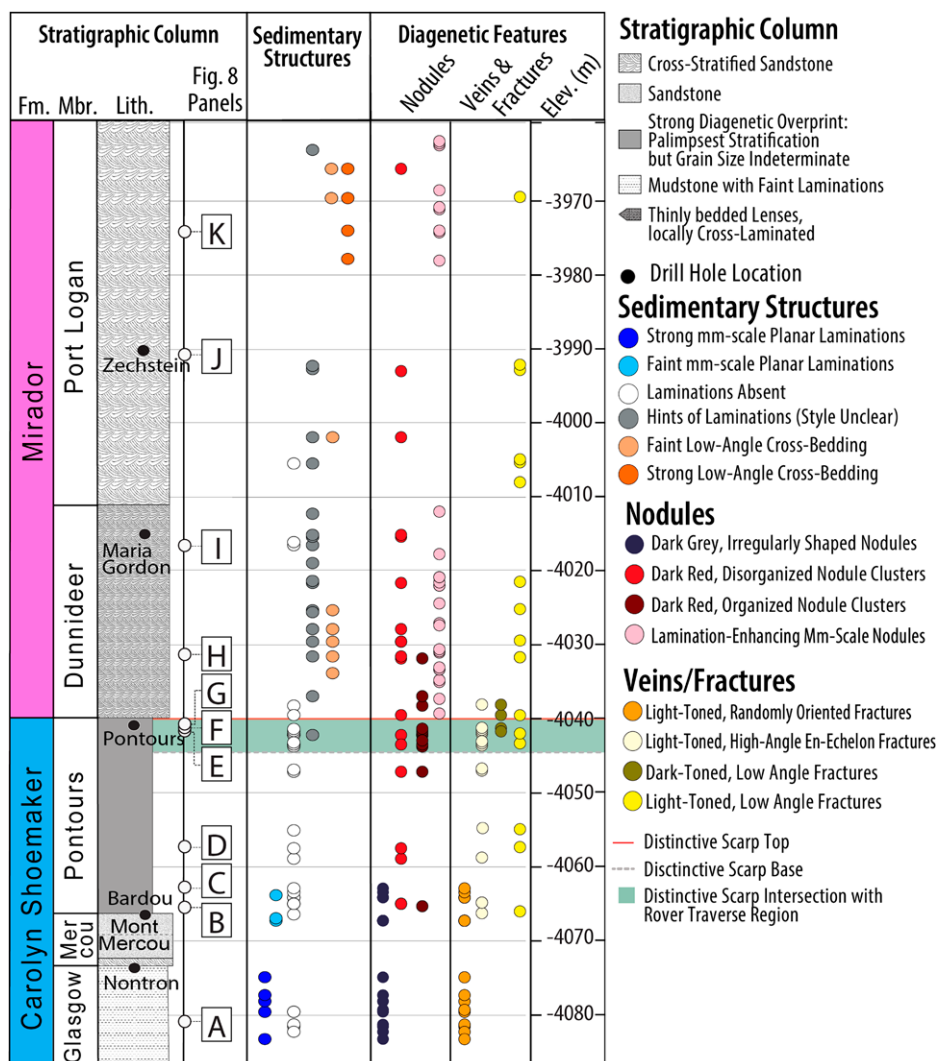


**Figure 7.** Mars Science Laboratory (MSL) Team stratigraphic column plotted against observed occurrences of sedimentary structures and recognized diagenetic nodule and vein/fracture classes. Examples for each classification are shown in Figures 8 and 9. The team stratigraphic column is an integrated representation of the stratigraphy as encountered along the rover traverse path. In this version, the dashed green zone between the red solid and black dashed lines represents the projected position of the distinctive scarp based on elevations in mounds adjacent to the lower-sloped rover traverse region. As noted in the text, the absolute elevation of the scarp base, taken to be coincident with the regional unconformity, is variable at kilometer and longer scales. The overlay of the scarp position onto the integrated stratigraphic column highlights the degree of uncertainty in the exact position of the unconformity—coincident with the Carolyn Shoemaker formation–Mirador formation boundary—along the rover traverse path. Prior to this study, and as depicted in the column, the Carolyn Shoemaker formation–Mirador formation boundary was estimated to be at an elevation of  $\sim$ –4040 m, in rough alignment with the position of the scarp top. The actual boundary and unconformity may be  $\sim$ 5 m lower, but significant diagenetic overprinting precludes accurate location of the boundary along the specific rover traverse path (see section “Correlation of the Basal Mirador Formation Unconformity to *Curiosity*’s Traverse Route” for details).

ter-scale planar laminations, noted by previous workers as being indicative of a lacustrine depositional environment (e.g., Fedo et al., 2022;

see Fig. 8A). Glasgow outcrops are typically fractured into meter- to decimeter-scale blocky exposures separated by sand. The dusty top sur-

faces of these blocks offer poor exposure (e.g., red arrow in Fig. 8A), but the cleaner sides reveal millimeter-scale, parallel, planar laminations in gray-colored mudstones (blue arrows in Fig. 9A).

Considerable diagenetic variability is well documented throughout the Glasgow member (e.g., Seeger et al., 2023; Gasda et al., 2022). Mudstones at the base of Mont Mercou consistently exhibit a distinct combination of protruding, dark-gray, irregularly shaped nodules (e.g., navy arrows in Fig. 9G) and light-toned, randomly oriented veins (e.g., gold arrows in Fig. 9K). Faint hints of laminations can be traced undisturbed through sufficiently large nodules (e.g., white arrow in Fig. 9A). Both laminations and nodules are pervasively dissected by randomly oriented, light-toned veins that range from hairline to centimeters in thickness.

### Mercou Member, Carolyn Shoemaker Formation

The Mercou member outcrops in the  $\sim$ 7-m-tall cliff face of Mont Mercou (Fig. 4). The stratigraphic section is well exposed in three dimensions and was analyzed in detail by Cardenas et al. (2022). The lower  $\sim$ 4 m interval of section, which is remarkably free of diagenetic overprint, is interpreted to record a fluvial bar form of an ancient river that flowed south as part of a larger, partially exhumed channel belt with locally superimposed dunes migrating up the back of the bar (Cardenas et al., 2022). The upper  $\sim$ 3 m interval of section is heavily overprinted by near bed-parallel fracturing and lacks clear indication of primary stratification (Seeger et al., 2023).

### Pontours Member, Carolyn Shoemaker Formation

The base of the Pontours member exhibits faint evidence for the continuation of millimeter-scale planar laminations (light-blue arrows in Fig. 9B) in gray-toned and blocky fractured outcrops, reminiscent of the Glasgow member at the base of Mont Mercou (cf. Figs. 8B and 8C to 8A). Bedrock is similarly marked by protruding, dark-gray, and irregularly shaped nodules (white arrows in Fig. 9B) and is crosscut by light-toned, randomly oriented veins and fractures. A few meters up section, overprinting by diagenetic nodules and veins increases in intensity, and the faint hints of laminations diminish (cf. Fig. 8B to 8C). The outcrops encountered along the remaining  $\sim$ 20 m within the Pontours member are distinctly lacking in clear evidence of primary stratification (Figs. 7, 8D, and 9C; Fig. S1-A18A). Instead, bedrock is marked by the appearance of a diverse array of diagenetic nodules and veins (Figs. 7 and 8D–8G; Fig. S1-A18B).

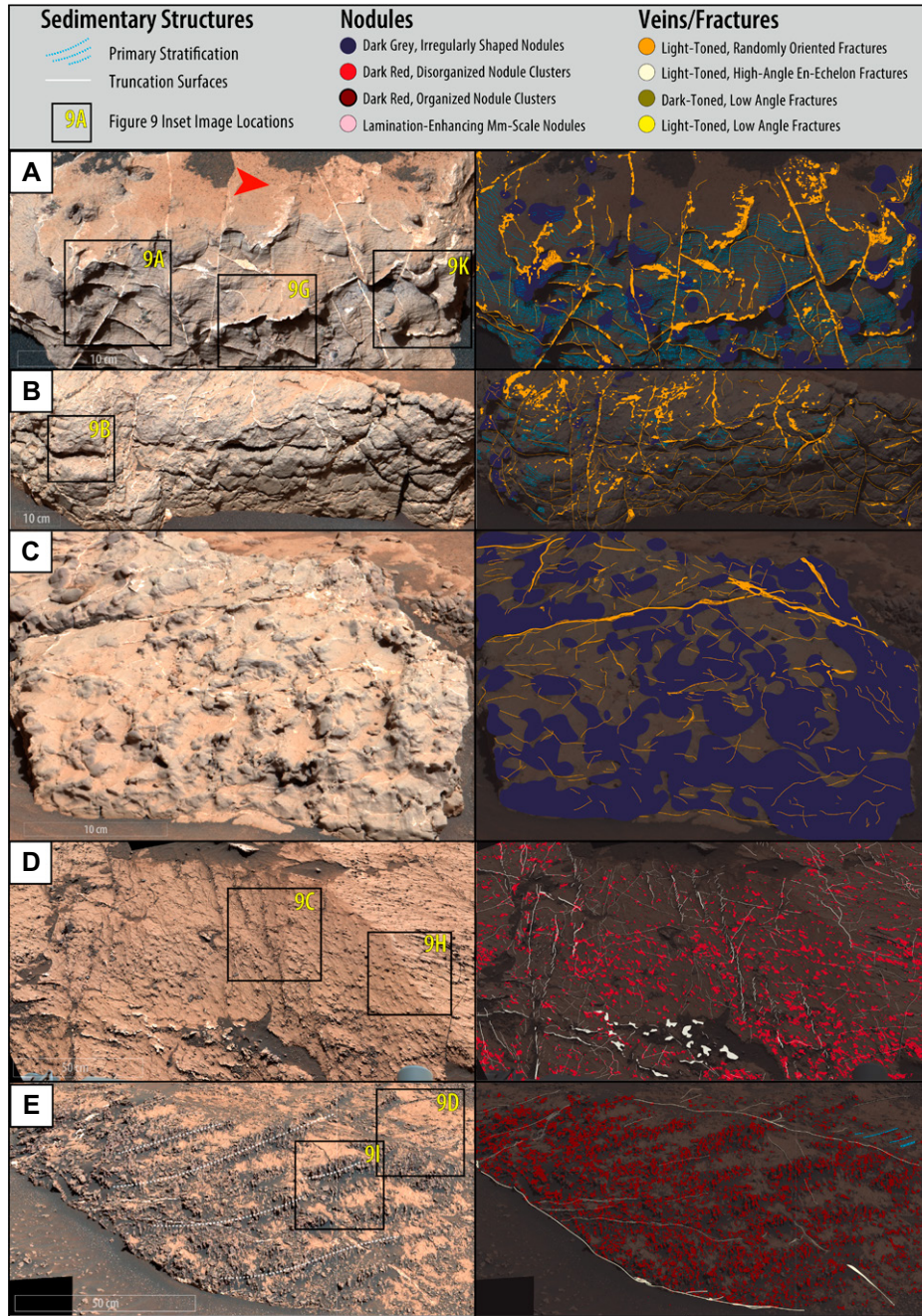


Figure 8. Examples of the range of sedimentary structures and diagenetic features observed in Mastcam workspace mosaics throughout the clay-sulfate transition region. The stratigraphic position for each image panel is noted on the stratigraphic column in Figure 7. See Data File S1-C2 for all Mastcam image sequence information (see text footnote 1). (A) Typical Glasgow member (Carolyn Shoemaker formation) outcrops showing faint, even millimeter-scale planar laminations (light-blue dashed lines) and dark-gray, irregularly shaped nodules (navy polygons), both of which are crosscut by abundant light-toned, randomly oriented veins/fractures (orange polygons). (B) Outcrop character of the Pontours member within the Carolyn Shoemaker formation just above Mont Mercou, showing hints of even millimeter-scale planar laminations (light-blue dashed lines), dark-gray, irregularly shaped nodules (navy polygons), and pervasive light-toned, randomly oriented veins/fractures (orange polygons). Note the similarities between this outcrop and that of panel A, suggesting some continuity between the outcrops just above and below Mont Mercou. (C) A few meters up section from panel B within the Pontours member of the Carolyn Shoemaker formation, the dark-gray, irregularly shaped nodules (navy polygons) and light-toned, randomly oriented veins/fractures (orange polygons) increase in intensity, and faint hints of millimeter-scale planar laminations diminish. (D) Outcrop typical of the middle portion of the Pontours member of the Carolyn Shoemaker formation. Outcrops notably lack indications of primary stratification and instead are overprinted by pervasive dark-red, disorganized nodule clusters (bright-red polygons and inset Fig. 9H) and light-toned, high-angle, en-echelon veins/fractures (white polygons). (E) Outcrops near the Pontours workspace (see Fig. 5D for panel location relative to the Pontours drill-hole location) are pervasively overprinted by the dark-red, organized nodule clusters (dark-red polygons) and crosscutting light-toned, high-angle en-echelon veins/fractures (white polygons). Organization of these nodules is linear (following white dashed lines) at the meter scale and subparallel to faint hints of laminations (blue dashed lines). At the submeter scale, these nodules are also organized into dendritic and branching patterns. (F) Outcrop near the Pontours workspace (see Fig. 5D for panel location relative to the Pontours drill hole) showing pervasive overprint of the dark-red, organized nodule clusters (dark-red polygons) and crosscutting dark-toned, low-angle veins/fractures (dark-yellow polygons). Both diagenetic populations are further crosscut by the light-toned, high-angle, en-echelon veins/fractures (white polygons). (G) Outcrop near the Pontours workspace (see Fig. 5D for panel location relative to the Pontours drill hole) showing pervasive overprint of the dark-red, disorganized nodule clusters (bright-red polygons) and crosscutting light-toned, high-angle, en-echelon veins/fractures (white polygons) showing a single preferred orientation. (H) Example of outcrop within the Dunnideer member of the Mirador formation showing hints of low-angle cross-stratification (see light-blue dashed and white solid lines) strongly overprinted by the dark-red disorganized nodule clusters (bright-red polygons). (I) Example of outcrops in the Dunnideer member of the Mirador formation showing pervasive overprint by the lamination-enhancing, millimeter-scale nodule population (light-pink polygons). (J) Example of light-toned, low-angle fracturing (yellow) within the Port Logan member of the lower Mirador formation. (K) Example of outcrops in the Port Logan member of the Mirador formation showing pervasive low-angle cross-stratification (see light-blue dashed and white solid lines).

Pontours drill-hole location) are pervasively overprinted by the dark-red, organized nodule clusters (dark-red polygons) and crosscutting light-toned, high-angle en-echelon veins/fractures (white polygons). Organization of these nodules is linear (following white dashed lines) at the meter scale and subparallel to faint hints of laminations (blue dashed lines). At the submeter scale, these nodules are also organized into dendritic and branching patterns. (F) Outcrop near the Pontours workspace (see Fig. 5D for panel location relative to the Pontours drill hole) showing pervasive overprint of the dark-red, organized nodule clusters (dark-red polygons) and crosscutting dark-toned, low-angle veins/fractures (dark-yellow polygons). Both diagenetic populations are further crosscut by the light-toned, high-angle, en-echelon veins/fractures (white polygons). (G) Outcrop near the Pontours workspace (see Fig. 5D for panel location relative to the Pontours drill hole) showing pervasive overprint of the dark-red, disorganized nodule clusters (bright-red polygons) and crosscutting light-toned, high-angle, en-echelon veins/fractures (white polygons) showing a single preferred orientation. (H) Example of outcrop within the Dunnideer member of the Mirador formation showing hints of low-angle cross-stratification (see light-blue dashed and white solid lines) strongly overprinted by the dark-red disorganized nodule clusters (bright-red polygons). (I) Example of outcrops in the Dunnideer member of the Mirador formation showing pervasive overprint by the lamination-enhancing, millimeter-scale nodule population (light-pink polygons). (J) Example of light-toned, low-angle fracturing (yellow) within the Port Logan member of the lower Mirador formation. (K) Example of outcrops in the Port Logan member of the Mirador formation showing pervasive low-angle cross-stratification (see light-blue dashed and white solid lines).

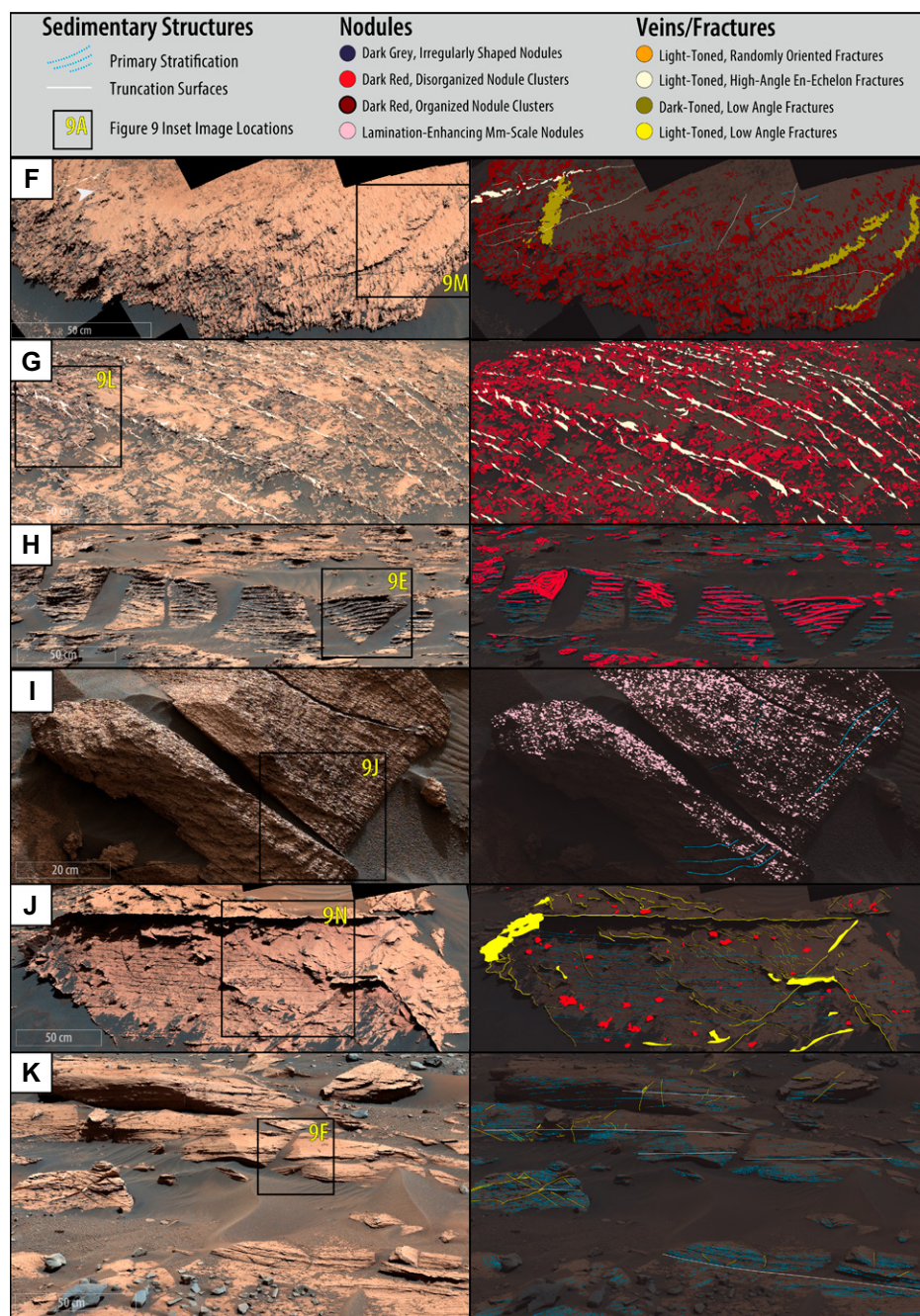


Figure 8. (Continued)

Disorganized, variably sized clusters of dark-toned and red-colored nodules are present in the lower portion of the Pontours member (Figs. 7 and 8D; red arrows in Figs. 9H; see Fig. S1-A18B). These “disorganized” nodule clusters are often patchily distributed across the bedrock (see also Seeger et al., 2023). Near the top ~5 m of the Pontours member, a similar but more organized nodule population overprints the bedrock (Figs. 7 and 8E; dark-red arrows in Fig. 9I; Fig. S1-A18B). These are

generally larger (centimeter-sized) and organize into subparallel lines at the meter scale (e.g., dashed white lines in Fig. 8E). Although lamination visibility in this region is generally poor, the linear orientation of this “organized” nodule population appears to loosely conform to bedding orientations where hints of laminations are apparent (e.g., compare orientation of nodules along dashed white lines in Figure 8E to dashed blue lines tracing laminations in companion annotation panel). These hints of lami-

nations are often traceable through sufficiently large clusters of these nodules (white arrows in Figs. 9I and 9M).

The Pontours member is also overprinted by a distinct set of light-toned, en-echelon fractures that crosscut both bedrock and nodules at relatively high angles (light-yellow arrows in Fig. 9L; see also Seeger et al., 2023). Though not common, in the lower portion of the Pontours member, these fractures sometimes show a clear set of preferred orientations and occur as branching or curvilinear features (e.g., Fig. 8D). Toward the top of the Pontours member, these high-angle fractures become more organized into subparallel lines in a single orientation, termed “tiger stripes” by Seeger et al. (2023). Low-angle fractures and veins are also common throughout the Pontours member but are more difficult to isolate due to the dominant presence of the en-echelon fracturing. In some locations, the nodules and fractures locally organize into polygonal shapes, as described in detail by Rapin et al. (2023) and Seeger et al. (2023). In general, the overarching characteristic of the Pontours member is extensive diagenetic overprinting.

#### Carolyn Shoemaker–Mirador Formation Boundary (Coincident with the Distinctive Scarp)

The orbitally identified distinctive scarp and its associated boundaries intersect the rover traverse route where the Pontours member of the Carolyn Shoemaker formation transitions to the Dunnideer member of the Mirador formation (Fig. 4; Fig. S1-A18B). This region is marked by intense diagenetic overprinting of the dark-red nodule populations and crosscutting en-echelon fracturing (Figs. 8E–8G). The lighter-to-darker color transition that is visible in orbital images (Fig. 4; Fig. S1-A18) and in rover panoramic views (e.g., Figs. 5A and 5B) coincides with the appearance of the organized dark-red nodules at the base of the distinctive scarp (Figs. 5D and 7; Fig. S1-A18B). This intense diagenetic overprinting, coupled with sand cover and the low slope of terrain, obscures almost all indication of primary stratigraphy along the rover traverse path in this region. For this reason, it is not possible to determine unambiguously if the surface identified in mounds A and B and face A is also present in lateral equivalents at the rover traverse. However, similarities exist between mound A and mound C, located less than 10 m from the rover traverse near the Pontours location, laterally adjacent to the distinctive scarp base. Similar to mound A, mound C becomes distinctly darker in color (yellow arrow in Fig. 6F) above a horizon (pink arrows in Fig. 6F).

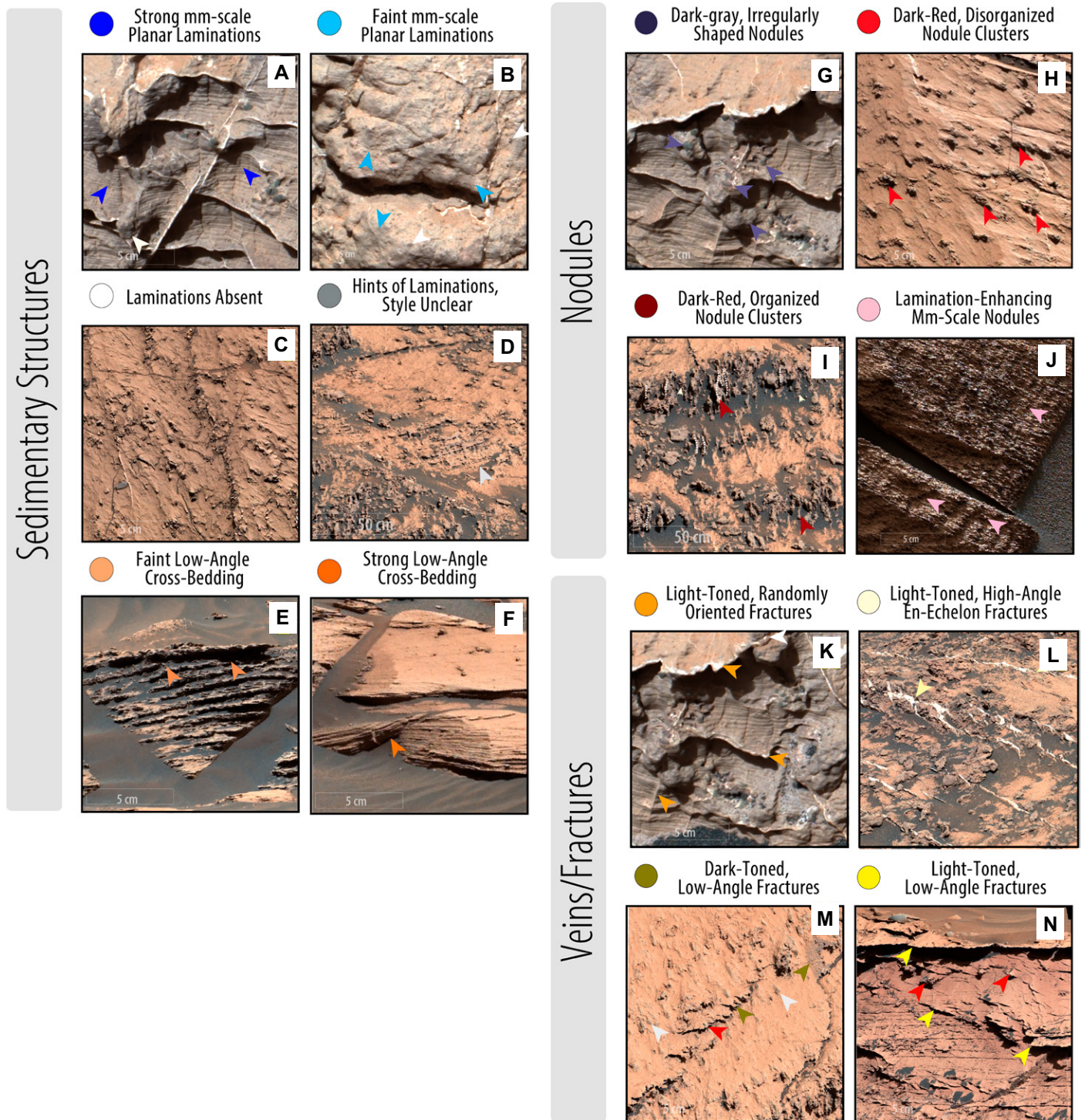


**Figure 9.** Type examples, inset from Figure 8 panels, of sedimentary structures (A–F), nodules (G–J), and veins/fractures (K–N) recognized in this study. (A) Strong millimeter-scale planar laminations (blue arrows), inset from Figure 8A. (B) Faint millimeter-scale planar laminations (light-blue arrows), inset from Figure 8B. (C) Absent laminations, inset from Figure 8D. (D) Hints of laminations (gray arrows), style unclear, inset from Figure 8E. (E) Faint low-angle cross-bedding (light-orange arrows), inset from Figure 8H. (F) Strong low-angle cross-bedding (orange arrows), inset from Figure 8K. (G) Dark-gray, irregularly shaped nodules (dark-blue arrows), inset from Figure 8A. (H) Dark-red, disorganized nodule clusters (red arrows), inset from Figure 8D. (I) Dark-red, organized nodule clusters (dark-red arrows), inset from Figure 8E. (J) Lamination-enhancing millimeter-scale nodules (light-pink arrows), inset from Figure 8I. (K) Light-toned, randomly oriented veins/fractures (orange arrows), inset from Figure 8A. (L) Light-toned, high-angle, en-echelon veins/fractures (white arrows), inset from Figure 8G. (M) Dark-toned, low-angle veins/fractures (dark-yellow arrows), inset from Figure 8F. (N) Light-toned, low-angle veins/fractures (yellow arrows), inset from Figure 8J.

## Dunnideer Member, Lower Mirador Formation

The intense diagenetic overprinting continues into the lower ~5 m of the Dunnideer member of the lower Mirador formation. As the organized nodules and en-echelon fracturing disappear up section, hints of laminations return, albeit with considerable overprint, making unambiguous interpretation of sedimentary structures difficult (Fig. 7; Fig. S1-A18). The first hints of low-angle cross-bedding in the low-slope rover workspaces appear at ~4036 m (e.g., light-orange arrows in Figs. 7, 8H, and 9E; Fig. S1-A18A). This observation is consistent with earlier predictions of eolian cross-bedding made in this region from long-distance imaging efforts (Rapin et al., 2021).

A new population of pervasive and lamination-enhancing millimeter-scale nodules (Figs. 8I and 9J) first appears at the base of this member and persists up section. Individual nodules are so small that they are easily misidentified as primary grains in the absence of MAHLI and RMI images. This member is also marked by two (dark- and light-toned) fracture populations that crosscut bedding at low angles. The dark-toned population occurs locally in the lower ~10 m of the Dunnideer member (e.g., dark-yellow arrows in Fig. 9M) and appears to crosscut the dark-red, organized nodules (e.g., red arrow in Fig. 9M) but is crosscut by the light-toned en-echelon fractures (white arrow in Fig. 8F). The light-toned, low-angle fracture population (e.g., yellow arrows in Fig. 9N) occurs throughout the Dunnideer member. Often nearly parallel to bedding, this fracture population can easily be misidentified as sedimentary structures in the absence of higher resolution or repeat imaging. Upon closer inspection, veins can be distinguished from primary stratification due to their higher resistance to weathering relative to the surrounding bedrock; they often form a protruding, platy, and fin-like morphology (Fig. 8J).

## Port Logan Member, Lower Mirador Formation

Low-angle, eolian cross-stratification becomes more apparent in the overlying sandstones of the considerably less diagenetically overprinted Port Logan member of the lower Mirador formation, particularly just above the Zechstein drill-hole workspace (e.g., yellow arrows in Fig. 9F; also see Gupta et al., 2022; Rapin et al., 2021, 2022, 2023). While cross-stratification is clearly present in parts of the Port Logan member, interpretations of grain size and sedimentary structures remain complicated by the presence of millimeter-scale nodules and light-toned, low-angle fractures. Disorganized,

dark-red nodule clusters occur only sporadically within this member (e.g., red arrows in Fig. 9N).

## Changes in Drill Sample Mineralogy

Several notable changes in drill sample mineralogy, as reported by the CheMin Team in Thorpe et al. (2022) and Rampe et al. (2023), occur between the Mary Anning drill region and the region where *Curiosity* entered the lower Mirador formation (Fig. 4). The Mary Anning, Mary Anning 3, and Groken drill samples are significantly clay-enriched (28, 30, and 30 wt%, respectively; Thorpe et al., 2022). In the overlying Nontron and Bardou drill samples, clay content falls to 18 and 12 wt%, respectively (Rampe et al., 2023). Pontours, drilled even higher up at the top of the Pontours member, has only 3 wt% clay minerals. Diffraction patterns collected on the Zechstein and Maria Gordon drill powders in the overlying Mirador formation lack evidence of clay minerals (Rampe et al., 2023).

Although the uncertainties on abundance of X-ray amorphous phases are large (~10 wt%, Rampe et al., 2023), their abundance generally increases in the samples above the Mary Anning region (Thorpe et al., 2022; Rampe et al., 2023). Total amorphous content in the Mary Anning, Mary Anning 3, and Groken drill samples is ~25 wt%. In the Nontron, Bardou, and Pontours samples, amorphous totals increase to ~40–50 wt%. Amorphous abundance remains elevated in the lower Mirador formation, totaling 54 wt% and 46 wt% in the Maria Gordon and Zechstein drill samples, respectively (Rampe et al., 2023). Total iron oxide/oxyhydroxide (hematite and goethite) content also increases above the Mary Anning region. Hematite occurs at trace levels or is absent in the bedrock sampled at Mary Anning, Mary Anning 3, and Groken (1.1, 0.9, and 0 wt%, respectively). Hematite and goethite occur in minor quantities (with combined abundances of 8, 8.4, 5.1, and 10 wt% in Nontron, Bardou, Pontours, and Maria Gordon drill samples, respectively). Calcium sulfates (gypsum, anhydrite, and/or bassanite) are present in minor quantities in all samples, with the exception of Zechstein, which has 18.2 wt% gypsum and 2.4 wt% bassanite (Rampe et al., 2023). Crystalline magnesium and iron sulfates are absent in X-ray diffraction (XRD) data in this portion of the stratigraphic section, indicating they are absent or present in abundances below the CheMin detection limit of ~1 wt%.

## CHARACTERIZATION OF BEDROCK AND DIAGENETIC FEATURES

The lithologic descriptions above introduced eight diagenetic feature classes in the clay-sul-

fate transition region (four nodule populations and four vein populations; see Figs. 8 and 9). We now provide additional details on the small-scale textural, compositional, and inferred mineralogical attributes for each of these classes, as well as for the local bedrock. For examples of textures and RMI images with stratigraphic position, see Figures S1-A19 through S1-A21. The average bulk composition and standard deviation of each bedrock and diagenetic feature class are presented graphically in Figures 10 and 11 and reported in Figure 12. For alternate versions of these figures highlighting each individual class, see Figures S1-A22 through S1-A41. We note that a wide range of diagenetic features has been observed along *Curiosity*'s traverse and in lower stratigraphic sections, and we refer readers to papers by Nachon et al. (2014), Sun et al. (2019), Kronyak et al. (2019), L'Haridon et al. (2020), Gasda et al. (2022), Bennett et al. (2023), and references therein, as examples of detailed descriptions of those features.

## Bedrock

Total bedrock measurements (Fig. 3; top row of Fig. 12) include individual LIBS point measurements that lack any obvious contribution from veins, fractures, nodules, sand, and/or loose pebbles at the scale of RMI images. This class is further chemically subdivided into two categories: typical bedrock and CaO-enriched bedrock (Figs. 3, 11, and 12).

## Typical Bedrock

Typical bedrock targets often do not show evidence for resolvable primary grains in RMI images (track c of Fig. S1-A20). While grain visibility is obscured in regions of pervasive diagenetic overprint, this observation also suggests that where laminations and bedrock are visible, the grain size is near or below what can be typically resolved in RMI images (on the order of 115  $\mu\text{m}$ ). The lack of grain visibility at RMI image resolution is not, however, diagnostic of a fine-grained lithology (e.g., mudstone, ~60  $\mu\text{m}$  and below), a designation that requires further MAHLI image analyses.

Typical bedrock composition is overall homogeneous throughout the studied region and is consistent with a basaltic sediment source (Figs. 10–12). However, small co-decreases in potassium (from  $1.28 \pm 0.5$  wt% to  $0.76 \pm 0.3$  wt%) and aluminum ( $11.07 \pm 1.3$  wt% to  $10.18 \pm 2.3$  wt%) begin near the top of the Glasgow member of the Carolyn Shoemaker formation. A subtle trend toward decreasing magnesium also occurs across the Glasgow member (from  $8.94 \pm 1.65$  wt% to  $5.48 \pm 2.2$  wt%) and persists up section. Typical

bedrock is otherwise homogeneous in composition with relatively narrow standard deviations for each element (Fig. 12).

The minor enrichments in potassium and aluminum in the Carolyn Shoemaker formation compared with the overlying Mirador formation may reflect the presence of a K- and Al-bearing phyllosilicate in the Carolyn Shoemaker formation. Though speculative, this interpretation is consistent with the presence of clay minerals in all drill samples analyzed by CheMin within the Carolyn Shoemaker formation (Thorpe et al., 2022; Rampe et al., 2022) and with interpretations of underlying strata made by previous studies (Mangold et al., 2019; Dehouck et al., 2022). It is intriguing that bedrock within portions of the Carolyn Shoemaker formation

examined in this study commonly exhibits a “shiny” appearance (track d of Fig. S1-A20), a characteristic that is particularly noticeable at the Mary Anning and Mary Anning 3 drill sites (e.g., Fig. S1-A19A), both of which contain a significant abundance of clay minerals (Thorpe et al., 2022). On Earth, this characteristic in fine-grained sedimentary rocks can indicate low porosity or the dominant occlusion of pores (e.g., Ajdukiewicz and Larese, 2012), and its presence in rocks of the Carolyn Shoemaker formation could be consistent with decreased porosity due to clays occurring as authigenic pore-filling cements. However, the images used in this study were not photometrically corrected, so interpretation of relative variations in brightness is subject to error and may be an

artifact of viewing geometry. Nevertheless, it is interesting that the “shiny” characteristic is not observed in all rocks/outcrops along *Curiosity*’s traverse, and future studies on this topic may be warranted to determine if this characteristic could be a useful proxy for degree of clay mineral cementation/decreased porosity and/or hardness. While a detrital origin for the clay minerals cannot be definitively ruled out in the absence of petrographic analyses, our favored interpretation—that at least some portion of the clay minerals within the Carolyn Shoemaker formation is authigenic—is consistent with previous studies of clay mineralogy within Gale crater (e.g., Vaniman et al., 2014; Grotzinger et al., 2014; McLennan et al., 2014; Bristow et al., 2018, 2021; Thorpe et al., 2022).

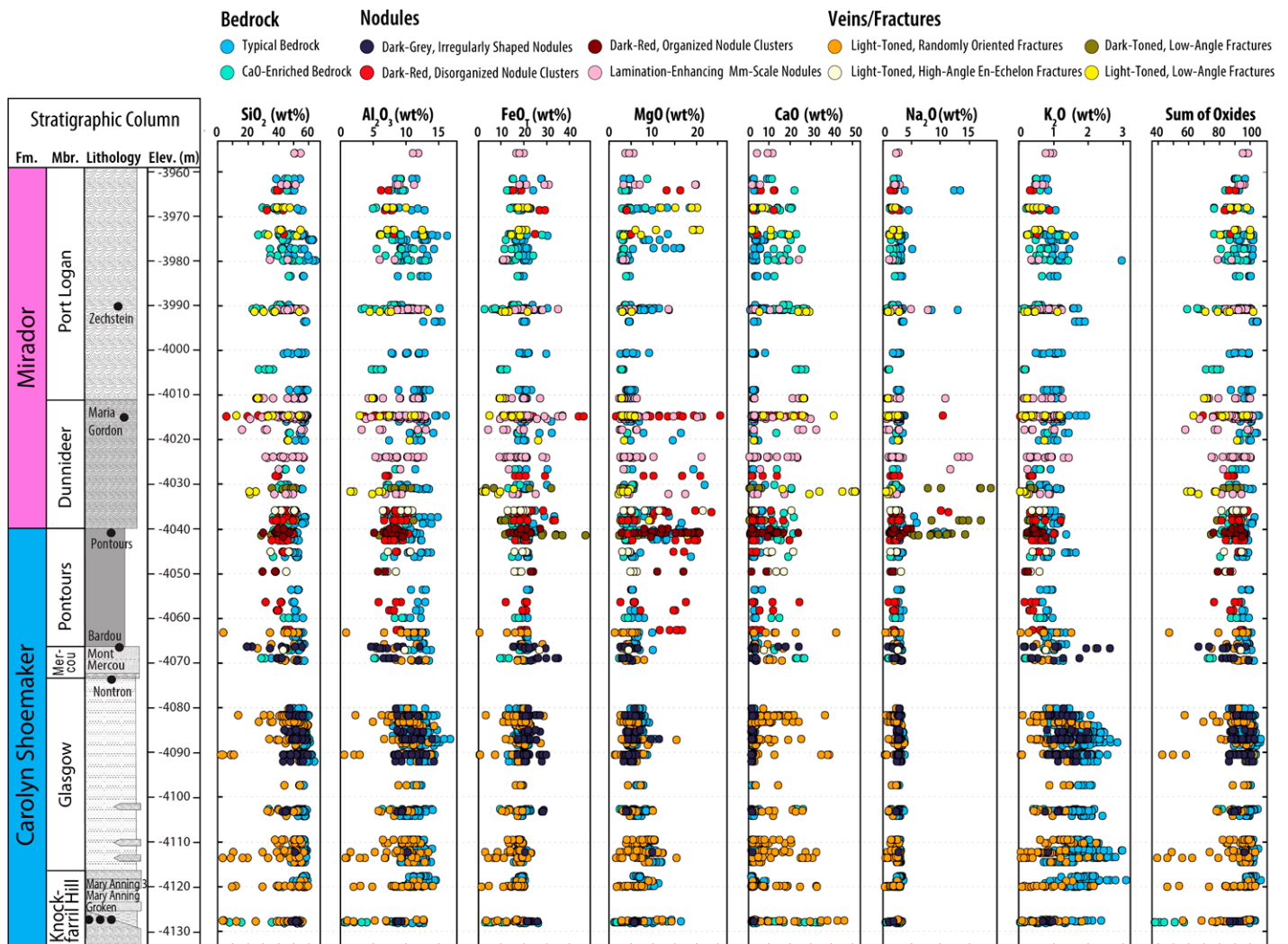
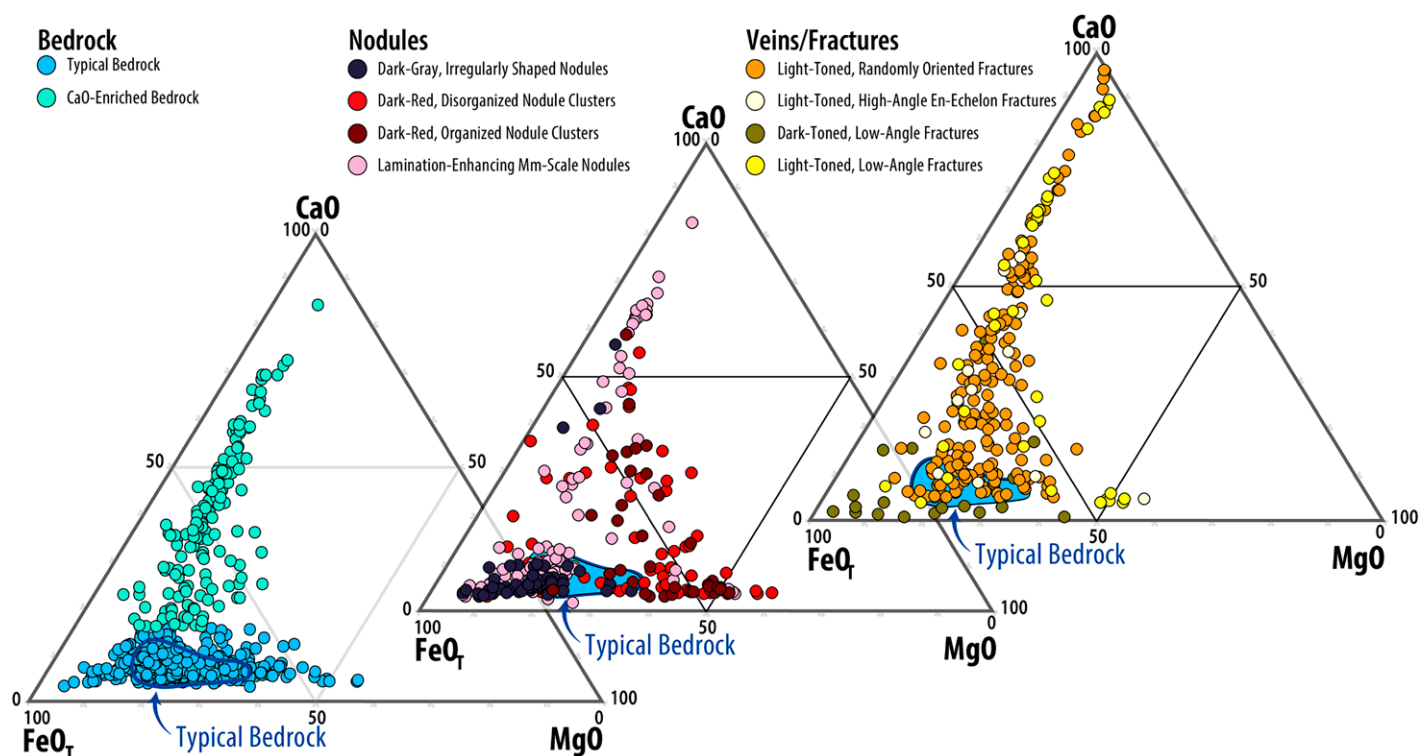


Figure 10. ChemCam laser-induced breakdown spectroscopy (LIBS) elemental data plotted against elevation along with the Mars Science Laboratory (MSL) Team stratigraphic column. Individual LIBS point measurements are colored by targeted geologic feature, as classified according to methods detailed in Figure 3. See Figures S1-A22 through S1-A41 for versions of this figure that highlight and isolate each individual geologic feature category for clarity (see text footnote 1). Note that much of the chemical variability observed in ChemCam data can be attributed to the presence of diagenetic features. Lithologic legend for MSL Team stratigraphic column is shown in Figure 7.



**Figure 11.** Separate CaO-FeO-MgO oxide ternary diagrams for bedrock, nodules, and veins/fractures showing ChemCam laser-induced breakdown spectroscopy (LIBS) elemental measurements, consistent with Figure 10 and data tabulated in Figure 12. Measurements are colored by targeted geologic feature, as classified according to methods detailed in Figure 3. Blue polygons on each ternary diagram mark the average composition of typical bedrock measurements. See Figures S1-A22 through S1-A41 for versions of this figure that highlight and isolate each individual geologic feature category for clarity (see text footnote 1).

It is also likely that at least some part of the X-ray amorphous component occurs as a cementing agent throughout the stratigraphic section, as amorphous materials have been identified in CheMin data from all drill holes to date (e.g., Thorpe et al., 2022; Smith et al., 2022; Rampe et al., 2020a, 2020b). Fe-oxide/oxyhydroxide cements may also be present in some cases (discussed further below).

#### CaO-Enriched Bedrock

Most common within the Mirador formation (Figs. 10–12), this category is differentiated from typical bedrock based solely on calcium enrichment beyond one standard deviation of the total bedrock average (i.e., 8.16 wt%; top row of Fig. 12). These targets are often visually indistinguishable from typical bedrock in RMI images (cf. Figs. S1-A19C and S1-A19D to S1-A19B). While the average chemistry remains largely basaltic, calcium enrichment in this class is coupled with a depleted sum of oxides (Fig. 12). Individual LIBS points classified as CaO-enriched bedrock often occur with typical bedrock points across a given target (e.g., Fig. S1-A19C and S1-A19D).

We interpret this class to represent typical (basaltic) bedrock that has been chemically modified by the localized addition of Ca-sulfate cement (or, alternatively, microscale diagenetic nodules) that is below the image resolution capabilities of *Curiosity's* payload, consistent with reports by Gasda et al. (2022) of Ca-sulfate cement in the Carolyn Shoemaker formation bedrock. Similar evidence for Ca-sulfate cement has been reported in the underlying Murray formation (e.g., Stein et al., 2018; Rapin et al., 2019; Thompson et al., 2020), and in some cases, significant amounts of Ca-sulfate have been interpreted to represent early diagenetic precipitation from saline brines (Rapin et al., 2019). However, previously, there have been no clear observations of primary evaporite beds, layers, or lenses during the ascent of Mount Sharp, and this remains true for the studied portion of the clay-sulfate transition region.

#### Nodules

Nodule measurements include individual LIBS points that sampled any apparently spherical, rounded, or irregularly shaped feature distinct in color, texture, and/or erosional resistance

from surrounding bedrock. They are grouped into four categories, and mineralogical inferences are based largely on CheMin results from the Maria Gordon drill hole. In all cases, we suggest at least some components were locally added to the composition of typical bedrock, suggesting these nodules are not fully replacive of the original basaltic sediment.

#### Lamination-Enhancing, Millimeter-Scale Nodules

This nodule population is pervasive in the Dunnideer member of the Mirador formation, particularly near the Maria Gordon drill-hole workspace, and common in the Port Logan member of the Mirador formation (Fig. 10). Nodules in this class are typically pervasive (track f of Fig. S1-A20), protruding (track h of Fig. S1-A20), sub-millimeter to millimeter in size (track g of Fig. S1-A20), and rounded in shape. They often conform to and enhance the visibility of primary laminations in bedrock (e.g., Figs. S1-A19K and S1-A19L; track b of Fig. S1-A20). This type of nodule is sometimes not easy to recognize in Mastcam images alone because of their small size and general pervasiveness, which give the appearance of

Feature Class	SiO <sub>2</sub> (wt%)	Al <sub>2</sub> O <sub>3</sub> (wt%)	FeO <sub>T</sub> (wt%)	MgO (wt%)	CaO (wt%)	Na <sub>2</sub> O (wt%)	K <sub>2</sub> O (wt%)	Sum of Oxides
<b>Bedrock</b>								
Total Bedrock Measurements <i>n</i> = 1,075 individual point measurements	52.01 ± 5.77	11.05 ± 1.79	18.51 ± 2.72	6.18 ± 2.31	3.47 ± 4.72	2.53 ± 0.88	1.29 ± 0.54	95.98 ± 5.52
● Typical Bedrock <i>n</i> = 927 individual point measurements	53.65 ± 3.43	11.46 ± 1.35	18.89 ± 2.2	6.54 ± 2.21	1.81 ± 0.65	2.66 ± 0.77	1.41 ± 0.48	97.39 ± 3.63
● CaO-Enriched Bedrock <i>n</i> = 152 individual point measurements	41.97 ± 6.91	8.57 ± 2.08	16.17 ± 4.06	3.99 ± 1.53	13.61 ± 5.99	1.73 ± 1.07	0.58 ± 0.32	87.39 ± 7.09
<b>Nodules</b>								
● Dark-gray, Irregularly Shaped Nodules <i>n</i> = 66 individual point measurements	47.59 ± 7.18	9.66 ± 1.96	22.46 ± 3.98	4.87 ± 1.61	2.27 ± 3.66	2.35 ± 0.43	1.2 ± 0.47	91.31 ± 6.81
● Dark-Red, Disorganized Nodule Clusters <i>n</i> = 65 individual point measurements	40.56 ± 7.48	7.82 ± 1.64	20.19 ± 6.21	10.73 ± 6.16	6.14 ± 6.57	2.09 ± 1.95	0.44 ± 0.22	88.76 ± 5.47
● Dark-Red, Organized Nodule Clusters <i>n</i> = 35 individual point measurements	40.3 ± 3.84	7.59 ± 1.00	19.2 ± 2.60	13.21 ± 5.07	5.59 ± 5.63	1.8 ± 0.79	0.43 ± 0.12	88.91 ± 4.40
● Lamination-Enhancing Mm-Scale Nodules <i>n</i> = 116 individual point measurements	46.84 ± 8.91	9.56 ± 2.33	18.77 ± 5.47	5.26 ± 3.98	6.57 ± 7.97	2.61 ± 2.4	0.7 ± 0.33	91.17 ± 8.49
<b>Fractures/Veins</b>								
● Light-Toned, Randomly Oriented Fractures <i>n</i> = 177 individual point measurements	44.64 ± 11.77	9.32 ± 2.77	16.41 ± 4.72	5.51 ± 2.59	10.02 ± 9.05	1.87 ± 0.69	0.93 ± 0.51	89.51 ± 12.6
● Light-Toned, High-Angle En-Echelon Fractures <i>n</i> = 12 individual point measurements	42.7 ± 5.34	8.5 ± 1.78	18.09 ± 3.56	6.56 ± 5.15	9.53 ± 6.87	1.93 ± 0.61	0.53 ± 0.21	88.6 ± 5.22
● Dark-Toned, Low-Angle Fractures <i>n</i> = 21 individual point measurements	42.5 ± 6.18	8.12 ± 1.44	19.78 ± 11.65	3.88 ± 2.05	1.7 ± 2.11	11.21 ± 4.13	0.3 ± 0.09	88.17 ± 5.16
● Light-Toned, Low-Angle Fractures <i>n</i> = 36 individual point measurements	34.09 ± 13.88	7.06 ± 2.87	14.19 ± 6.45	7.13 ± 6.21	18.04 ± 15.66	1.35 ± 0.74	0.41 ± 0.32	82.91 ± 11.77

Lowest	Column Value	Highest
--------	--------------	---------

**Figure 12. Average and standard deviation values for classes of ChemCam laser-induced breakdown spectroscopy (LIBS) standard elemental measurements acquired on in-place bedrock targets within the clay-sulfate transition region of *Curiosity*'s traverse and analyzed in this study. See Figure 3 and “Data Sets and Methods” section for classification methods. Note that the LIBS measurements average a stand-off distance of 2.68 m with a standard deviation of 0.34 m.**

somewhat smooth bedrock at the scale of those images. Due to their small size, they can easily be misidentified in Mastcam images as primary grains. However, they are discernible as nodules at the scale of RMI images, where they are clearly larger than grains of the host rock (Figs. S1-A19K and S1-A19L). When identifiable in images, they appear generally homogeneous in size, color, and shape.

MAHLI image analysis of this nodule population indicated further morphologic complexity. While the Maria Gordon drill-hole workspace contains only the lamination-enhancing, millimeter-scale nodule class (Figs. 13B, 14A, and 14B), the Helmsdale workspace (Berger et al., 2022) contains this type as well as the larger dark-red, disorganized nodule cluster population (Fig. 13C). MAHLI images of larger dark-red nodule clusters in the Helmsdale workspace, which were driven over and broken open by *Curiosity*, reveal lamination-enhancing, millimeter-scale nodules contained within them (Fig. 14C). Furthermore, analysis of color-stretched MAHLI images from both workspaces indicated that the lamination-enhancing, millimeter-scale nodules are composed of two subsets of small nodules (Figs. 14A–14C). The

first subset is a population of nodules that is dark in tone (black polygons in Figs. 14A–14C). The second population of nodules is lighter in tone, with two distinct lighter-toned materials inside (gray and white polygons in Figs. 14A–14C).

By polygon area calculation, the Maria Gordon drill-hole surface (white dashed circle) shown in Figure 14A is estimated to be composed of ~8% darker-toned nodules (black polygons), ~7% lighter-toned nodules (gray and white polygons), ~12% plucked nodule holes (yellow dashed outlined polygons), and ~13% red halos (red polygons). We suggest the plucked nodule depressions likely contained both darker- and lighter-toned subpopulations prior to surface abrasion. In total, these diagenetic features account for ~40% of the surface of the imaged drill-hole wall. Across the Maria Gordon drill surface, the dark-toned nodules are surrounded by millimeter-scale red halos (dashed red polygons in Fig. 14A). Within the freshly broken surfaces of the Helmsdale nodules, both lighter- and darker-toned, millimeter-scale nodules are also completely enveloped in a similarly red-colored matrix (red polygons in Fig. 14C).

Because drilled samples delivered to CheMin originate from depths of a few centimeters

within the drill hole (Rampe et al., 2020b), these quantitative areas cannot be assumed a priori to be representative of the quantities of diagenetic features incorporated into the powdered sample delivered to CheMin for XRD analysis. Although smeared by drill rotations, the nodular fabric clearly extends into the walls of the drill hole with evidence that nodules have been plucked from the hole walls and likely incorporated into the drill powder (Fig. 14B). We suggest that an amount of this nodule material above the level required for detection in CheMin is represented in Maria Gordon's derived mineral assemblage, which is reported as 23.8 wt% plagioclase, 2.8 wt% potassium feldspar, 3.5 wt% pyroxene, 0.7 wt% quartz, 7.5 wt% hematite, 2.5 wt% goethite, 2.2 wt% anhydrite, 2.0 wt% bassanite, 1.0 wt% gypsum, and 54 wt% amorphous content (Rampe et al., 2023).

ChemCam measurements of these nodules indicate a chemical complexity consistent with the morphologic observations (Figs. 3 and 10–12). Nodules show enrichments in iron, calcium, and/or magnesium, each of which is always associated with a depleted sum of oxides. In all cases, levels of enrichment in these metal cations are suggestive of the minor

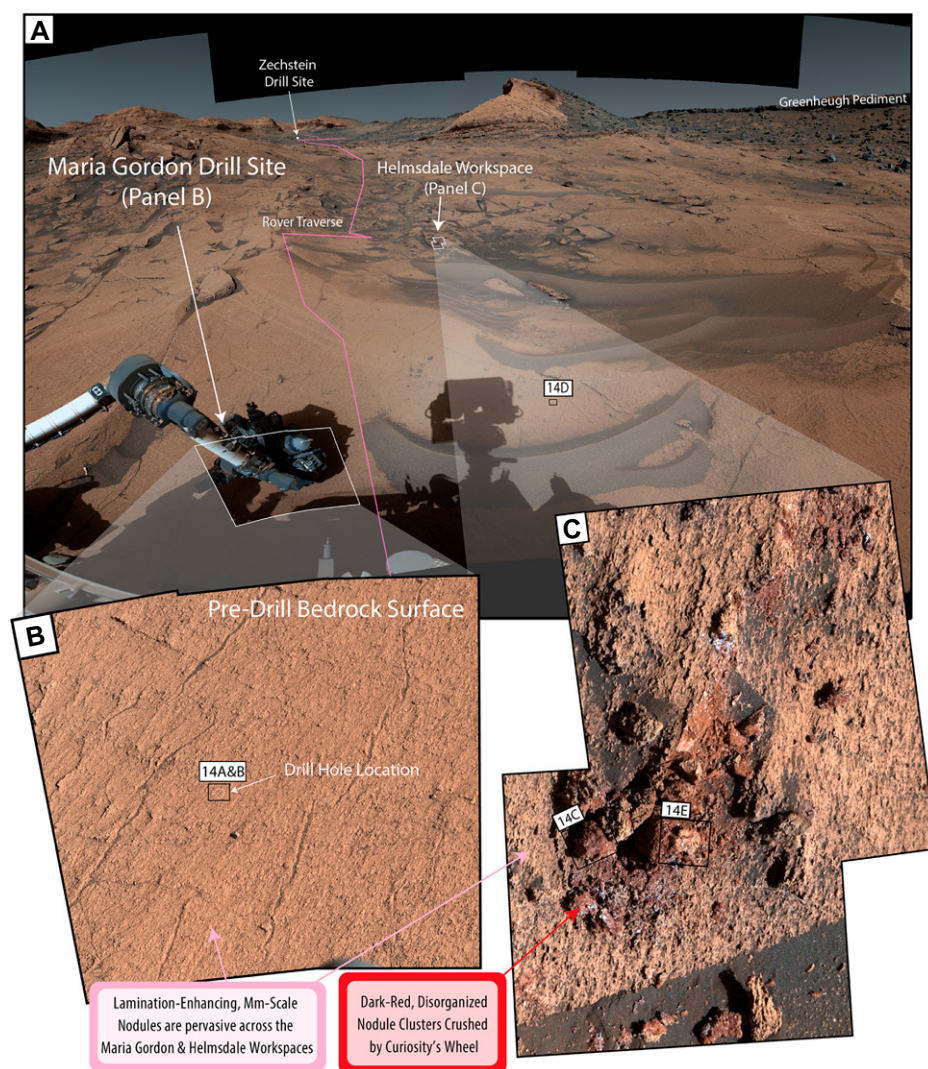


**Figure 13.** Maria Gordon and Helmsdale workspace locations. See Data File S1-C2 for all Mastcam image and sequence information (see text footnote 1). (A) Mastcam mosaic showing the Maria Gordon drill site and the nearby Helmsdale nodule crushing experiment. *Curiosity*'s approximate traverse within the Mirador formation is shown by the pink line. (B) Mastcam mosaic of the Maria Gordon drill-site location. Drill hole is shown by the white dashed circle. Note that workspace is pervasively covered by the lamination-enhancing, millimeter-scale nodule population. (C) Mastcam mosaic of the Helmsdale workspace, showing a population of large dark-red, disorganized nodule clusters that were crushed and broken by *Curiosity*'s wheel. Note this workspace is also pervasively covered by the lamination-enhancing, millimeter-scale nodule population.

addition of these components to the basaltic composition of typical bedrock. Across several point measurements within a given target, nodules often show heterogeneous enrichments in all three cations (e.g., Fig. S1-A19K; Fig. 14D). Typically, if a given LIBS point measurement is enriched in iron, it is depleted in calcium and magnesium (see gap in Fig. S1-A33 ternary). However, individual LIBS point measurements with magnesium enrichments commonly co-occur with calcium enrichments and vice versa.

This chemical diversity can be correlated to the morphologic subclasses. The dark-toned nodule subpopulation is enriched in iron with slightly depleted sum of oxides (e.g., blue arrow in Fig. 14A; blue arrow in Fig. 14D), suggesting the presence of an Fe-oxide/oxyhydroxide. Although amorphous Fe-sulfate cannot be definitively ruled out, we speculate that a component of the hematite and/or goethite detected by CheMin is the source of Fe enrichment in this nodule subclass and the associated red halos.

Interestingly, this type of lamination-enhancing, millimeter scale nodule shares a chemical and morphologic similarity with the Fe-bearing, dark-gray, irregularly shaped nodule class common in the Glasgow formation, discussed below (cf. dark-toned nodules in Figs. 8G, S1-A19E, and S1-A19F with dark-toned nodules in Fig. 14A).

The lighter-toned subpopulation is variably enriched in calcium and/or magnesium (Fig. 14D) with depleted sum of oxides, suggestive of the presence of both Mg- and Ca-sulfate. We interpret at least some of the anhydrite/bassanite/gypsum detected by CheMin to be associated with this subpopulation. If an Mg-sulfate phase were present in a crystalline form, then it should be above the detection limit of CheMin (~1 wt%; Blake et al., 2012; Rampe et al., 2020b) based on the mapped abundance of lighter-toned nodules across the drill target surface and drill-hole wall (Figs. 14A and 14B). Since no crystalline Mg-sulfate was detected in XRD patterns, we suggest the Mg-sulfate in these nodules exists in an X-ray amorphous state, as has been observed in laboratory experiments (Vaniman et al., 2014; Chipera and Vaniman, 2007), although likely in minor quantities. The interpretation that Mg-sulfate is present in the amorphous fraction of the Maria Gordon drill sample is consistent with sample analysis at Mars-evolved gas analysis (SAM-EGA) data for this drill sample (Clark et al., 2022), and X-ray amorphous Mg-sulfate has also been hypothesized to be present in previous drill samples analyzed by CheMin along *Curiosity*'s traverse (Smith et al., 2022). Alternatively, the Mg-sulfate in the nodules may be crystalline, but it becomes amorphous in the warm environment within the CheMin instrument (e.g., Chipera et al., 2023).

Finally, we note that relative proportions of the lighter- and darker-toned nodule subpopulations appear to show a stratigraphic dependence within the lower Mirador formation. In the Dunnideer member, Fe-bearing, dark-toned nodules and Mg/Ca-bearing, lighter-toned nodules appear in approximately equal proportions (e.g., Fig. 10; Figs. S1-A19K and S1-A32). In the overlying Port Logan member, particularly across the Zechstein drill workspace, the Fe-bearing, dark-toned subclass of nodules is more prevalent than the Mg/Ca-bearing, lighter-toned subclass (e.g., Fig. 10; Fig. S1-A19L and S1-A32). Nodules with enhanced Fe, Mg, and Ca were also observed down section in the Carolyn Shoemaker formation in the Glen Torridon region (Gasda et al., 2022) and on the Vera Rubin ridge (L'Haridon et al., 2020; David et al., 2020), indicating the fluids that gave rise to these features may have been widespread.

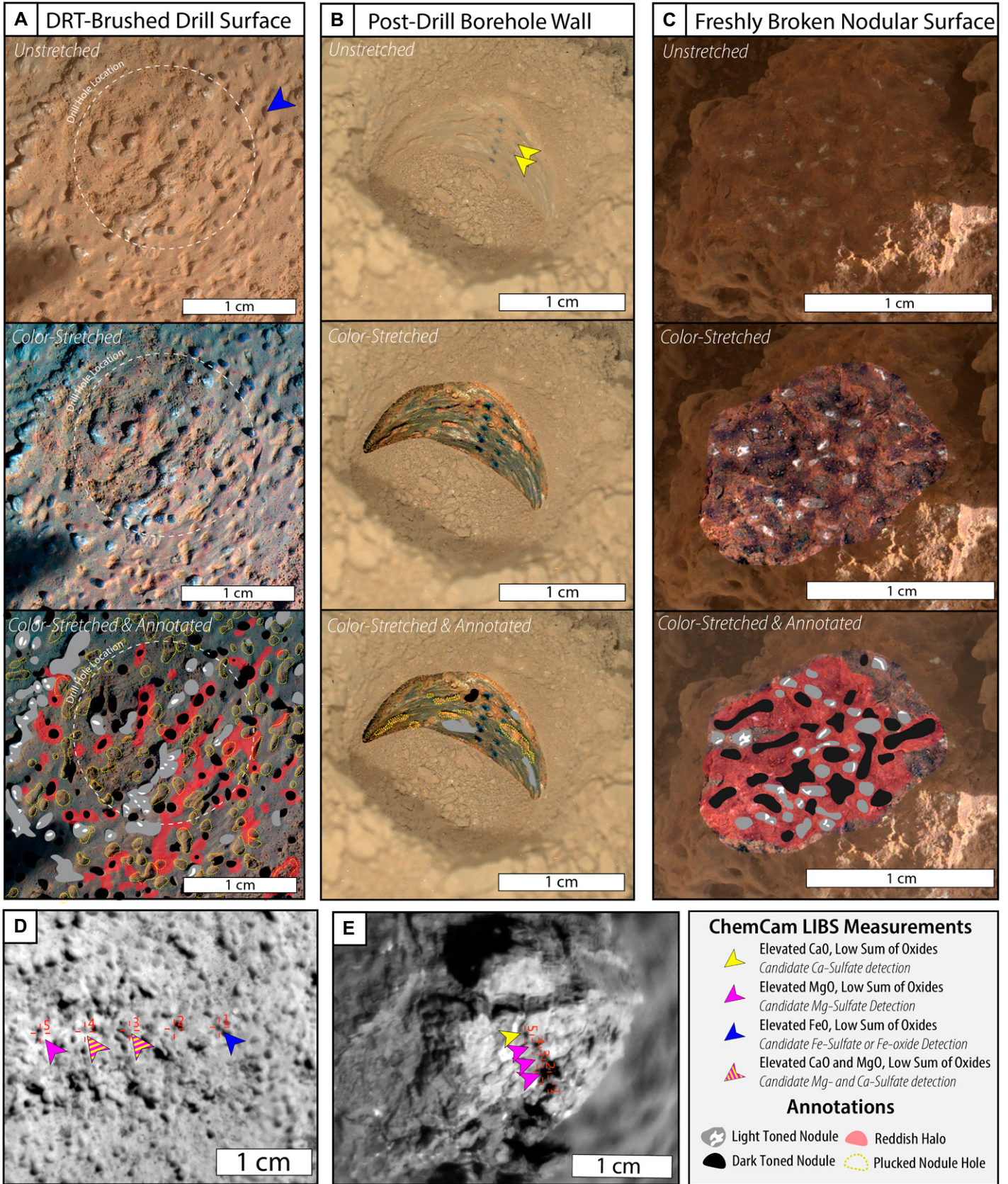


**Figure 14. Mars Hand Lens Imager (MAHLI) image analyses at the Maria Gordon and Helmsdale workspace locations. See Figure 13 for inset locations of each panel. (A) Unstretched, color-stretched, and color-stretched and annotated MAHLI images of the brushed Maria Gordon drill surface (see Fig. 13B for image location) that is pervasively covered by the lamination-enhancing, millimeter-scale nodule population. Color stretching reveals lighter- and darker-toned subpopulations within this nodule class. MAHLI image shown is 3224MH0007060011103370C00. (B) Unstretched, color-stretched, and color-stretched and annotated MAHLI images of the Maria Gordon drill-hole wall (see Fig. 13B for image location), showing further evidence for plucked nodules. MAHLI image shown is 3246MH0004100011103455C00. (C) Unstretched, color-stretched, and color-stretched and annotated MAHLI images of a freshly broken large nodule from the dark-red, disorganized nodule cluster population in the Helmsdale workspace (see Fig. 13C for image location). Color-stretched images of the broken surface reveal the lamination-enhancing, millimeter-scale nodule population contained within these larger dark-red clusters (e.g., compare the morphologic similarity between annotations in panels A and C). MAHLI image shown is 3273MH0001710001103559R00. (D) ChemCam Remote Micro Imager (RMI) image of Holoman Island target close to the Maria Gordon drill site (see Fig. 13A for RMI image location), which is pervasively covered in the lamination-enhancing, millimeter-scale nodule population and shows evidence for candidate Mg-sulfate, Ca-sulfate, and Fe-oxide/oxyhydroxide and/or Fe-sulfate. See Data File S1-C3 for the sequence identifications for RMI and Mastcam images associated with this target (see text footnote 1). (E) ChemCam RMI image of Helmsdale Boulder Beds ccam2 target in the Helmsdale workspace (see Fig. 13C for RMI image location), which contains a broken dark-red nodule cluster and shows evidence for candidate Mg- and Ca-sulfate. See Data File S1-C3 for the sequence identifications for RMI and Mastcam images associated with this target (see text footnote 1).**

### **Dark-Gray, Irregularly Shaped Nodules**

This nodule class is dark in tone, gray in color, and irregular but generally rounded in shape (Figs. S1-A19E and S1-A19F). Examples are most common in the upper ~20 m of elevation within the Glasgow member (Fig. 10). There, nodules vary in abundance, ranging from absent to pervasive (track f of Fig. S1-A20). They also vary in diameter from sub-millimeter (e.g., Fig. S1-A19F) to a few millimeters (e.g., Fig. S1-A19E; track g of Fig. S1-A20). Nodules almost always protrude from the surrounding bedrock (track h of Fig. S1-A20) and can sometimes appear shiny (e.g., Fig. S1-A19F). No systematic organized distribution or growth fabric is observed within this nodule class. Nodules almost always occur with, and are often crosscut by, the light-toned, randomly oriented fracture population (e.g., Fig. S1-A19F; Fig. 8A).

This nodule population exhibits minor enrichments in iron and is somewhat depleted in sum of oxides relative to typical bedrock (Fig. 12). The chemical differences between these nodules and the surrounding typical basaltic bedrock are usually subtle and sometimes even indiscernible. Chemically similar to the Fe-enriched, dark-toned subpopulation of the lamination-enhancing, millimeter-scale nodules, we interpret these nodules to contain Fe-oxide/oxyhydroxide added to a typical bedrock composition, although amorphous Fe-sulfate cannot be definitively ruled out. Dark, irregularly shaped nodules, some of which exhibit Fe enrichment, have also been previously reported in underlying strata of the Carolyn Shoemaker and Murray formations (e.g., Sun et al., 2019; L'Haridon et al., 2020; David et al., 2020; Gasda et al., 2022; Bennett et al., 2023).

### **Dark-Red, Disorganized Nodule Clusters**

Most common within the Pontours member of the Carolyn Shoemaker formation and the Dunnideer member of the lower Mirador formation, these features are distinctly dark in tone and reddish in color and often consist of smaller nodules that are amalgamated or clustered together (Figs. S1-A19G and S1-A19H). Clusters can occur in isolation (e.g., Figs. S1-A19G) or as pervasive, connected masses (e.g., Fig. S1-A19H) with no systematic preferred orientation or organized distribution. Always protruding from the surrounding bedrock (track h of Fig. S1-A20), this nodule population can sometimes appear pitted or dimpled (e.g., Fig. S1-A19H). Nodules range from several millimeters to a centimeter in size (track g of Fig. S1-A20). As the last remnants of surrounding wind-abraded bedrock, these erosion-resistant nodules often accumulate as lag deposits across the terrain (e.g., Fig. S1-A19H).

Relative to typical bedrock chemistry, the dark-red disorganized nodule clusters are most often enriched in magnesium and to a lesser degree calcium, coupled with depleted sum of oxide values (Figs. 10–12). We interpret these nodules to contain components of Mg- and Ca-sulfate added to a typical basaltic composition, consistent with interpretations made by Rapin et al. (2022, 2023). Although not directly sampled by CheMin, the chemical similarities between this nodule class and the lighter-toned subclass of the lamination-enhancing, millimeter-scale nodule population suggest that amorphous Mg-sulfate may be present in this nodule class.

### **Dark-Red, Organized Nodule Clusters**

Occurring pervasively in the ~10 m rover elevation interval at the boundary between the Carolyn Shoemaker formation and the lower

Mirador formation (Figs. 10 and 11), this nodule population is similar in tone, color, erosional resistance, and composition to the dark-red, disorganized nodule population. However, these nodules are organized at the meter scale into subparallel lines that loosely follow bedding orientations (white dashed lines in Fig. 8E). At the centimeter scale, these nodules also form dendritic and branching patterns, as described by Seeger et al. (2023) (e.g., yellow dashed lines in Fig. 9I). Measuring several centimeters in size (track g of Fig. S1-A20), these organized nodules are typically larger than their disorganized equivalents and stand out as the largest nodule population observed in the study region (Fig. S1-A21). In the members where both dark-red nodule populations occur, variations in lamination visibility broadly correlate inversely with apparent size of diagenetic nodules (cf. track a to track g of Fig. S1-A20 across the Pontours member).

Chemically similar to the dark-red disorganized nodule population (Fig. 12), these nodules are enriched in magnesium and calcium and have depleted sum of oxide values relative to typical bedrock chemistry. We interpret these nodules to also have a component of Ca-sulfate and (likely amorphous) Mg-sulfate.

### **Veins/Fractures**

This class includes individual LIBS points that sampled any apparently filled or unfilled planar feature distinct in color, texture, and/or erosional resistance from surrounding bedrock, and it is further subdivided into four distinct morphologies (Figs. 3 and 9). All three types of light-toned (i.e., randomly oriented, high-angle en-echelon, and low-angle) vein/fracture populations are Ca-enriched with depleted sum of oxides. Thus, we interpret all light-toned vein/fracture populations

to be similarly enriched in Ca-sulfate. The compositions of these Ca-sulfate veins/fractures are in a family with those that have been observed in rocks throughout the ascent of Mount Sharp and are most consistent with late-stage (postlithification) diagenetic processes, in some cases clearly cutting through other diagenetic features (Grotzinger et al., 2014; Rapin et al., 2016; Nachon et al., 2014; Caswell and Milliken, 2017; Kronyak et al., 2019; Sun et al., 2019; L'Haridon et al., 2018; Das et al., 2020).

**Light-Toned, Randomly Oriented Veins/Fractures**

Ubiquitous in the mudstones of the Glasgow and Knockfarril Hill members (Fig. 10), this class of veins and fractures is recognized by their light tonality, chaotic orientation, and curvilinear nature (Figs. S1-A19 M and S1-A19N). Individual fracture widths range from hairline to centimeters in thickness. Fractures become particularly pervasive toward the top of the Glasgow member (track e of Fig. S1-A20), coincident with the appearance of the dark-gray, irregularly shaped nodules (e.g., Fig. S1-A19N). Hairline fractures can often appear unfilled at the scale of Mastcam and RMI images but show evidence for Ca enrichment when sampled by LIBS. Nevertheless, a large portion of these exhibits no change in tone or chemistry relative to typical basaltic bedrock (Fig. 11). Calcium enrichment (Figs. 10–12) is consistent with the presence of Ca-sulfate.

**Light-Toned, High-Angle, En-Echelon Veins/Fractures**

Pervasive within the Pontours member of the Carolyn Shoemaker formation, this fracture population crosscuts the bedrock at relatively high angles and appears light in tone. Individual overlapping step fractures are

typically several centimeters in length, linking together to form curvilinear fractures that span up to several meters (e.g., Fig. 8G). Widths of individual filled fractures range from hairline (e.g., Fig. S1-A19O) to several millimeters in thickness nearing the boundary between the Carolyn Shoemaker formation and the lower Mirador formation (e.g., Fig. S1-A19P). Chemical measurements (Figs. 10–12) suggest these fractures are chemically similar to the other light-toned fracture populations and contain Ca-sulfate.

**Light-Toned, Low-Angle Veins/Fractures**

Relatively common in the study region, this fracture population is light in tonality with low-angle orientation. Often nearly bed parallel (e.g., Fig. S1-A19S), this fracture population can be easily misidentified as sedimentary structures. Upon closer inspection, veins can be distinguished from primary stratification due to their higher resistance to weathering relative to the surrounding bedrock; they often form a protruding, platy, and fin-like morphology (Fig. S1-A19T). These fractures are compositionally similar to the other light-toned fracture populations and contain Ca-sulfate.

**Dark-Toned, Low-Angle Veins/Fractures**

Occurring locally at the base of the Dunnideer member of the lower Mirador formation, these fractures are distinctly darker in tone (Fig. 9M; Figs. S1-A19Q and S1-A19R). They commonly protrude from the surrounding bedrock at relatively low angles, forming platy, fin-like shapes with jagged edges. ChemCam measurements indicate they are enriched in sodium and iron and depleted in sum of oxides (Figs. 10–12), consistent with previously seen dark diagenetic features (L'Haridon et al., 2018; Gasda et al., 2022). The Na enrichment is suggestive of the

presence of halite, as reported by Meslin et al. (2022). Chlorine abundance, like sulfur, is not systemically provided in standard ChemCam reports, since these elements are challenging to quantify (e.g., Anderson et al., 2017). Halite was also detected by CheMin in trace quantities in the nearby Pontours drill sample (Rampe et al., 2022; Rampe et al., 2023). Although rare in comparison to those enriched in Ca-sulfate, halite-bearing veins/fractures have been encountered previously within Mount Sharp (Forni et al., 2017; Thomas et al., 2019; Meslin et al., 2022).

**PROPOSAL OF A REGIONAL UNCONFORMITY AT THE BASE OF THE MIRADOR FORMATION**

The distinctive and regionally correlative scarp identified and discussed in this study is best interpreted as an expression of a low-angle erosional unconformity or disconformity at the base of the Mirador formation. The gentle termination of overlying orbital layer boundaries onto the mapped surface (i.e., blue arrows in Figs. 2H and 2I), which we suggest to be evidence for an erosional surface at this layer boundary, is the primary basis on which we make this interpretation. The discrete surface that is throughgoing and traceable across the steep mound and cliff-face exposures adjacent to the Greenheugh Pediment (e.g., mounds A and B and face A in Figs. 6A, 6B, 6D, and 6E) is interpreted to be in situ evidence for this stratigraphic boundary (Fig. 15). While the proposed unconformity appears to be discretely traceable in these exposures, identification of its outcropping location is more complex and ambiguous directly along the low slope of *Curiosity's* traverse route and within the scarps imaged at a distance from Mont Mercou.

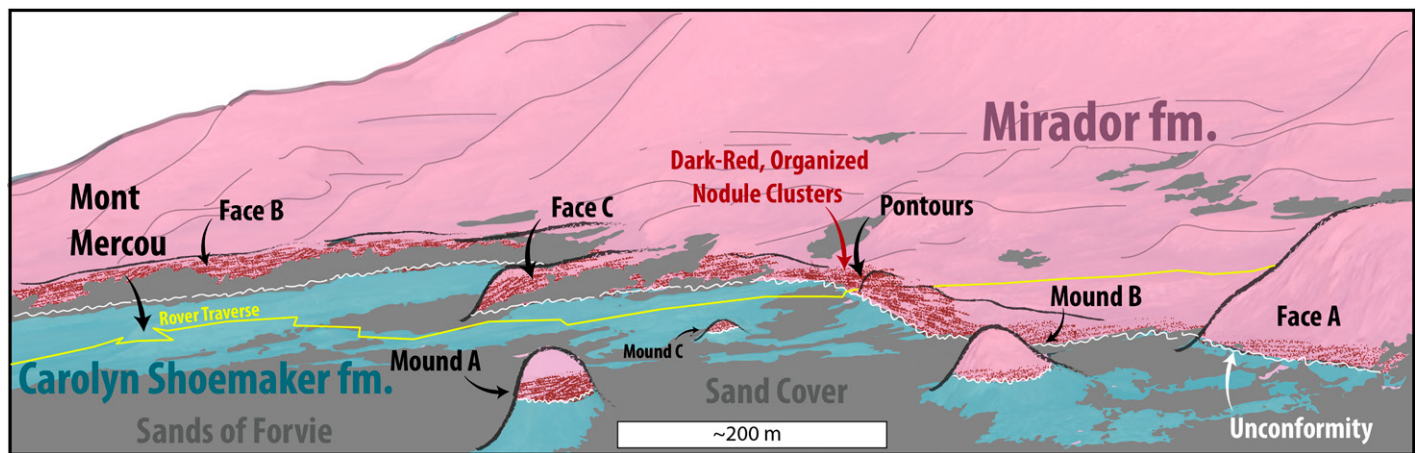


Figure 15. Sketch of proposed unconformity in relation to the distinctive scarp and dark-red, organized nodule cluster population.

**Correlation of the Basal Mirador Formation Unconformity to *Curiosity*'s Traverse Route**

The unconformity is interpreted to be regional and thus throughgoing across the study region, and though a boundary is clearly visible in rover images of multiple mounds/buttes, it is difficult to trace from face A (Fig. 6B) eastward toward *Curiosity*'s specific traverse route (Fig. 6C). This poor expression is consistent with the low slope of terrain (chosen for ease of rover mobility), sand cover, and strong diagenetic overprint (Fig. 15). However, the distinct changes in diagenesis with stratigraphic position observed along *Curiosity*'s traverse in this region offer insight into the likely location where *Curiosity* crossed this boundary. The first prominent occurrence (~4045 m elevation along the traverse route) of the dark-red organized nodule cluster population (Fig. 5D; dashed line in Fig. 7) may be where the rover actually intersected the unconformity.

In this scenario, the clear increase in size and pervasiveness of nodules may reflect a distinct up-section shift toward increased outcrop perme-

ability as *Curiosity* crossed into the eolian lower Mirador formation (Figs. 15 and 16B). Low-angle cross-bedded sandstones are clearly identifiable farther up section, but they might first appear here and are simply so strongly overprinted by this diagenesis that primary stratification is not readily apparent. Indeed, stratification becomes clearer where these nodules begin to decrease in prevalence ~10 m up section within the Dunningdeer member. Though speculative, the organized nature of this nodule population may result from preferential formation along laminations within a cross-bedded sandstone. Although subtle in this low-slope region, this location also marks *Curiosity*'s arrival at the base of the distinctive scarp identified from orbital data (white dashed line in Fig. 4; Fig. S1-A18). We note that the true stratigraphic boundary (erosional surface) presumably exists at the base of the distinctive scarp (Fig. 15), but the scarp top is often easier to trace in orbital images because the bottom contact is commonly obscured by sand and talus and thus is not reliably correlative over kilometer length scales.

The occurrence of the dark-red organized nodule cluster population immediately above

the proposed unconformity (at the base of the distinctive scarp) may influence the topographic slope and color changes observable across this boundary in far-field Mastcam images (Figs. 5A–5D) as well as broader-scale HiRISE images (Fig. S1-A18). The distinctive scarp top and bottom correspond broadly to locations where these large, pervasive, and protruding nodules occur along the lower-sloped rover traverse (e.g., Fig. 7; Fig. S1-A18B). Thus, a link may exist between scarp relief and this population of diagenetic features. The occurrence of these nodules may also contribute to the color change observed across this distinctive scarp. It is plausible that the dark-toned interval observable in mound A (yellow arrows in Figs. 6A and 6E) and mound C (yellow arrow in Fig. 6F) could correspond to a similar increase in the density of these dark-toned diagenetic features. In this case, the variable expression of the dark-toned interval (i.e., it is not obviously throughgoing across mound B and along face A in Figs. 6B and 6D) could indicate local heterogeneity in the pervasiveness of diagenetic features.

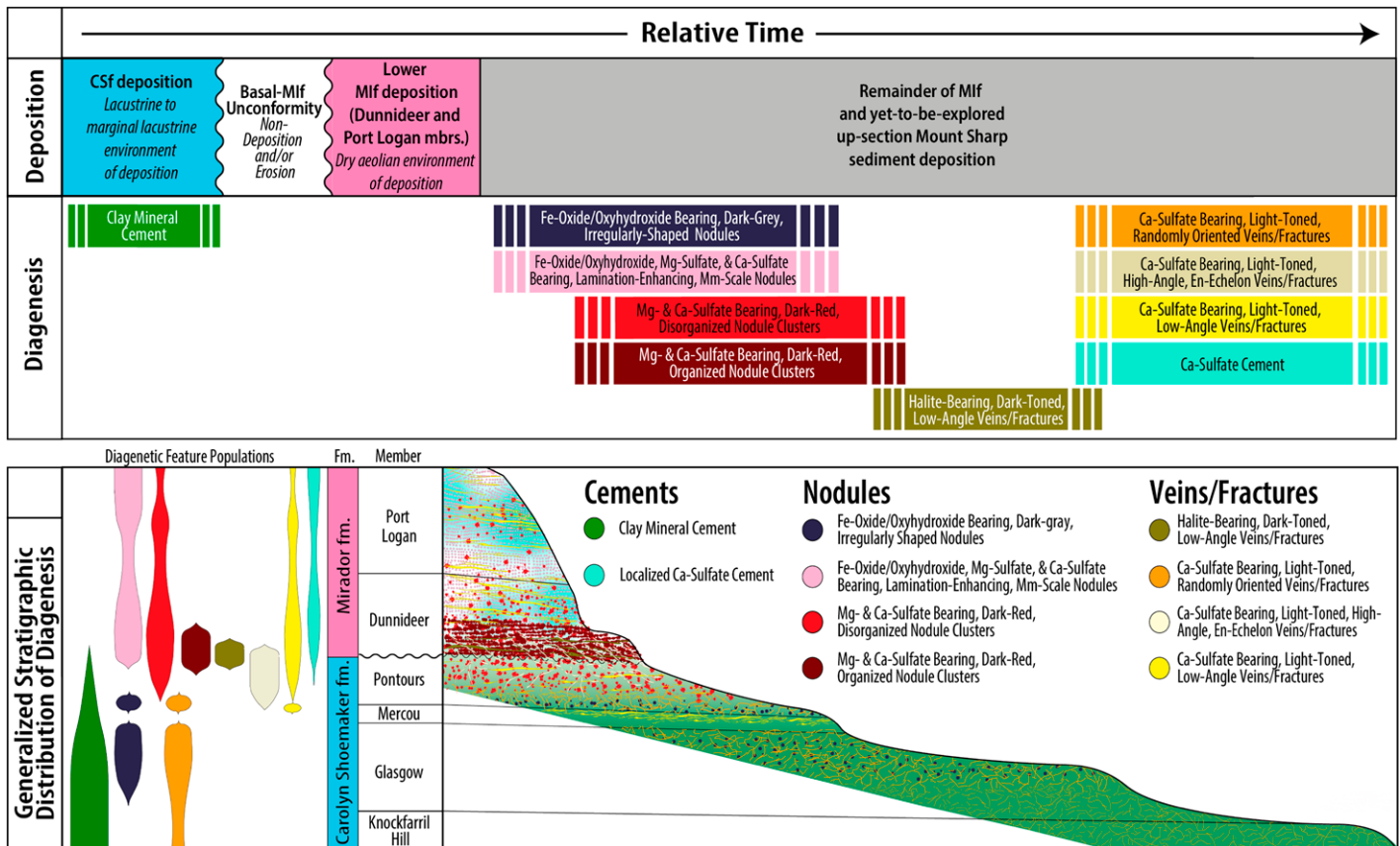


**Figure 16. Relative timing and generalized stratigraphic distribution of diagenetic features. (A) Relative time chart of Carolyn Shoemaker formation (CSf) deposition, proposed basal Mirador formation (Mif) unconformity duration, Mirador formation deposition, and all diagenetic features. (B) Generalized stratigraphic distribution of diagenetic features throughout the studied portions of the Carolyn Shoemaker and Mirador formations.**

The interpretation that the scarp's distinctive relief and color change result from increased diagenesis above a stratigraphic boundary is also consistent with its expression near Mont Mercou. There, the distinctive scarp top lacks clear indication of a stratigraphic surface. If strength of color change and topographic relief across the scarp are indeed correlated with nodule pervasiveness, then the darker color of the scarp faces in this region (particularly in face B; see Fig. 6G) suggests diagenetic overprinting must be strong at this location. The interpretation of an unconformity at the base of the scarps near Mont Mercou is also consistent with the (albeit ambiguous) mix of inclined and horizontal stratification observed within the scarp faces themselves (blue lines in Figs. 6G, 6H, and 6I). In this scenario, the strata within the scarp faces would be stratigraphically above the unconformity and laterally equivalent to the portion of the Dunnideer member of the Mirador formation that shows hints of low-angle cross-stratification (e.g., Fig. 8H).

### Implications for Missing Time in Mount Sharp Group Strata

The presence of a regionally extensive unconformity at the Carolyn Shoemaker–Mirador formation boundary suggests that the lacustrine/fluvial environment recorded in the Carolyn Shoemaker formation may have persisted for an unknown amount of time prior to the transition to the eolian environment recorded by the Mirador formation (Fig. 16A). In this scenario, the duration of potentially habitable aqueous conditions recorded by strata of the Murray and Carolyn Shoemaker formations represents a minimum estimate of persistently wet conditions in Gale crater. Although impossible to quantify the amount of missing time in the absence of precise radiometric age dating, the orientation of the proposed unconformity is only subtly different than the orientations of layers below and above the boundary ( $\sim 4.7^\circ\text{N}44\text{W}$  versus  $2.7^\circ\text{N}45\text{W}$  and  $3.0^\circ\text{N}44\text{W}$ , respectively). The small angular discordance observed at this boundary indicates relatively low paleorelief of the erosional surface, particularly when compared to the erosional unconformity at the base of the younger Siccar Point group (Watkins et al., 2022), where the orientation aligns closely with the modern-day topography and is suggestive of a significant hiatus.

Regardless of whether the unconformity represents a short or long period of missing time, its presence indicates a transition from net accumulation of sediment in a primarily aqueous environment to conditions marked by nondeposition/erosion and back to net accumulation but under markedly drier (eolian) conditions. Because the rock record is incomplete in this part of Mount

Sharp's stratigraphy, and because there are no absolute age dates, we cannot presently determine whether the transition from aqueous to eolian conditions was gradual or abrupt. Strata of the Carolyn Shoemaker formation include finely laminated lacustrine mudstones as well as sandy fluvial deposits, with the latter becoming more prominent up section toward the unconformity (Fedó et al., 2022; Caravaca et al., 2022a; Cardenas et al., 2022). This may reflect a decrease in lake level and inward migration of the shoreline or progradation and/or channel switching with no significant decrease in lake level (Cardenas et al., 2022). The uppermost member of the Carolyn Shoemaker formation (Pontours) shows very weak hints of fine laminations, possibly consistent with a return to a Glasgow-like lacustrine facies (Fig. 9B), and the mineralogical profiles just above and below Mont Mercou are also similar (Fig. S1–A20). These observations open the possibility that diagenetically overprinted Glasgow-like lacustrine deposition continued until  $\sim 4045$  m. Here, the first prominent occurrence of the dark-red organized nodule cluster population is recorded, which may reflect an increase in primary outcrop permeability as *Curiosity* crossed the proposed unconformity and entered the cross-bedded sandstones of the Mirador formation (Figs. 15 and 16B).

However, the strong diagenetic overprinting of what is currently identified as the Pontours member ultimately precludes a confident determination of depositional setting between the fluvial bar forms of Mont Mercou and the stratigraphic appearance of the unconformity. As such, the total duration of the lacustrine-fluvial-alluvial system preserved below the eolian Mirador formation remains unknown. Nevertheless, it is remarkable in that ancient Martian conditions resulted in the deposition of hundreds of meters of sediment under predominantly wet conditions, sediment that is now preserved in the Murray and Carolyn Shoemaker formations. Diagenetic overprinting is a key characteristic of strata throughout the clay-sulfate transition region, and most of the observed chemical variability in this region can be attributed to diagenetic features and processes. The inferred mineralogy and relative timing of the various diagenetic features are summarized in Figure 16A, and their generalized stratigraphic occurrence is shown in Figure 16B.

### ROLE OF WATER IN GALE CRATER AS RECORDED BY STRATA OF THE CLAY-SULFATE TRANSITION REGION

A major goal of *Curiosity*'s mission is to characterize and interpret the geological factors and ancient depositional environments that govern the orbitally inferred transition from clay-

bearing to sulfate-bearing strata within Mount Sharp. The results presented here demonstrate that strata of the clay-sulfate transition region record a long and complex history of water-sediment and water-rock interaction in Gale crater. For simplicity, this history can be broken into three categories: aqueous processes/alteration in the original sediment source region(s), aqueous processes during sediment transport and deposition, and water-related processes after deposition (i.e., early and late diagenesis). For the most part, the chemical and mineralogical data acquired by *Curiosity* do not preserve detailed textural information (e.g., ChemMin data are from bulk-rock powders, and fine-grained components are below the size of individual ChemCam LIBS points), or at least not at a scale that allows for unique and unambiguous interpretation of the relation between chemistry and mineralogy and the sedimentology in fine-grained rocks (e.g., Meyer et al., 2023). This complicates interpretation of the origin and timing of water-related processes, including determination of authigenic versus detrital origins of clay minerals. We acknowledge that some of the rover data can be interpreted multiple ways and do not intend to review all possibilities here. Rather, in this section, we discuss several key observations, present interpretations that are permissible by the integrated observations, and highlight outstanding questions.

### Water-Rock Interaction in Sediment Source Regions

Although exact sediment source regions are unknown, it is reasonable to assume they include the Gale crater walls/rim and possibly remnants of the central peak, as well as locations external to Gale crater (e.g., windblown sediment; Le Deit et al., 2013). Despite a significant change in depositional environment across the unconformity (lacustrine/fluvial/alluvial to eolian), the chemistry of the bedrock along this transition is quite homogeneous, an observation that is supported by both ChemCam (Rapin et al., 2022) and APXS (Berger et al., 2023) elemental data. Previous studies of the underlying Murray and Carolyn Shoemaker formations demonstrated that bulk bedrock compositions exhibit elevated Al and a relative decrease in Ca, Na, and K contents, which results in elevated chemical index of alteration (CIA) values (a proxy for degree of chemical weathering) that are consistent with open-system chemical weathering (Mangold et al., 2017; Frydenvang et al., 2020; Gasda et al., 2022). The bulk bedrock chemistry of the strata studied here is broadly similar, including elevated abundances of Al relative to more mobile elements, and thus it is also consistent

with some degree of chemical weathering. The origin of any chemical weathering may stem from processes in the sediment source region as well as postdepositional processes, including those that may have led to in situ clay formation (e.g., Bristow et al., 2018; Thorpe et al., 2022). In either case, the bedrock chemistry is distinct from the isochemical processes inferred for clay-bearing mudstones of the older Yellowknife Bay formation (McLennan et al., 2014).

It is also worth noting that the bulk compositions of eolian sandstones of the Mirador formation are distinct from the basaltic composition of eolian sandstones in the younger Stimson formation of the Siccar Point group, where the latter show no strong evidence for elevated Al or open-system chemical weathering (Berger et al., 2020). These differences in bulk chemistry between eolian sandstones in Gale crater may represent a decrease in open-system chemical weathering over time of sediment from a similar source region (i.e., from a decline in aqueous activity) or that eolian Mirador formation sediment was sourced from a fundamentally different region than eolian Stimson formation sediment.

Another possible explanation for this difference is that eolian sandstones in the Mirador formation may include reworked components of the eroded portion of the underlying Carolyn Shoemaker formation. The presence of a regionally extensive erosional conformity implies local generation of sediment via erosion, and it has been documented that a significant component of fluviably transported sand is present in the Carolyn Shoemaker formation (Caravaca et al., 2022a; Fedo et al., 2022; Cardenas et al., 2022). Fluviial sands and other sediment in what are now eroded portions of the Carolyn Shoemaker formation could have been reworked in a dry eolian system—ultimately becoming the lower portions of the Mirador formation—without changing the original, already altered bulk composition of the sediment. This would imply that the processes and products that cemented the reworked sediment also did not strongly influence bulk chemistry, as there is no evidence for chemically distinct cements between the Carolyn Shoemaker formation and Mirador formation (though the cements may be mineralogically distinct, as discussed below). In contrast, windblown sands of the younger Stimson formation may have come from basaltic sources outside of Gale crater. If *Curiosity* continues to encounter eolian sandstones during its climb of Mount Sharp, and if the bulk chemistry of the clastic component of such sandstone transitions to a more basaltic composition akin to the Stimson formation, then this could be consistent with a net transition from internal to external sediment sources.

In either case, the origin of the observed chemical difference in eolian sandstones in Gale crater is worthy of additional investigation. At a minimum, it suggests either differences in sediment source regions and/or a decrease in open-system chemical weathering through time, either in the source region(s) or postdeposition. Importantly, although the Mirador formation contains sediment that appears to have been deposited in a relatively dry eolian environment, the modern rocks exhibit a signature indicative of some degree of open-system chemical weathering/alteration. Some of this is likely associated with postdepositional alteration and cementation. Indeed, limitations of rover data make it difficult to determine unambiguously if the observed elemental signatures of chemical weathering represent processes in the sediment source region(s), alteration during fluvial transport, or postdepositional alteration.

Clay minerals are common products of surface weathering on Earth, so the presence of clays in the Carolyn Shoemaker formation and their apparent general absence in the lower Mirador formation are worthy of discussion. A defining characteristic of lacustrine and fluvial strata of the Murray and Carolyn Shoemaker formations is the general, though variable, presence of different clay minerals (e.g., Rampe et al., 2017; Bristow et al., 2018; Rampe et al., 2020a, 2020b; Thorpe et al., 2022; Dehouck et al., 2022). Understanding the nature and origin of these clay minerals continues to be an active area of research, particularly in terms of understanding whether or not certain clay minerals are likely authigenic or detrital. There are good arguments to be made for why at least some of the clay minerals in the Carolyn Shoemaker formation are authigenic (e.g., Bristow et al., 2019; Thorpe et al., 2022), but the evidence for some degree of open-system chemical weathering also permits the possibility that some of the clays may be detrital. In this case, and considering the scenario in which eolian sandstones of the lower Mirador formation include reworked (presumably fluvial) sand from the upper Carolyn Shoemaker formation, it is perhaps odd that the former would not also incorporate clay minerals. However, it is possible that (1) eolian erosion and reworking of Carolyn Shoemaker formation strata could have resulted in the preferential winnowing away of finer-grained, clay-rich material, especially if the clay minerals occurred as a fine-grained cement (see discussion below), (2) later diagenesis by sulfate-rich brines could have preferentially destroyed clay minerals (e.g., Bristow et al., 2021) within the lower Mirador formation, or (3) the volumetric abundance of clays in reworked sediment has been diluted by mixing with clay-poor sediment, such that it is

at or below the detection limit of CheMin in the lower Mirador formation.

Alternatively, sandstones of the lower Mirador formation may contain little or no reworked component of the now-eroded Carolyn Shoemaker formation and may instead represent a fundamentally different (clay-poor) source region, or clay minerals in the Carolyn Shoemaker formation beneath the unconformity could be authigenic and could have formed prior to erosion and deposition of the Mirador formation under different diagenetic conditions. Distinguishing between these possibilities with a high degree of confidence is not possible with only rover-based data, and defining clear trends in clay abundance with grain size (mudstone versus sandstone), transport mechanism (e.g., aqueous versus eolian transport of sand), and/or time of deposition remains challenging. Regardless of these complexities, a key observation in the clay-sulfate transition region, and one that has implications for orbital spectroscopic signatures, is that there is a distinct and strong decrease in clay abundance across the Carolyn Shoemaker formation–Mirador formation boundary.

In summary, the bulk bedrock compositions of strata in the clay-sulfate transition region and across the unconformity indicate some degree of chemical weathering, but it is challenging to determine how much of this may have taken place in the sediment source region. To date, orbital data of the Gale crater rim and walls do not show much evidence for clay minerals or other aqueous alteration products in these possible source regions (Buz et al., 2017), and transport distances were presumably limited, as there are no large fluvial transport systems leading into Gale crater. These observations contrast with those from other craters, which also host clay-bearing alluvial/fluviial/lacustrine deposits but which can be linked to clay-bearing source regions (e.g., Milliken and Bish, 2011; Goudge et al., 2015; Hughes et al., 2023), and it supports limited chemical weathering in the source region(s) for Carolyn Shoemaker formation and Mirador formation sediments.

### Aqueous Alteration of Sediment during Transport

If the sediment entering aqueous transport systems in ancient Gale crater was relatively unaltered and presumably mafic in composition, then it is possible it could have been chemically altered, even over short time scales and transport distances. As on Earth, such alteration would be highly dependent on the characteristics of the transporting fluids, though source-to-sink studies of basaltic sediment transport systems on Iceland have shown that mineralogical changes take

place even under cold conditions and relatively short transport distances (Thorpe et al., 2019). There is no robust information on what the transporting fluid characteristics would have been for Gale crater during the time period in which the clay-sulfate transition region formed, so any interpretations are highly speculative. However, McLennan et al. (2014) demonstrated that clay-bearing mudstones of the older Yellowknife Bay formation in Gale crater exhibited no clear evidence for open-system chemical weathering and that the detrital mud was effectively basaltic in character. Specifically, fine-grained mudstones of the Sheepbed member in the Yellowknife Bay region were shown to contain primary igneous minerals such as olivine that are more susceptible to alteration. These results indicated limited alteration during transport, and the clays in those mudstones were interpreted to have formed via in situ isochemical alteration (McLennan et al., 2014; Vaniman et al., 2014). This evidence of limited alteration during aqueous transport, and the general lack of aqueous alteration products in Gale crater wall/rim source regions (Buz et al., 2017), suggests that solute concentrations of fluvial waters in Gale crater may have been low. The same may have been true during the emplacement of the Carolyn Shoemaker formation, and we consider there to be no strong or direct evidence for appreciable alteration of sediment during transport within Gale crater. However, diagnostic signatures of such alteration may be subtle and cannot be entirely ruled out, and even limited interaction between water and fine-grained basaltic material may produce poorly crystalline phases at low abundances. This may be of particular note given the prevalence of complex and variable X-ray amorphous components in all samples drilled by *Curiosity* to date (e.g., Dehouck et al., 2014; Smith et al., 2021, 2022).

#### **Postdepositional Aqueous Alteration (Early and Late Diagenesis)**

There is compelling, albeit indirect, evidence that at least some of the clay minerals in the Mount Sharp group were formed during or shortly after deposition. While proposed mechanisms for clay authigenesis in Gale crater are varied, alteration of preexisting (either detrital or authigenic) clay minerals has been noted in several studies (e.g., Rampe et al., 2017; Bristow et al., 2018, 2019; Thorpe et al., 2022). Consistent with these previous studies and the absence of significant clays in the walls and rim of Gale crater, some of the clays in the Carolyn Shoemaker formation may be authigenic. We suggest that syndepositional or very early diagenetic clay cementation may have transformed the Carolyn

Shoemaker formation into a hydraulic barrier, particularly in contrast to the increased primary porosity and permeability of the overlying cross-bedded eolian sandstones of the lower Mirador formation. This contrast could have allowed later diagenetic fluids, e.g., those that gave rise to nodules, to percolate preferentially through Mirador formation sediments and become concentrated along the proposed unconformity.

In addition to clay minerals in the Carolyn Shoemaker formation, other cements present in the studied region likely include Ca-sulfate phases, as indicated by the presence of Ca-enriched bedrock targets, Fe-oxides/oxyhydroxides, and X-ray amorphous components. The origin and timing of the latter are difficult to constrain, but the lack of clay minerals or other obvious cementing agents in the Mirador formation suggests that amorphous components, along with Fe-oxides/oxyhydroxides, were the likely cementing agents in those rocks. These phases presumably formed during the initial lithification of the eolian sediment, but they may also have been altered at later times with progressive burial and/or later interaction with diagenetic fluids. If clay minerals and amorphous materials are both part of the cement of Carolyn Shoemaker formation strata, then the former may have formed very early, as discussed above, and the latter may have formed later under more water-limited conditions. Though separated by an erosional unconformity, it cannot be ruled out that some components of the amorphous material in the Carolyn Shoemaker formation and Mirador formation formed during the same event (e.g., late-stage interaction with pore fluids after all strata were lithified). Additional detailed studies are warranted to better understand the compositional similarities and differences of X-ray amorphous alteration materials across the Carolyn Shoemaker formation–Mirador formation boundary, given that their presence implies that some level of water-rock interaction continued to take place well after the region transitioned to a drier, eolian environment.

The observed relationships between primary laminations and individual nodules suggest that all nodule populations likely formed subsequent to deposition and lithification. In select places, faint laminations can be traced undisturbed through dark-gray, irregularly shaped nodules and also through clusters of dark-red organized nodules (i.e., white arrows in Fig. 9A; white arrows in Fig. 9I). Similar to results of Sun et al. (2019) for underlying mudstones of the Murray formation, we found no evidence for differential compaction of laminae around nodules that would suggest an early, preburial origin. The lamination-enhancing, millimeter-scale nodule population is often observed to conform to primary laminae

(Fig. S1-A19L), indicating primary deposition must have preceded nodule formation.

Observations made at the Helmsdale workspace near the Maria Gordon drill hole (Fig. 13) suggest that the lamination-enhancing nodule populations formed prior to the dark-red disorganized nodule clusters. If the darker-toned subclass within the lamination-enhancing nodule population is genetically related to the class of dark-gray, irregularly shaped nodules, it would suggest that these nodules also formed before the dark-red nodule clusters. Based on their similarities in color and composition, we suggest that the two dark-red nodule cluster populations formed contemporaneously as the last nodule-forming event in this region (Fig. 16A). The differences in organizational/spatial aspects of the nodule populations are interpreted to result from differences in primary porosity and permeability of their host rocks.

In the case of the Carolyn Shoemaker formation–Mirador formation contact in the clay-sulfate transition region, the dominant presence of diagenetic features and sulfate minerals at and immediately above the unconformity would be most consistent with a top-down migration of fluids that was eventually halted upon entry into the finer-grained and less permeable strata of the Carolyn Shoemaker formation. Top-down fluid migration could allow three nodule populations that are distinctly more enriched in Mg- and Ca-sulfate to preferentially precipitate in the more permeable Mirador formation. The disorganized and organized dark-red nodule populations could also have formed in response to increased porosity and permeability in sandstones at the base of the Mirador formation. The unconformity could also have promoted fluid flow and resulted in accumulation of notably larger nodules in this region. On Earth, unconformities can enhance postdepositional fluid flow (Huntoon et al., 1994) and consequently promote increased diagenesis (Al-Ramadan, 2021; Huntoon et al., 1994; Dolson et al., 1994; Swezey, 1991). As an example, this phenomenon is observed in the higher-permeability eolian foresets along the low-angle J-2 unconformity in Utah (Fig. S1-A42). Evidence of enhanced diagenesis along unconformities has been observed and inferred elsewhere in Gale crater, including along the younger Siccar Point unconformity at locations such as the Vera Rubin ridge and the Carolyn Shoemaker formation–Greenheugh Pediment (Stimson formation) contact (e.g., Frydenvang et al., 2020; Rampe et al., 2020a; Thompson et al., 2020; Fraeman et al., 2020; Dehouck et al., 2022; Gasda et al., 2022).

The prominence of diagenetic features enriched in Mg-sulfate in the clay-sulfate transition region, coupled with the lack of indica-

tion of local primary bedrock evaporite, may necessitate a more significant source of Mg and S, such as a primary Mg-evaporite, to be present in yet-to-be explored strata up section. In this scenario, fluids that remobilized elements from these up-section Mg-enriched sources could have migrated (downward and laterally) and preferentially concentrated and precipitated phases in the underlying clay-sulfate transition region. A logical source for such highly soluble, Mg-rich rocks would be locations where orbital Mg-sulfate signatures are strongest in the region above the marker band (Sheppard et al., 2021). Alternatively, Mg could have been sourced from local bedrock, as evident from the measurable (~3 wt%) decline in bedrock Mg occurring at ~4110 m where the Mg-sulfate-bearing nodules begin to appear just before crossing into the lower Mirador formation. In the case of Mg sourced from younger, up-section strata of Mount Sharp, this would imply that the Mg-sulfate nodules in the clay-sulfate transition region must have formed after the deposition of the up-section strata, which in turn would imply a timing that is much later than primary deposition and initial cementation of both the Carolyn Shoemaker formation and lower Mirador formation.

The presence of Fe-rich nodules and Fe-oxides/oxyhydroxides in the clay-sulfate transition region is further demonstration of the important role of Fe mobility in Mount Sharp strata (e.g., Hurowitz et al., 2017; Fraeman et al., 2020; Rampe et al., 2020a; L'Haridon et al., 2020; David et al., 2020; Gasda et al., 2022). A relatively young age for jarosite at the base of the Murray formation ( $2.1 \pm 0.4$  Ga, based on SAM-EGA K-Ar age dating by Martin et al., 2017) demonstrates that late diagenetic activity mobilized Fe in Gale crater. Several key observations are that the Fe-rich nodules occur as late (postlithification) diagenetic features and that some appear to be similar to dark Fe-rich features observed in underlying Mount Sharp strata. The specific oxidation state of the Fe is not known, but given the presence of ferric oxides and oxyhydroxides in the CheMin data and significant abundance of ferric clays (nontronite) and oxides in the underlying strata (Rampe et al., 2020a; Bristow et al., 2021; Thorpe et al., 2022), it is likely that some, perhaps most, of the Fe in the nodules occurs as  $\text{Fe}^{3+}$ . There is currently no clear indication that the pH values of fluids interacting with strata of the clay-sulfate transition region were unusually low or high to help mobilize significant amounts of  $\text{Fe}^{3+}$ . It is more likely that iron was aqueously transported as  $\text{Fe}^{2+}$ . In this context, late-stage formation of ferric alteration products at depth is intriguing in that it would imply somewhat reducing conditions, at

least locally. It is possible that  $\text{Fe}^{3+}$  in preexisting alteration products was somehow reduced, transported in solution, and later reoxidized to form Fe-oxides, but such a pathway is difficult to envision on Mars in the absence of significant reductants. Alternatively, deep basal fluids that were not in contact with an oxidizing surface environment (and thus were anoxic) may have locally dissolved  $\text{Fe}^{2+}$  from primary igneous phases and led to Fe-oxide precipitation upon later oxidation. The nature of such an oxidation event is speculative, but it could include interaction with atmospheric oxygen or oxygenated meteoric/groundwaters that had been in communication with the atmosphere. Additional work is clearly needed to better understand the oxidation state of Fe-rich diagenetic features throughout Mount Sharp, the large-scale distribution of such features, the likely length scales over which Fe was mobilized, and the drivers of redox processes through time. We simply note that the presence of late diagenetic, Fe-rich nodules in the clay-sulfate transition region continues to highlight the important role that redox-sensitive elements play in the geologic record of Mount Sharp.

All fracture populations in the clay-sulfate transition region are interpreted to postdate nodule formation. Our observations suggest two distinct generations of fracture filling occurred: an earlier generation of dark-toned, low-angle fractures followed by a later generation that includes all three morphologic classes of light-toned fracture populations (Fig. 16A). Fractures/veins within the dark-toned, low-angle fracture populations appear to postdate dark-red nodule formation and lithification and are in turn crosscut by the light-toned en-echelon fracture population (Fig. 8F; consistent with Meslin et al., 2022). The significant portion of randomly oriented light-toned fractures within the Carolyn Shoemaker formation that show no chemical difference to typical bedrock (e.g., Fig. 11) may indicate that some of these fractures remain unfilled, which in turn suggests that fracture propagation may have occurred at separate points in time and/or that not all fracture events may have resulted in precipitation of Ca-sulfate.

In the absence of petrographic observations, the timing of the Ca-sulfate cement proposed to exist in the Mirador formation cannot be determined unambiguously. However, Ca-enriched bedrock targets examined in this study lack evidence of crystal molds or bottom growth textures to support a surface primary evaporative origin for the Ca-sulfate. The simplest option is that this Ca-sulfate cement formed contemporaneous with the fluid event that filled the Ca-sulfate fractures, and the spatial distribution of Ca-sulfate cement was controlled by the porosity and permeability of the lithified strata. Similarly, the three nod-

ule populations that contain components of both Mg- and Ca-sulfate may have originally been more Mg-sulfate rich but were later replaced by Ca-sulfate during this same fluid event. This is supported by the higher solubility of Mg-sulfate compared to Ca-sulfate, by the multitonned textures in the light-toned nodule populations (i.e., white and light-gray polygons in Figs. 14A and 14C), and by the spread between Mg and Ca in the ternary diagram for the Ca- and Mg-bearing nodule populations (Fig. 11).

In summary, nearly all chemical and mineralogical evidence for water-rock interaction and alteration within the clay-sulfate transition region is or can be reasonably attributed to products of early and/or late diagenesis. Exceptions are the clay minerals in the Carolyn Shoemaker formation, for which we cannot unambiguously rule out a detrital origin, and possibly some component of X-ray amorphous alteration material, if it exists as detritus (and keeping in mind that some amorphous material may be detrital volcanic or impact glass). All other major indications of aqueous alteration are associated with possible early cements or late diagenetic nodules and mineralized veins. Mount Sharp, and Gale crater in general, records a diverse and long history of water-rock interaction in a complex lacustrine/fluvial/alluvial system on ancient Mars, but most of the alteration induced by water-rock interaction appears to have taken place after deposition and over a long period of time, which included cycles of burial and exhumation.

### Time Line of Aqueous Processes Recorded in the Clay-Sulfate Transition Region

Based on the data and interpretations presented above, and as diagrammed in Figure 16, we propose the following sequence of events associated with strata in the clay-sulfate transition region and along the Carolyn Shoemaker formation–Mirador formation contact:

- (1) Transport and deposition of Carolyn Shoemaker formation sediment. Sediment of the Carolyn Shoemaker formation is most consistent with aqueous deposition in a lacustrine/fluvial environment. The uppermost member of the Carolyn Shoemaker formation, Pontours, is extensively overprinted by diagenetic features, but rare hints of fine laminations suggest it may contain facies similar to the underlying Glasgow member. Elemental chemistry of the bulk sediment is consistent with underlying strata that indicate some degree of open-system chemical weathering. Limited chemical alteration of sediment may have taken place in the source region or during transport, perhaps under cold conditions, but cannot be uniquely determined with rover data.

(2) Lithification and early authigenic clay formation. Concurrent with or shortly after deposition, primary waters at or near the sediment-water interface or at shallow depth may have resulted in the precipitation of authigenic clay minerals in the Carolyn Shoemaker formation. This could also have included alteration of detrital clays, as suggested for lower portions of the Carolyn Shoemaker formation (e.g., Bristow et al., 2021; Thorpe et al., 2022). If present, such clays would act as a cement, and it is likely that at least some portions of the X-ray amorphous alteration components in the Carolyn Shoemaker formation are also present as cementing agents.

(3) Transition to an erosional regime. After an unknown amount of time, the lacustrine/fluvial/alluvial system recorded in Mount Sharp ceased or became very spatially limited, and the region transitioned to a net erosional state. This is evidenced by the presence of a regional unconformity that marks the upper boundary of the Carolyn Shoemaker formation along *Curiosity's* traverse. This unconformity spans up to ~11 m of stratigraphy (regionally) and has an estimated surface slope that is slightly steeper than the regional dip of the strata it separates. The amount of missing time that is represented by this unconformity is unknown, so the total duration of sustained aqueous activity at the surface of Gale crater and the exact nature of its cessation cannot be uniquely determined. To date, there is no clear indication of bedded evaporites or other diagnostic signs of salt precipitation resulting from evaporative concentration of a drying lake. Such indicators may have been eroded, be preserved elsewhere in the stratigraphy toward possible centers of paleolakes, or have been extremely minor or never present due to low solute concentrations in lake water and/or subsurface infiltration.

(4) Transition to an eolian depositional regime. At some point in time, Mount Sharp returned to a net depositional state, though under drier eolian conditions. Sediment of the eolian Mirador formation may include reworked components of the eroded Carolyn Shoemaker formation, which could explain the similarity in bulk elemental chemistry of the Carolyn Shoemaker formation and Mirador formation bedrock. However, clay minerals are conspicuously absent in the lower Mirador formation. The sediment was ultimately lithified, and X-ray amorphous components and Fe-oxides/oxyhydroxides are candidate cementing agents as revealed by CheMin XRD data. The transition to the lower eolian (Dunnideer, Port Logan) members of the Mirador formation in the clay-sulfate transition region does not imply or demonstrate a complete cessation of lacustrine or fluvial activity in the evolution of

Gale crater and Mount Sharp, particularly since higher stratigraphic positions show evidence for clay minerals (e.g., Sheppard et al., 2021) and fluvial activity (e.g., Caravaca et al., 2022b; Gupta et al., 2022).

(5) Late diagenetic interaction with (Fe + Mg)-rich fluids. After lithification of the lower Mirador formation, (Fe + Mg)-bearing fluids interacted with the rocks to create Fe-oxide/oxyhydroxides in dark-gray irregular nodules and Fe-oxide/oxyhydroxides and Mg-sulfate in the millimeter-scale lamination-enhancing nodules. The source of Mg may have been from fluids interacting with Mg-sulfate-bearing rocks in overlying Mount Sharp strata, or it could have been from dissolution of local bedrock (see discussion above). The origin of Fe is unclear, but it implies that Fe was somewhat mobile, and the lack of evidence for unusually low or high pH conditions suggests it was mobilized as Fe(II).

(6) Additional interaction with Mg-rich fluids. Mg-rich fluids reacted with bedrock to create the dark-red nodules that show strong stratigraphic dependence, i.e., at top of Carolyn Shoemaker formation and the bottom of the Mirador formation along the unconformity. This would also be consistent with top-down migration of brines and preferential concentration and precipitation of phases along the unconformity due to associated changes in hydraulic properties at this boundary.

(7) Interaction with (Na + Cl)-bearing fluid. This interaction created mineralized dark-toned fractures. This event, or at least its recorded signature, appears to have been quite localized based on the rare occurrence of these features at the base of the lower Mirador formation.

(8) Final interaction with (Ca + Mg + S)-bearing fluid. This phase formed Ca-sulfate in fractures and dissolved and replaced some of the lighter-toned Mg-sulfate nodules, resulting in the mixing line between Ca and Mg in the ternary diagram for nodule chemistry (Fig. 11). These fluids would presumably have become quickly saturated with respect to Mg-sulfate to avoid significant dissolution and disruption of bedding, which is not observed. The fluid event associated with Ca-sulfate mineralized fractures is also assumed to have been responsible for local Ca enrichment of bedrock, which is interpreted as local occurrences of Ca-sulfate cement.

#### COMPARISON TO PRELANDING ORBITAL FRAMEWORKS AND IMPLICATIONS FOR MAPPING IN SEDIMENTARY SUCCESSIONS ON MARS

Here, we discuss the degree to which geologic features and processes inferred from detailed

rover-scale observations align with the clay-to-sulfate spectroscopic signatures observed from orbit. Chemical and mineralogical detections of clay minerals are in overall good agreement with mapped orbital (CRISM) detections of clay minerals and associated spectral absorption band parameter maps for the studied portion of the Carolyn Shoemaker formation (Figs. 16A and 16B; Sheppard et al., 2021; Viviano, 2014). Both orbital and in situ clay mineral signatures begin to decline stratigraphically up section from Mont Mercou and toward the base of the Mirador formation (Fig. 17B; Sheppard et al., 2022). We suggest that this decline in orbital clay mineral abundance in proximity (but below) the Carolyn Shoemaker formation–Mirador formation boundary is caused by the increase in replacive diagenetic fabrics and nodules that overprint and dilute the primary, clay-bearing bedrock signatures in this area. Laboratory studies have demonstrated that clay-rich mixtures can obscure spectral signatures of hydrated sulfates (Sheppard et al., 2022), but it is equally likely that a field of view dominated by sulfate-bearing nodules may obscure evidence of clay minerals in the host rock.

Orbital detections of Mg-sulfate signatures become more prominent up section from Mont Mercou and are consistent with an increase in isolated occurrences of Mg-sulfate-bearing nodules (i.e., the dark-red disorganized nodule cluster population; Fig. 16B). Orbital detections continue to be present, but variable, through the lower section of the Mirador formation, where dark-red disorganized and organized nodule clusters are abundant. These nodules protrude from the surrounding bedrock and sometimes form lag deposits, both of which likely contribute to orbital signatures. Evidence for crystalline Mg-sulfate is absent in this region based on CheMin data, and Fe-sulfate, though observed previously (Rampe et al., 2017, 2020a), is also absent. However, amorphous content in drill samples doubles across the proposed basal Mirador formation unconformity (from 27% in Mary Anning to 54% in Maria Gordon), consistent with sulfate detections mapped from orbit (Fig. 17B). Our results strongly suggest that orbital detections of hydrated sulfate in this region correspond to diagenetic nodules enriched in amorphous Mg-sulfate. Orbital indicators of Mg-sulfate may be more prevalent in some sections of the clay-sulfate transition region because Mg-sulfate-rich diagenetic features (nodules) are more prevalent in those regions.

Though spatially congruent with the sedimentological transition from lacustrine to eolian depositional environments, the dominant association of Mg-sulfates with postdepositional diagenesis implies that the clay-to-sulfate mineral transition

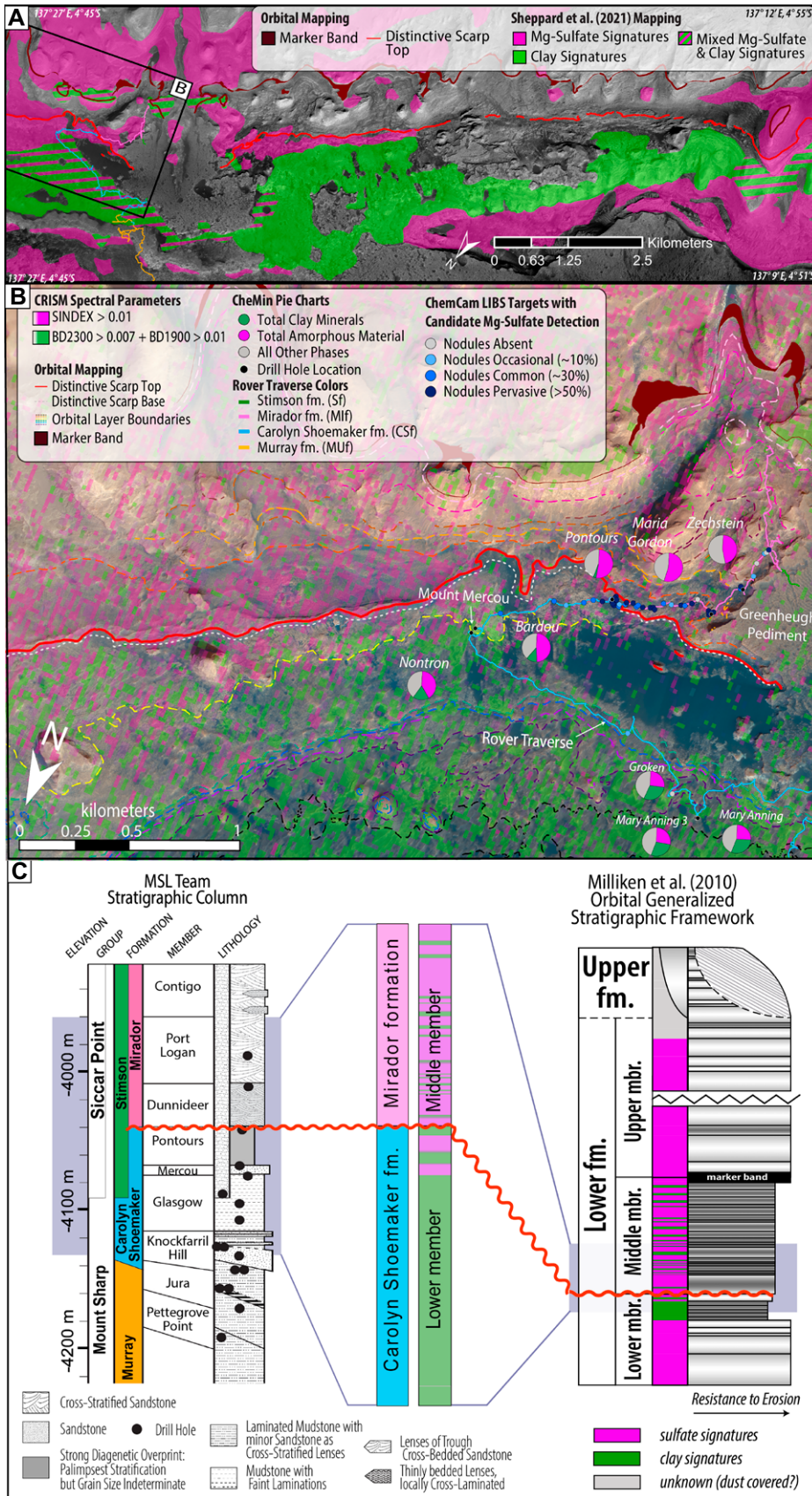


**Figure 17.** Comparison of study results to preexisting orbiter-based spectroscopic frameworks. (A) Regional study area showing position of distinctive scarp in relation to mapped detections of Mg-sulfate and clay as identified by Sheppard et al. (2011) in Compact Reconnaissance Imaging Spectrometer for Mars (CRISM) images. The regional transition from clay to sulfate-bearing spectroscopic signatures broadly aligns with (1) the location where *Curiosity* enters the Mirador formation and (2) the location of the distinctive scarp. (B) CRISM-derived spectral parameter maps over the clay-sulfate transition region of *Curiosity*'s traverse. Pink shading shows increased values of SINDEX (a spectral parameter that detects spectrum convexity related to hydrated sulfates; see Viviano et al., 2014). Green shading shows increased values of BD1900 (depth of the 1.9  $\mu\text{m}$   $\text{H}_2\text{O}$  absorption, sensitive to the presence of hydrated minerals; see Viviano et al., 2014) and BD2300 (depth of the 2.3  $\mu\text{m}$  absorption, sensitive to the presence of ferromagnesian clay minerals; see Viviano et al., 2014). Orbital spectroscopic detections of clay minerals (green mapped shading) occur most preferentially within the Carolyn Shoemaker formation and are in good agreement with CheMin drill sample total clay mineral abundance (green segments of pie charts). Orbital spectroscopic detections of sulfate minerals (pink mapped shading) are in good agreement with the pervasiveness of nodules across ChemCam laser-induced breakdown spectroscopy (LIBS) targets containing at least one candidate Mg-sulfate detection (i.e., elevated magnesium content beyond typical bedrock and depleted sum of oxide values). (C) Comparison of rover- and orbiter-based stratigraphic frameworks in the context of this study. Left stratigraphic column is the Mars Science Laboratory (MSL) Team stratigraphic column, with the purple-shaded background region showing the range of rover-traverse stratigraphy analyzed within this study. Right stratigraphic column is the preexisting orbital stratigraphic framework for Mount Sharp strata, adapted with permission from Milliken et al. (2010), with the purple-shaded background region showing the range of orbital stratigraphy analyzed in this study. The middle schematic column illustrates how this study—for the first time—connects these two frameworks. Our findings imply that the boundary between the Lower and Middle members of the Lower formation as defined from orbit by Milliken et al. (2010) is

(1) unconformable and (2) correlative to the boundary between the Carolyn Shoemaker and Mirador formations.

(Fig. 16A) is ultimately not fully contemporaneous with primary environmental signals. That is, conditions conducive to sulfate formation were not synchronous with the eolian deposition of the lower Mirador formation. Instead, later diagenesis preferentially concentrated sulfate within the Mirador formation and at the Carolyn Shoemaker formation–Mirador formation unconformity, and this coincides with the orbitally defined mineralogical transition.

The interpretation that the expression of a geomorphic scarp along the orbital layer boundary may be driven more by diagenetic nodule accumulation rather than primary stratification poses complications for orbital-scale stratigraphic investigations, particularly where in situ validation is not possible. Previous exploration by *Curiosity* of the geomorphic (but discontinuous) Vera Rubin ridge demonstrated the strong influence that diagenesis can have on local topography and morphology, especially when eolian abrasion is the dominant mechanism for denudation (Edgar et al., 2020; Fraeman et al., 2020). Similarly, Fedo et al. (2022) demonstrated that orbitally identified morphologic boundaries (e.g., those based on fracture abundance) in the clay-rich Glen Torridon region did not conform to clear facies changes or rover-based stratigraphic boundaries.

Both on Earth and Mars, understanding the nuanced connections between data sets collected at multiple scales of observation is crucial for determining regional stratigraphic relationships and identifying potential gaps in sedimentary rock records (Posamentier and Allen, 1999; Van Wagoner et al., 1990). This is especially true for low-angle unconformities, which can be challenging to identify unambiguously at the outcrop scale, even on Earth, where correlations can be walked out (Posamentier and Allen, 1999; e.g., Pipiringos and O'Sullivan, 1975, 1978; Kocurek and Dott, 1983; Swezey, 1991). Although outcrop data undoubtedly provide ground truth to remote data sets and are essential for providing detailed information to constrain depositional environments, they can also have limitations when it comes to identifying stratigraphic relationships over longer baselines (Posamentier and Allen, 1999; Van Wagoner et al., 1990). Conversely, coarser-resolution but more regionally extensive data sets (such as HiRISE images on Mars, or seismic or well-log data on Earth) may better capture stratigraphic architecture but provide less detailed information about depositional processes and any overprinting diagenesis (Posamentier and Allen, 1999; Van Wagoner et al., 1990). Not surprisingly, an integrated approach that combines the strengths and acknowledges the uncertainty of each type of data—orbital- and rover-based—is preferred to

fully understand the geological context of sedimentary strata on Mars.

## SUMMARY AND CONCLUSIONS

A key objective for the MSL *Curiosity* rover mission is to investigate the orbitally defined clay-sulfate transition in Mount Sharp strata and to assess whether it reflects a drying trend as previously hypothesized (Milliken et al., 2010; Rapin et al., 2021). We found that this mineral transition broadly coincides with the boundary between the Carolyn Shoemaker and Mirador formations. Although strongly overprinted by diagenesis, regional mapping suggests that this formation boundary is unconformable. The Carolyn Shoemaker formation records deposition in a lacustrine to marginal lacustrine environment, and the lower members (Dunnideer and Port Logan members) of the Mirador formation record a dry eolian environment. This up-section record of wetter (Carolyn Shoemaker formation) to drier (lower Mirador formation) depositional conditions is accompanied by distinct changes in diagenesis. Specifically, we suggest that syndepositional or early diagenetic clay mineral authigenic cements occur preferentially within the Carolyn Shoemaker formation. These cements and the lake waters from which they precipitated were likely absent during the dry deposition of the lower members of the lower Mirador formation. Sometime after lower Mirador formation deposition, these sediments were infiltrated by magnesium- and sulfate-rich fluids to form nodules bearing amorphous Mg-sulfate. Early clay cementation of the Carolyn Shoemaker formation may have created a hydraulic barrier such that these fluids accumulated preferentially within the lower Mirador formation. The proposed basal Mirador formation unconformity may have also acted as a fluid conduit to further promote enhanced accumulation of Mg-sulfate nodules in this region. These erosion-resistant, dark-toned nodules may contribute to the color and slope changes observed along this boundary from orbit. Overall, our findings confirm the co-occurrence of the clay-sulfate transition with the drying of depositional environments. However, our findings also highlight that complex interactions among primary depositional environment, erosion, and postdepositional diagenesis likely also influence orbital signatures in this mineral transition.

## ACKNOWLEDGMENTS

We gratefully acknowledge the National Aeronautics and Space Administration (NASA) Mars Science Laboratory (MSL) mission and the efforts of the MSL engineering and science operations teams for making this study possible. We are grateful to Malin Space Science Systems for providing all Mastcam mosa-

ics analyzed and presented in this study. Part of this research was supported by the Future Investigators in NASA Earth and Space Science and Technology (FINESST) program (80NSSC20K1375). Part of this research was carried out at the Jet Propulsion Laboratory, California Institute of Technology, under a contract with NASA (80NM0018D0004). G. Caravaca, O. Gasnault, and S. Le Mouélic work on ChemCam, and *Curiosity* is supported by the Centre National d'Etudes Spatiales (CNES). Raw data products supporting the conclusions of this work can be obtained from the NASA Planetary Data System (PDS). Any use of trade, firm, or product names is for descriptive purposes only and does not imply endorsement by the U.S. government.

## REFERENCES CITED

- Ajdkiewicz, J.M., and Larese, R.E., 2012, How clay grain coats inhibit quartz cement and preserve porosity in deeply buried sandstones: Observations and experiments: *American Association of Petroleum Geologists Bulletin*, v. 96, no. 11, p. 2091–2119, <https://doi.org/10.1306/02211211075>.
- Al-Ramadan, K., 2021, The role of diagenesis at unconformities of the Paleozoic siliciclastic succession of central Saudi Arabia: Implications for reservoir quality: *Arabian Journal of Geosciences*, v. 14, no. 6, p. 1–12, <https://doi.org/10.1007/s12517-021-06845-6>.
- Anderson, D.E., et al., 2017, Characterization of LIBS emission lines for the identification of chlorides, carbonates, and sulfates in salt/basalt mixtures for the application to MSL ChemCam data: *Journal of Geophysical Research: Planets*, v. 122, no. 4, p. 744–770, <https://doi.org/10.1002/2016JE005164>.
- Anderson, R., and Bell, J.F., 2010, Geologic mapping and characterization of Gale crater and implications for its potential as a Mars Science Laboratory landing site: *MARS—The International Journal of Mars Science and Exploration*, v. 5, p. 76–128, <https://doi.org/10.1555/mars.2010.0004>.
- Banham, S.G., Gupta, S., Rubin, D.M., Edgett, K.S., Barnes, R., Van Beek, J., Watkins, J.A., Edgar, L.A., Fedo, C.M., Williams, R.M., and Stack, K.M., 2021, A rock record of complex aeolian bedforms in a Hesperian desert landscape: The Stimson formation as exposed in the Murray buttes, Gale crater, Mars: *Journal of Geophysical Research: Planets*, v. 126, no. 4, <https://doi.org/10.1029/2020JE006554>.
- Bennett, K.A., Fox, V.K., Bryk, A., Dietrich, W., Fedo, C., Edgar, L., Thorpe, M.T., Williams, A.J., Wong, G.M., Dehouck, E., and McAdam, A., 2023, The *Curiosity* rover's exploration of Glen Torridon, Gale crater, Mars: An overview of the campaign and scientific results: *Journal of Geophysical Research: Planets*, v. 128, no. 1, <https://doi.org/10.1029/2022JE007185>.
- Berger, J.A., Gellert, R., Boyd, N.I., King, P.L., McCraig, M.A., O'Connell-Cooper, C.D., Schmidt, M.E., Spray, J.G., Thompson, L.M., VanBommel, S.J., and Yen, A.S., 2020, Elemental composition and chemical evolution of geologic materials in Gale crater, Mars: APXS results from Bradbury landing to the Vera Rubin ridge: *Journal of Geophysical Research: Planets*, v. 125, no. 12, <https://doi.org/10.1029/2020JE006536>.
- Berger, J.A., Gellert, R., McCraig, M.A., O'Connell-Cooper, C.D., Thompson, L.M., VanBommel, S.J.V., and Yen, A.S., 2022, Uniform Mount Sharp bedrock composition and minor Mg-sulfate in nodules: APXS results from the clay-sulfate transition in Gale crater, Mars, in *53rd Lunar and Planetary Science Conference: Lunar and Planetary Institute Contribution 2678*, abstract 2764, <https://www.hou.usra.edu/meetings/lpsc2022/pdf/2764.pdf>.
- Berger, J.A., Gellert, R., McCraig, M.A., O'Connell-Cooper, C.D., Spray, J.G., Thompson, L.M., VanBommel, S.J., Yen, A.S., Rampe, E.B., and Clark, J.V., 2023, Isochemical characteristics of the clay-sulfate transition in Gale crater, Mars: APXS results from Mont Mercou to the marker band valley: *Lunar and Planetary Institute Contribution 2806*, no. 1662, <https://ntrs.nasa.gov>

- .gov/api/citations/20230000120/downloads/Berger\_LPSC\_2023-v4.pdf.
- Bibring, J.P., et al., 2006, Global mineralogical and aqueous Mars history derived from *OMEGA/Mars Express* data: *Science*, v. 312, no. 5772, p. 400–404, <https://doi.org/10.1126/science.1122659>.
- Blake, D., Vaniman, D., Achilles, C., Anderson, R., Bish, D., Bristow, T., Chen, C., Chipera, S., Crisp, J., Des Marais, D., and Downs, R.T., 2012, Characterization and calibration of the CheMin mineralogical instrument on Mars Science Laboratory: *Space Science Reviews*, v. 170, p. 341–399, <https://doi.org/10.1007/s11214-012-9905-1>.
- Bristow, T.F., Rampe, E.B., Achilles, C.N., Blake, D.F., Chipera, S.J., Craig, P., Crisp, J.A., Des Marais, D.J., Downs, R.T., Gellert, R., and Grotzinger, J.P., 2018, Clay mineral diversity and abundance in sedimentary rocks of Gale crater, Mars: *Science Advances*, v. 4, no. 6, <https://doi.org/10.1126/sciadv.aar3330>.
- Bristow, T.F., Rampe, E.B., Grotzinger, J.P., Fox, V.K., Bennett, K.A., Yen, A.S., Vasavada, A.R., Vaniman, D.T., Tu, V., Treiman, A.H., and Thorpe, M.T., 2019, Clay minerals of Glen Torridon, Mount Sharp, Gale crater, Mars, in 9th International Conference on Mars, July 22–25, 2019, Pasadena, California: Lunar and Planetary Institute Contribution 2089, abstract 6390, <https://www.hou.usra.edu/meetings/ninthmars2019/pdf/6390.pdf>.
- Bristow, T.F., Grotzinger, J.P., Rampe, E.B., Cuadros, J., Chipera, S.J., Downs, G.W., Fedo, C.M., Frydenvang, J., McAdam, A.C., Morris, R.V., and Achilles, C.N., 2021, Brine-driven destruction of clay minerals in Gale crater, Mars: *Science*, v. 373, no. 6551, p. 198–204, <https://doi.org/10.1126/science.abc5449>.
- Bryk, A.B., Dietrich, W.E., Lamb, M.P., Grotzinger, J.P., Vasavada, A.R., Stack, K.M., Arvidson, R., Fedo, C., Bennett, K., Fox, V.K., and Gupta, S., 2019, In *Curiosity's* path: The geomorphology and stratigraphy of the Greenhugh Pediment and Gediz Vallis ridge in Gale crater, in 50th Annual Lunar and Planetary Science Conference: Lunar and Planetary Institute Contribution 2132, abstract 2263, <https://www.hou.usra.edu/meetings/lpsc2019/pdf/2263.pdf>.
- Buz, J., Ehlmann, B.L., Pan, L., and Grotzinger, J.P., 2017, Mineralogy and stratigraphy of the Gale crater rim, wall, and floor units: *Journal of Geophysical Research: Planets*, v. 122, p. 1090–1118, <https://doi.org/10.1002/2016JE005163>.
- Calef, F.J., III, and Parker, T., 2016, MSL Gale Merged Orthophoto Mosaic: Reston, Virginia, PDS Annex, U.S. Geological Survey, [http://bit.ly/MSL\\_Basemap](http://bit.ly/MSL_Basemap).
- Caravaca, G., et al., 2022a, From lake to river: Documenting an environmental transition across the Jura/Knockfaril Hill members boundary in the Glen Torridon region of Gale crater (Mars): *Journal of Geophysical Research: Planets*, v. 127, no. 9, <https://doi.org/10.1029/2021JE007093>.
- Caravaca, G., Le Mouélic, S., Gupta, S., Mangold, N., Rapin, W., Schieber, J., Le Deit, L., Gasnault, O., and Lanza, N.L., 2022b, The Prow outcrop: An “open catalog” of multiscale 3D fluvial sedimentary structures in the lower sulfate unit of Gale crater (Mars): *European Science Congress Abstracts*, v. 16, <https://doi.org/10.5194/epsc2022-336>.
- Cardenas, B.T., Grotzinger, J.P., Lamb, M.P., Lewis, K., Fedo, C., Bryk, A., Dietrich, W., Stein, N., Turner, M., and Caravaca, G., 2022, Barform deposits of the Carolyn Shoemaker formation, Gale crater, Mars: *Journal of Sedimentary Research*, v. 92, no. 12, p. 1071–1092, <https://doi.org/10.2110/jfsr.2022.032>.
- Carr, M.H., and Head, J.W., III, 2010, Geologic history of Mars: *Earth and Planetary Science Letters*, v. 294, no. 3–4, p. 185–203, <https://doi.org/10.1016/j.epsl.2009.06.042>.
- Carter, J., Riu, L., Poulet, F., Bibring, J.P., Langevin, Y., and Gondet, B., 2023, A Mars orbital catalog of aqueous alteration signatures (MOCAAS): *Icarus*, v. 389, <https://doi.org/10.1016/j.icarus.2022.115164>.
- Caswell, T.E., and Milliken, R.E., 2017, Evidence for hydraulic fracturing at Gale crater, Mars: Implications for burial depth of the Yellowknife Bay formation: *Earth and Planetary Science Letters*, v. 468, p. 72–84, <https://doi.org/10.1016/j.epsl.2017.03.033>.
- Chipera, S.J., and Bish, D.L., 2013, Fitting full X-ray diffraction patterns for quantitative analysis: A method for readily quantifying crystalline and disordered phases: *Advances in Materials Physics and Chemistry*, v. 3, no. 1A, p. 47–53, <https://doi.org/10.4236/ampc.2013.31A007>.
- Chipera, S.J., and Vaniman, D.T., 2007, Experimental stability of magnesium sulfate hydrates that may be present on Mars: *Geochimica et Cosmochimica Acta*, v. 71, no. 1, p. 241–250, <https://doi.org/10.1016/j.gca.2006.07.044>.
- Chipera, S.J., et al., 2023, Mineralogical investigation of Mg-sulfate at the Canaima drill site, Gale crater, Mars: *Journal of Geophysical Research: Planets*, v. 128, no. 11, <https://doi.org/10.1029/2023JE008041>.
- Cino, C.D., Dehouck, E., and McLennan, S.M., 2017, Geochemical constraints on the presence of clay minerals in the Burns formation, Meridiani Planum, Mars: *Icarus*, v. 281, p. 137–150, <https://doi.org/10.1016/j.icarus.2016.08.029>.
- Clark, J.V., Sutter, B., Wong, G., Lewis, J., McAdam, A.C., Archer, P.D., Mahaffy, P., Franz, H., Eigenbrode, J., Freissinet, C., and Stern, J., 2022, Sample analysis at Mars—Evolved Gas analysis (SAM-EGA) results from the clay-sulfate transition region in Gale crater, Mars, in 53rd Lunar and Planetary Science Conference: Lunar and Planetary Institute Contribution 2678, abstract 1160, <https://insu.hal.science/insu-04507816>.
- Das, D., et al., 2020, Boron and lithium in calcium sulfate veins: Tracking precipitation of diagenetic materials in Vera Rubin ridge, Gale crater: *Journal of Geophysical Research: Planets*, v. 125, no. 8, <https://doi.org/10.1029/2019JE006301>.
- David, G., Cousin, A., Forni, O., Meslin, P.Y., Dehouck, E., Mangold, N., L'Haridon, J., Rapin, W., Gasnault, O., Johnson, J.R., and Ollila, A.M., 2020, Analyses of high-iron sedimentary bedrock and diagenetic features observed with ChemCam at Vera Rubin ridge, Gale crater, Mars: Calibration and characterization: *Journal of Geophysical Research: Planets*, v. 125, no. 10, <https://doi.org/10.1029/2019JE006314>.
- Day, M., and Kocurek, G., 2016, Observations of an aeolian landscape: From surface to orbit in Gale crater: *Icarus*, v. 280, p. 37–71, <https://doi.org/10.1016/j.icarus.2015.09.042>.
- Dehouck, E., McLennan, S.M., Meslin, P.Y., Cousin, A., Rampe, E.B., Morris, R.V., Lanza, N.L., Hurowitz, J.A., Rapin, W., and MSL Science Team, 2014, Constraints on abundances and compositional ranges of X-ray amorphous components in soils and rocks at Gale crater from mass balance calculations, in 8th International Conference on Mars, July 14–18, 2014, Pasadena, California: Lunar and Planetary Institute Contribution 1791, abstract 1224, <https://www.hou.usra.edu/meetings/8thmars2014/pdf/1224.pdf>.
- Dehouck, E., et al., 2022, Bedrock geochemistry and alteration history of the clay-bearing Glen Torridon region of Gale crater, Mars: *Journal of Geophysical Research: Planets*, v. 127, no. 12, <https://doi.org/10.1029/2021JE007103>.
- Dickson, J.L., Kerber, L.A., Fassett, C.I., and Ehlmann, B.L., 2018, A global, blended CTX mosaic of Mars with vectorized seam mapping: A new mosaicking pipeline using principles of non-destructive image editing, in 49th Lunar and Planetary Science Conference: Lunar and Planetary Institute Contribution 2083, abstract 2480, <https://www.hou.usra.edu/meetings/lpsc2018/pdf/2480.pdf>.
- Dolson, J.C., Shanley, K.W., Hendricks, M.L., and Wescott, W.A., 1994, A review of fundamental concepts of hydrocarbon exploration in unconformity related traps, in Dolson, J.C., Hendricks, M.L., and Wescott, W.A., eds., *Unconformity-Related Hydrocarbons in Sedimentary Sequences*: Denver, Colorado, Rocky Mountain Association of Geologists Guidebook, p. 1–22.
- Edgar, L.A., et al., 2020, A lacustrine paleoenvironment recorded at Vera Rubin ridge, Gale crater: Overview of the sedimentology and stratigraphy observed by the Mars Science Laboratory *Curiosity* rover: *Journal of Geophysical Research: Planets*, v. 125, no. 3, <https://doi.org/10.1029/2019JE006307>.
- Edgett, K.S., Caplinger, M.A., Maki, J.N., Ravine, M.A., Ghaemi, F.T., McNair, S., Herkenhoff, K.E., Duston, B.M., Willson, R.G., Yingst, R.A., and Kennedy, M.R., 2015, *Curiosity's* Robotic Arm—Mounted Mars Hand Lens Imager (MAHLI): Characterization and Calibration Status: MSL MAHLI Technical Report 0001, 102 p., <https://doi.org/10.13140/RG.2.1.3798.5447>.
- Ehlmann, B.L., Mustard, J.F., Murchie, S.L., Bibring, J.P., Meunier, A., Fraeman, A.A., and Langevin, Y., 2011, Subsurface water and clay mineral formation during the early history of Mars: *Nature*, v. 479, no. 7371, p. 53–60, <https://doi.org/10.1038/nature10582>.
- Ehlmann, B.L., Berger, G., Mangold, N., Michalski, J.R., Catling, D.C., Ruff, S.W., et al., 2013, Geochemical consequences of widespread clay mineral formation in Mars' ancient crust: *Space Science Reviews*, v. 174, p. 329–364, <https://doi.org/10.1007/s11214-012-9930-0>.
- Fedo, C.M., et al., 2022, Geology and stratigraphic correlation of the Murray and Carolyn Shoemaker formations: *Journal of Geophysical Research: Planets*, v. 127, no. 9, <https://doi.org/10.1029/2022JE007408>.
- Flahaut, J., Massé, M., Le Deit, L., Tholot, P., Bibring, J.P., Poulet, F., Quantin, C., Mangold, N., Michalski, J., and Bishop, J.L., 2014, Sulfate-rich deposits on Mars: A review of their occurrences and geochemical implications, in 8th International Conference on Mars, July 14–18, 2014, Pasadena, California: Lunar and Planetary Institute Contribution 1791, abstract 1196, <https://www.hou.usra.edu/meetings/8thmars2014/pdf/1196.pdf>.
- Forni, O., Meslin, P.Y., L'Haridon, J., Rapin, W., Nachon, M., Newsom, H., Mangold, N., Gasnault, O., Anderson, D.E., Anderson, R.B., and Blaney, D.L., 2017, Detection of fluorine-rich phases, phosphates, and halite in the Stimson-Murray units, Gale crater, Mars, in 48th Annual Lunar and Planetary Science Conference: Lunar and Planetary Institute Contribution 1964, abstract 1838, <https://www.hou.usra.edu/meetings/lpsc2017/pdf/1838.pdf>.
- Fraeman, A.A., Ehlmann, B.L., Arvidson, R.E., Edwards, C.S., Grotzinger, J.P., Milliken, R.E., Quinn, D.P., and Rice, M.S., 2016, The stratigraphy and evolution of lower Mount Sharp from spectral, morphological, and thermophysical orbital data sets: *Journal of Geophysical Research: Planets*, v. 121, no. 9, p. 1713–1736, <https://doi.org/10.1002/2016JE005095>.
- Fraeman, A.A., Edgar, L.A., Rampe, E.B., Thompson, L.M., Frydenvang, J., Fedo, C.M., Catalano, J.G., Dietrich, W.E., Gabriel, T.S., Vasavada, A.R., and Grotzinger, J.P., 2020, Evidence for a diagenetic origin of Vera Rubin ridge, Gale crater, Mars: Summary and synthesis of *Curiosity's* exploration campaign: *Journal of Geophysical Research: Planets*, v. 125, no. 12, <https://doi.org/10.1029/2020JE006527>.
- Frydenvang, J., Mangold, N., Wiens, R.C., Fraeman, A.A., Edgar, L.A., Fedo, C.M., L'Haridon, J., Bedford, C.C., Gupta, S., Grotzinger, J.P., and Bridges, J.C., 2020, The chemostratigraphy of the Murray formation and role of diagenesis at Vera Rubin ridge in Gale crater, Mars, as observed by the ChemCam instrument: *Journal of Geophysical Research: Planets*, v. 125, no. 9, <https://doi.org/10.1029/2019JE006320>.
- Gasda, P.J., Comellas, J., Essunfeld, A., Das, D., Bryk, A.B., Dehouck, E., Schwener, S.P., Crossey, L., Herkenhoff, K., Johnson, J.R., and Newsom, H., 2022, Overview of the morphology and chemistry of diagenetic features in the clay-rich Glen Torridon unit of Gale crater, Mars: *Journal of Geophysical Research: Planets*, v. 127, no. 12, <https://doi.org/10.1029/2021JE007097>.
- Goetz, W., Bruns, M., Thoma, S., Pardowitz, I., and Stein, T.C., 2023, Determination of spatial scale in Martian landscape images acquired by the *Curiosity* rover, and viewing image scale and target chemistry using the ASIC website: *Earth and Space Science*, v. 10, no. 5, <https://doi.org/10.1029/2020EA001611>.
- Goudge, T.A., Mustard, J.F., Head, J.W., Fassett, C.I., and Wiseman, S.M., 2015, Assessing the mineralogy of the watershed and fan deposits of the Jezero crater paleolake system, Mars: *Journal of Geophysical Research: Planets*, v. 120, no. 4, p. 775–808, <https://doi.org/10.1002/2014JE004782>.
- Grotzinger, J.P., et al., 2014, A habitable fluvio-lacustrine environment at Yellowknife Bay, Gale crater, Mars: *Science*, v. 343, no. 6169, <https://doi.org/10.1126/science.1242777>.
- Grotzinger, J.P., Gupta, S., Malin, M.C., Rubin, D.M., Schieber, J., Siebach, K., et al., 2015, Deposition, ex-

- humation, and paleoclimate of an ancient lake deposit, Gale crater, Mars: *Science*, v. 350, no. 6257, <https://doi.org/10.1126/science.aac7575>.
- Gupta, S., Edgar, L., Yingst, R.A., Bryk, A., Caravaca, G., Dietrich, W., Grotzinger, J., Rubin, D., Rapin, W., Banham, S., and Roberts, A., 2022, Episodic aqueous conditions punctuated dominantly aeolian deposition within the layered sulphate-bearing unit, Gale crater (Mars): *Europlanet Science Congress Abstracts*, v. 16, <https://doi.org/10.5194/epsc2022-963>.
- Gwizd, S., Fedo, C., Grotzinger, J., Banham, S., Rivera-Hernandez, F., Stack, K.M., Siebach, K., Thorpe, M., Thompson, L., O'Connell-Cooper, C., and Stein, N., 2022, Sedimentological and geochemical perspectives on a marginal lake environment recorded in the Hartmann's Valley and Karasburg members of the Murray formation, Gale crater, Mars: *Journal of Geophysical Research: Planets*, v. 127, no. 8, <https://doi.org/10.1029/2022JE007280>.
- Hughes, C.M., Rice, M.S., Barnhart, C.J., Swanson, T.E., Pfeiffer, A.M., and Goudge, T.A., 2023, Sources of clay-rich sediment in Eberswalde crater, Mars, with implications for biopreservation potential: *Journal of Geophysical Research: Planets*, v. 128, no. 4, <https://doi.org/10.1029/2022JE007545>.
- Huntoon, J.E., Dubiel, R.F., and Stanesco, J.D., 1994, Tectonic influence on development of the Permian-Triassic unconformity and basal Triassic strata, Paradox Basin, southeastern Utah, *in* Caputo, M.V., Peterson, J.A., and Franczyk, K.J., eds., *Mesozoic Systems of the Rocky Mountain Region, USA*: Denver, Colorado, Rocky Mountain Section, Society for Sedimentary Geology (SEPM), p. 109–132.
- Hurowitz, J.A., Grotzinger, J.P., Fischer, W.W., McLennan, S.M., Milliken, R.E., Stein, N., Vasavada, A.R., Blake, D.F., Dehouck, E., Eigenbrode, J.L., and Fairen, A.G., 2017, Redox stratification of an ancient lake in Gale crater, Mars: *Science*, v. 356, no. 6341, <https://doi.org/10.1126/science.aah6849>.
- Kite, E.S., Sneed, J., Mayer, D.P., Lewis, K.W., Michaels, T.I., Hore, A., and Raffkin, S.C., 2016, Evolution of major sedimentary mounds on Mars: Buildup via anticompensational stacking modulated by climate change: *Journal of Geophysical Research: Planets*, v. 121, no. 11, p. 2282–2324, <https://doi.org/10.1002/2016JE005135>.
- Kocurek, G., and Dott, R.H., Jr., 1983, Jurassic paleogeography and paleoclimate of the central and southern Rocky Mountains region, *in* Reynolds, M.W., and Dolly, E.D., eds., *Mesozoic Paleogeography of the West-Central United States: Rocky Mountain Symposium 2*: Denver, Colorado, Rocky Mountain Section, Society for Sedimentary Geology (SEPM), p. 101–116.
- Kronyak, R.E., Kah, L.C., Edgett, K.S., VanBommel, S.J., Thompson, L.M., Wiens, R.C., Sun, V.Z., and Nachon, M., 2019, Mineral-filled fractures as indicators of multigenerational fluid flow in the Pahrump Hills member of the Murray formation, Gale crater, Mars: *Earth and Space Science* (Hoboken, N.J.), v. 6, no. 2, p. 238–265, <https://doi.org/10.1029/2018EA000482>.
- Langevin, Y., Gondet, B., Gasnault, O., Herkenhoff, K., Blaney, D., Maurice, S., Wiens, R., and MSL Science Team, 2013, Processing approaches for optimal science exploitation of the ChemCam remote microscopic imager (RMI) on-board *Curiosity*: *Geophysical Research Abstracts*, v. 15, abstract EGU2013-9277, <https://meetingorganizer.copernicus.org/EGU2013/EGU2013-9277.pdf>.
- Le Deit, L., Hauber, E., Fueten, F., Pondrelli, M., Rossi, A.P., and Jaumann, R., 2013, Sequence of infilling events in Gale crater, Mars: Results from morphology, stratigraphy, and mineralogy: *Journal of Geophysical Research: Planets*, v. 118, no. 12, p. 2439–2473, <https://doi.org/10.1002/2012JE004322>.
- Le Mouélic, S., et al., 2015, The ChemCam remote microscopic imager at Gale crater: Review of the first year of operations on Mars: *Icarus*, v. 249, p. 93–107, <https://doi.org/10.1016/j.icarus.2014.05.030>.
- L'Haridon, J., Mangold, N., Meslin, P.Y., Johnson, J.R., Rapin, W., Forni, O., Cousin, A., Payré, V., Dehouck, E., Nachon, M., and Le Deit, L., 2018, Chemical variability in mineralized veins observed by ChemCam on the lower slopes of Mount Sharp in Gale crater, Mars: *Icarus*, v. 311, p. 69–86, <https://doi.org/10.1016/j.icarus.2018.01.028>.
- L'Haridon, J., Mangold, N., Fraeman, A.A., Johnson, J.R., Cousin, A., Rapin, W., David, G., Dehouck, E., Sun, V., Frydenvang, J., and Gasnault, O., 2020, Iron mobility during diagenesis at Vera Rubin ridge, Gale crater, Mars: *Journal of Geophysical Research: Planets*, v. 125, no. 11, <https://doi.org/10.1029/2019JE006299>.
- Malin, M.C., et al., 2017, The Mars Science Laboratory (MSL) Mast cameras and Descent imager: Investigation and instrument descriptions: *Earth and Space Science*, v. 4, no. 8, p. 506–539, <https://doi.org/10.1002/2016EA000252>.
- Mangold, N., Schmidt, M.E., Fisk, M.R., Forni, O., McLennan, S.M., Ming, D.W., Sautter, V., Sumner, D., Williams, A.J., Clegg, S.M., and Cousin, A., 2017, Classification scheme for sedimentary and igneous rocks in Gale crater, Mars: *Icarus*, v. 284, p. 1–17, <https://doi.org/10.1016/j.icarus.2016.11.004>.
- Mangold, N., et al., 2019, Chemical alteration of fine-grained sedimentary rocks at Gale crater: *Icarus*, v. 321, p. 619–631, <https://doi.org/10.1016/j.icarus.2018.11.004>.
- Martin, P.E., et al., 2017, A two-step K-Ar experiment on Mars: Dating the diagenetic formation of jarosite from Amazonian groundwaters: *Journal of Geophysical Research: Planets*, v. 122, no. 12, p. 2803–2818, <https://doi.org/10.1002/2017JE005445>.
- Maurice, S., Wiens, R.C., Saccoccio, M., Barraclough, B., Gasnault, O., Forni, O., Mangold, N., Baratoux, D., Bender, S., Berger, G., and Bernardin, J., 2012, The ChemCam instrument suite on the Mars Science Laboratory (MSL) rover: Science objectives and mast unit description: *Space Science Reviews*, v. 170, p. 95–166, <https://doi.org/10.1007/s11214-012-9912-2>.
- McLennan, S.M., Anderson, R.B., Bell, J.F., III, Bridges, J.C., Calef, F., III, Campbell, J.L., Clark, B.C., Clegg, S., Conrad, P., Cousin, A., and Des Marais, D.J., 2014, Elemental geochemistry of sedimentary rocks at Yellowknife Bay, Gale crater, Mars: *Science*, v. 343, no. 6169, <https://doi.org/10.1126/science.1244734>.
- Meslin, P.Y., Rapin, W., Forni, O., Cousin, A., Gasnault, O., Loche, M., Dehouck, E., Mangold, N., Caravaca, G., Schröder, S., and Gasda, P., 2022, Significant halite enrichment in the sulfate-unit of Gale crater, Mars, *in* 53rd Lunar and Planetary Science Conference: Lunar and Planetary Institute Contribution 2678, abstract 2492, <https://www.hou.usra.edu/meetings/lpsc2022/pdf/2492.pdf>.
- Meyer, M.J., Milliken, R.E., Hurowitz, J.E., and Robertson, K.M., 2023, Ancient siliciclastic-evaporites as seen by remote sensing instrumentation with implications for the rover-scale exploration of sedimentary environments on Mars: *Astrobiology*, v. 23, no. 5, p. 477–495, <https://doi.org/10.1089/ast.2022.0103>.
- Milliken, R.E., and Bish, D.L., 2011, Clays beyond Earth: Clays and Clay Minerals, v. 59, p. 337–338, <https://doi.org/10.1346/CCMN.2011.0590400>.
- Milliken, R.E., Grotzinger, J.P., and Thomson, B.J., 2010, Paleoclimate of Mars as captured by the stratigraphic record in Gale crater: *Geophysical Research Letters*, v. 37, no. 4, L04201, <https://doi.org/10.1029/2009GL041870>.
- Nachon, M., Clegg, S.M., Mangold, N., Schröder, S., Kah, L.C., Dromart, G., Ollila, A., Johnson, J.R., Oehler, D.Z., Bridges, J.C., and Le Mouélic, S., 2014, Calcium sulfate veins characterized by ChemCam/*Curiosity* at Gale crater, Mars: *Journal of Geophysical Research: Planets*, v. 119, no. 9, p. 1991–2016, <https://doi.org/10.1002/2013JE004588>.
- North American Commission on Stratigraphic Nomenclature, 2005, North American Stratigraphic Code: American Association of Petroleum Geologists Bulletin, v. 89, no. 11, p. 1547–1591, <https://doi.org/10.1306/07050504129>.
- Okubo, C.H., 2014, Bedrock Geologic and Structural Map Through the Western Candor Colles Region of Mars: U.S. Geological Survey Scientific Investigations Map 3309, scale 1:18,000, <https://doi.org/10.3133/sim3309>.
- Okubo, C.H., and Gaither, T.A., 2017, Bedrock and Structural Geologic Maps of Eastern Candor Sulci, Western Ceti Mensa, and Southeastern Ceti Mensa, Candor Chasma, Valles Marineris Region of Mars: U.S. Geological Survey Scientific Investigations Map 3359, scale 1:18,000, <https://doi.org/10.3133/sim3359>.
- Pipiringos, G.N., and O'Sullivan, R.B., 1975, Chert pebble unconformity at the top of the Navajo Sandstone in southeastern Utah, *in* Fassett, J.E., ed., *Canyonlands: Country, Eighth Field Conference*: Durango, Colorado, Four Corners Geological Society, p. 149–156.
- Pipiringos, G.N., and O'Sullivan, R.B., 1978, Principal unconformities in Triassic and Jurassic rocks, western interior United States—A preliminary survey: U.S. Geological Survey Professional Paper 1035-A, 29 p., <https://doi.org/10.3133/pp1035A>.
- Posamentier, H.W., and Allen, G.P., eds., 1999, *Siliciclastic Sequence Stratigraphy—Concepts and Applications*: Society for Sedimentary Geology (SEPM) Concepts in Sedimentology and Paleontology 7, 210 p., <https://doi.org/10.2110/csp.99.07>.
- Rampe, E.B., et al., 2017, Mineralogy of an ancient lacustrine mudstone succession from the Murray formation, Gale crater, Mars: *Earth and Planetary Science Letters*, v. 471, p. 172–185, <https://doi.org/10.1016/j.epsl.2017.04.021>.
- Rampe, E.B., Bristow, T.F., Morris, R.V., Morrison, S.M., Achilles, C.N., Ming, D.W., Vaniman, D.T., Blake, D.F., Tu, V.M., Chipera, S.J., and Yen, A.S., 2020a, Mineralogy of Vera Rubin ridge from the Mars Science Laboratory CheMin instrument: *Journal of Geophysical Research: Planets*, v. 125, no. 9, <https://doi.org/10.1029/2019JE006306>.
- Rampe, E.B., Blake, D.F., Bristow, T.F., Ming, D.W., Vaniman, D.T., Morris, R.V., Achilles, C.N., Chipera, S.J., Morrison, S.M., Tu, V.M., and Yen, A.S., 2020b, Mineralogy and geochemistry of sedimentary rocks and eolian sediments in Gale crater, Mars: A review after six Earth years of exploration with *Curiosity*: *Geochemistry*, v. 80, no. 2, <https://doi.org/10.1016/j.chemer.2020.125605>.
- Rampe, E.B., et al., 2023, Mineralogical trends over the clay-sulfate transition in Gale crater from the Mars Science Laboratory CheMin Instrument, *in* 54th Lunar and Planetary Science Conference: Lunar and Planetary Institute Contribution 2806, abstract 1554, <https://www.hou.usra.edu/meetings/lpsc2023/pdf/1554.pdf>.
- Rapin, W., Meslin, P.Y., Maurice, S., Vaniman, D., Nachon, M., Mangold, N., Schröder, S., Gasnault, O., Forni, O., Wiens, R.C., and Martínez, G.M., 2016, Hydration state of calcium sulfates in Gale crater, Mars: Identification of bassanite veins: *Earth and Planetary Science Letters*, v. 452, p. 197–205, <https://doi.org/10.1016/j.epsl.2016.07.045>.
- Rapin, W., Ehlmann, B.L., Dromart, G., Schieber, J., Thomas, N.H., Fischer, W.W., Fox, V.K., Stein, N.T., Nachon, M., Clark, B.C., and Kah, L.C., 2019, An interval of high salinity in ancient Gale crater lake on Mars: *Nature Geoscience*, v. 12, no. 11, p. 889–895, <https://doi.org/10.1038/s41561-019-0458-8>.
- Rapin, W., Dromart, G., Rubin, D., Le Deit, L., Mangold, N., Edgar, L.A., Gasnault, O., Herkenhoff, K., Le Mouélic, S., Anderson, R.B., and Maurice, S., 2021, Alternating wet and dry depositional environments recorded in the stratigraphy of Mount Sharp at Gale crater: *Geology*, v. 49, p. 842–846, <https://doi.org/10.1130/G48519.1>.
- Rapin, W., Sheppard, R., Dromart, G., Schieber, J., Clark, B., Kah, L., Rubin, D., Ehlmann, B., Gupta, S., Caravaca, G., and Mangold, N., 2022, The *Curiosity* rover is exploring a key sulfate-bearing orbital facies, *in* 53rd Lunar and Planetary Science Conference: Lunar and Planetary Institute Contribution 2678, abstract 2473, <https://www.hou.usra.edu/meetings/lpsc2022/pdf/2473.pdf>.
- Rapin, W., et al., 2023, Sustained wet-dry cycling on early Mars: *Nature*, v. 620, p. 299–302, <https://doi.org/10.1038/s41586-023-06220-3>.
- Rivera-Hernández, F., et al., 2020, Grain size variations in the Murray formation: Stratigraphic evidence for changing depositional environments in Gale crater, Mars: *Journal of Geophysical Research: Planets*, v. 125, no. 2, <https://doi.org/10.1029/2019JE006230>.
- Seeger, C.H., Grotzinger, J.P., and Cowart, A.C., 2023, Diagenetic overprints associated with the clay-sulfate transition in Gale crater, Mars, *in* 54th Lunar and Planetary Science Conference: Lunar and Planetary Institute Contribution 2806, abstract 2955, <https://www.hou.usra.edu/meetings/lpsc2023/pdf/2955.pdf>.
- Sheppard, R.Y., Milliken, R.E., Parente, M., and Itoh, Y., 2021, Updated perspectives and hypotheses on the

- mineralogy of lower Mount Sharp, Mars, as seen from orbit: *Journal of Geophysical Research: Planets*, v. 126, no. 2, <https://doi.org/10.1029/2020JE006372>.
- Sheppard, R.Y., Milliken, R.E., and Robertson, K.M., 2022, Presence of clay minerals can obscure spectral evidence of Mg sulfates: Implications for orbital observations of Mars: *Icarus*, v. 383, <https://doi.org/10.1016/j.icarus.2022.115083>.
- Smith, R.J., McLennan, S.M., Achilles, C.N., Dehouck, E., Horgan, B.H.N., Mangold, N., Rampe, E.B., Salvatore, M., Siebach, K.L., and Sun, V., 2021, X-ray amorphous components in sedimentary rocks of Gale crater, Mars: Evidence for ancient formation and long-lived aqueous activity: *Journal of Geophysical Research: Planets*, v. 126, no. 3, <https://doi.org/10.1029/2020JE006782>.
- Smith, R.J., McLennan, S.M., Sutter, B., Rampe, E.B., Dehouck, E., Siebach, K.L., Horgan, B.H.N., Sun, V., McAdam, A., Mangold, N., and Vaniman, D., 2022, X-ray amorphous sulfur-bearing phases in sedimentary rocks of Gale crater, Mars: *Journal of Geophysical Research: Planets*, v. 127, no. 5, <https://doi.org/10.1029/2021JE007128>.
- Stack, K.M., et al., 2019, Evidence for plunging river plume deposits in the Pahrump Hills member of the Murray formation, Gale crater, Mars: *Sedimentology*, v. 66, no. 5, p. 1768–1802, <https://doi.org/10.1111/sed.12558>.
- Stein, N., Grotzinger, J.P., Schieber, J., Mangold, N., Hallet, B., Newsom, H., Stack, K.M., Berger, J.A., Thompson, L., Siebach, K.L., and Cousin, A., 2018, Desiccation cracks provide evidence of lake drying on Mars, Sutton Island member, Murray formation, Gale crater: *Geology*, v. 46, p. 515–518, <https://doi.org/10.1130/G40005.1>.
- Sun, V.Z., Stack, K.M., Kah, L.C., Thompson, L., Fischer, W., Williams, A.J., Johnson, S.S., Wiens, R.C., Kronyak, R.E., Nachon, M., and House, C.H., 2019, Late-stage diagenetic concretions in the Murray formation, Gale crater, Mars: *Icarus*, v. 321, p. 866–890, <https://doi.org/10.1016/j.icarus.2018.12.030>.
- Swezey, C., 1991, Description and Interpretation of the Jurassic J-2 Unconformity of the Western Interior (USA) [Master's thesis]: Austin, Texas, University of Texas at Austin, 146 p.
- Thomas, N.H., et al., 2019, Mars Science Laboratory observations of chloride salts in Gale crater, Mars: *Geophysical Research Letters*, v. 46, no. 19, p. 10,754–10,763, <https://doi.org/10.1029/2019GL082764>.
- Thompson, L.M., Berger, J.A., Spray, J.G., Fraeman, A.A., McCraig, M.A., O'Connell-Cooper, C.D., Schmidt, M.E., VanBommel, S., Gellert, R., Yen, A., and Boyd, N.I., 2020, APXS-derived compositional characteristics of Vera Rubin ridge and Murray formation, Gale crater, Mars: Geochemical implications for the origin of the ridge: *Journal of Geophysical Research: Planets*, v. 125, no. 10, <https://doi.org/10.1029/2019JE006319>.
- Thomson, B.J., Bridges, N.T., Milliken, R., Baldrige, A., Hook, S.J., Crowley, J.K., Marion, G.M., de Souza Filho, C.R., Brown, A.J., and Weitz, C.M., 2011, Constraints on the origin and evolution of the layered mound in Gale crater, Mars, using *Mars Reconnaissance Orbiter* data: *Icarus*, v. 214, no. 2, p. 413–432, <https://doi.org/10.1016/j.icarus.2011.05.002>.
- Thorpe, M.T., Hurowitz, J.A., and Dehouck, E., 2019, Sediment geochemistry and mineralogy from a glacial terrain river system in southwest Iceland: *Geochimica et Cosmochimica Acta*, v. 263, p. 140–166, <https://doi.org/10.1016/j.gca.2019.08.003>.
- Thorpe, M.T., et al., 2022, Science Laboratory CheMin data from the Glen Torridon region and the significance of lake-groundwater interactions in interpreting mineralogy and sedimentary history: *Journal of Geophysical Research: Planets*, v. 127, no. 11, <https://doi.org/10.1029/2021JE007099>.
- Treiman, A.H., Lanza, N.L., Vanbommel, S., Berger, J., Wiens, R., Bristow, T., Johnson, J., Rice, M., Hart, R., McAdam, A., and Gasda, P., 2023, Manganese-iron phosphate nodules at the Groken site, Gale crater: *Geological Society of America Abstracts with Programs*, v. 55, no. 6, <https://doi.org/10.1130/abs/2023AM-389279>.
- Turner, M., and Lewis, K., 2023, Geologic structure of the Vera Rubin ridge, Gale crater, Mars: *Journal of Geophysical Research: Planets*, v. 128, no. 9, <https://doi.org/10.1029/2022JE007237>.
- Vaniman, D.T., Bish, D.L., Ming, D.W., Bristow, T.F., Morris, R.V., Blake, D.F., Chipera, S.J., Morrison, S.M., Treiman, A.H., Rampe, E.B., and Rice, M., 2014, Mineralogy of a mudstone at Yellowknife Bay, Gale crater, Mars: *Science*, v. 343, no. 6169, <https://doi.org/10.1126/science.1243480>.
- Van Wagoner, J.C., Mitchum, R.M., Campion, K.M., and Rahmanian, V.D., 1990, *Siliciclastic Sequence Stratigraphy in Well Logs, Cores, and Outcrops: Concepts for High-Resolution Correlation of Time and Facies*: American Association of Petroleum Geologists Methods in Exploration 7, 55 p., <https://doi.org/10.1306/Mth7510>.
- Viviano, C.E., Seelos, F.P., Murchie, S.L., Kahn, E.G., Seelos, K.D., Taylor, H.W., Taylor, K., Ehlmann, B.L., Wiseman, S.M., Mustard, J.F., and Morgan, M.F., 2014, Revised CRISM spectral parameters and summary products based on the currently detected mineral diversity on Mars: *Journal of Geophysical Research: Planets*, v. 119, no. 6, p. 1403–1431, <https://doi.org/10.1002/2014JE004627>.
- Watkins, J.A., et al., 2022, Burial and exhumation of sedimentary rocks revealed by the base Stimson erosional unconformity, Gale crater, Mars: *Journal of Geophysical Research: Planets*, v. 127, no. 7, <https://doi.org/10.1029/2022JE007293>.
- Weitz, C.M., Lewis, K.W., Bishop, J.L., Thomson, B.J., Arvidson, R.E., Grant, J.A., Seelos, K.D., and Etenborough, I., 2022, Orbital observations of a marker horizon at Gale crater: *Journal of Geophysical Research: Planets*, v. 127, no. 4, <https://doi.org/10.1029/2022JE007211>.
- Wiens, R.C., et al., 2012, The ChemCam instrument suite on the Mars Science Laboratory (MSL) rover: Body unit and combined system tests: *Space Science Reviews*, v. 170, no. 1–4, p. 167–227, <https://doi.org/10.1007/s11214-012-9902-4>.
- Wiseman, S.M., Arvidson, R.E., Morris, R.V., Poulet, F., Andrews-Hanna, J.C., Bishop, J.L., Murchie, S.L., Seelos, F.P., Des Marais, D., and Griffes, J.L., 2010, Spectral and stratigraphic mapping of hydrated sulfate and phyllosilicate-bearing deposits in northern Sinus Meridiani, Mars: *Journal of Geophysical Research: Planets*, v. 115, no. E7, E00D18, <https://doi.org/10.1029/2009JE003354>.

SCIENCE EDITOR: MIHAI DUCEA  
ASSOCIATE EDITOR: CHRISTIAN KOEBERL

MANUSCRIPT RECEIVED 25 SEPTEMBER 2023  
REVISED MANUSCRIPT RECEIVED 18 APRIL 2024  
MANUSCRIPT ACCEPTED 28 MAY 2024